ICFO-The Institute of Photonic Sciences

Doctoral Thesis

Polaron physics in carbon nanotube electro-mechanical resonators

Author:
Sergio Lucio
De Bonis

Supervisor:
Prof. Adrian
Bachtold

A thesis submitted in fulfillment of the requirements for the degree of Doctor of Photonics

in the

Quantum Nanomechanics Group

December 2019

Acknowledgements

Vorrei suonare come gli Area
il gruppo italiano
- *Come gli Area*, EELST

Music is THE BEST.
- Frank Zappa

First I would like to thank my advisor Prof. Adrian Bachtold for giving me the opportunity to do my PhD in a great environment. He taught me to be always optimistic and never give up. I would also like to thank Prof. Edward Laird, Prof. Eddy Collin and Prof. Romain Quidant for accepting to be part of my thesis committee and finding the time to read my thesis. I would also like to thank Prof. Darrick Chang and Prof. Maria José Esplandiu Egido for agreeing to serve as substitute members.
I would like to thank Prof. Joel Moser and Dr. Chandan Samanta. I had the opportunity to work with them respectively at the beginning and at the end of my PhD. It was a really precious experience either scientifically and humanly. Overall, I'm grateful to all the past and present members of the Quantum Nanomechanics group for the continuous help and also to make the working environment always nice and relaxing. I want to thanks also all the ICFO and non-ICFO people with whom I shared a laugh during this years in Barcelona.
Finally I want to thank my family. Michele, Lina, Roberto, Valeria and Gianpaolo, you were always by my side respecting my decisions and encouraging me constantly. And Barbara, thanks for being the salt of my life.

Abstract

Carbon nanotube (CNT) mechanical resonators are unique systems because they combine remarkable mechanical properties with rich charge transport characteristics. Thanks to their intrinsically low-dimensional nature, their mass is extremely low. The mechanical resonance frequency reaches the GHz regime, can be widely tunable and they show quality factor as high as several million. Nanotubes hold great promise for sensing applications. Nanotubes are an excellent system to study quantum electron transport, which range from Fabry-Pérot interference to Coulomb blockade. These completely opposite regimes can be very efficiently coupled to the mechanics, since the two degrees of freedom, electrons and phonons, are embedded in the same system.
In the first section of this thesis we develop a detection scheme utilizing a RLC resonator together with a low-temperature HEMT amplifier. This allows us to lower the current noise floor of the setup and carry out sensitive electrical noise measurements, demonstrating a displacement sensitivity of 0.5 $\mathrm{pm}/\sqrt{\mathrm{Hz}}$ and a force sensitivity of 4.3 $\mathrm{zN}/\sqrt{\mathrm{Hz}}$. This surpasses what has been achieved with mechanical resonators to date and paves the way for the detection of individual nuclear spins. We also improve the device fabrication enhancing the capacitive coupling between mechanical vibrations and electrons flowing though the nanotube.
In the second part of this work, we study the electron-phonon coupling in CNT resonators in the Coulomb blockade regime and report on the long-sought-after demonstration of the ultra-strong coupling regime. Mechanical vibrations and electrons are so strongly coupled that it no longer makes sense to think of them as distinct entities, but rather as a quasi-particle: a polaron. First, we demonstrate that the polaronic nature of charge carriers modifies the quantum electron transport through the device. In previous electromechanical devices, the coupling was too weak to have any effect on the DC electrical conductance. Second, we show high tunability of polaron states by electrostatic means. This is something not possible to do with polarons in other systems, such as bulk crystals. Notably, this interaction creates a highly nonlinear potential for the phonon mode which establishes nanotube resonator as a possible platform for the demonstration of mechanical qubits.

Abstracto

Los resonadores mecánicos de nanotubos de carbono (CNT) son sistemas únicos porque combinan propiedades mecánicas notables con ricas características de transporte de carga. Gracias a su naturaleza intrínsecamente de baja dimensión, su masa es extremadamente baja. La frecuencia de resonancia mecánica alcanza el régimen de GHz, puede ser ampliamente ajustable y muestra un factor de calidad de hasta varios millones. Los nanotubos son muy prometedores para las aplicaciones de detección. Los nanotubos son un excelente sistema para estudiar el transporte cuántico de electrones, que van desde la interferencia Fabry-Pérot hasta el bloqueo de Coulomb. Estos regímenes completamente opuestos se pueden acoplar de manera muy eficiente a la mecánica, ya que los dos grados de libertad, electrones y fonones, están integrados en el mismo sistema. En la primera sección de esta tesis desarrollamos un esquema de detección que utiliza un resonador RLC junto con un amplificador HEMT de baja temperatura. Esto nos permite reducir el ruido de fondo actual del setup y realizar mediciones de ruido eléctrico sensibles, demostrando una sensibilidad de desplazamiento de 0.5 $\mathrm{pm}/\sqrt{\mathrm{Hz}}$ y una sensibilidad de fuerza de 4.3 $\mathrm{zN}/\sqrt{\mathrm{Hz}}$. Esto supera lo que se ha logrado con resonadores mecánicos hasta la fecha y allana el camino para la detección de espines nucleares individuales. También mejoramos la fabricación del dispositivo mejorando el acoplamiento capacitivo entre vibraciones mecánicas y electrones que fluyen a través del nanotubo. En la segunda parte de este trabajo, estudiamos el acoplamiento de electrones y fonones en resonadores CNT en el régimen de bloqueo de Coulomb e informamos sobre el tan buscado después de la demostración del régimen de acoplamiento ultra fuerte. Las vibraciones mecánicas y los electrones están tan fuertemente acoplados que ya no tiene sentido pensar en ellos como entidades distintas, sino más bien como una cuasi partícula: un polaron. Primero, demostramos que la naturaleza polarónica de los portadores de carga modifica el transporte cuántico de electrones a través del dispositivo. En dispositivos electromecánicos anteriores, el acoplamiento era demasiado débil para tener algún efecto sobre la conducción eléctrica continua. En segundo lugar, mostramos una alta capacidad de sintonización de los estados de Polaron por medios electrostáticos. Esto es algo que no es posible hacer con los polarones en otros sistemas, como los cristales a granel. Notablemente, esta interacción crea un potencial altamente no lineal para el modo de fonón que establece el resonador de tubos de resonancia como una posible plataforma para la demostración de qubits mecánicos.

Contents

Chapter 1

Introduction

Miniaturized mechanical resonators have been proven to have a major impact both on technological advancement and fundamental physical research [1]. Micro-electromechanical resonators (MEMS) are widely present in our everyday life. Gyroscopes and antennas in our smartphones (Fig.1.1(a)), accelerometers that trigger airbags in our cars (Fig. 1.1(b)), blood pressure sensors in hospitals are all MEMS-based devices. Micro resonators have become nowaday essential tools to carry out basic science research. A great example is the atomic force microscope (AFM) [2]. It consists of a micro-machined cantilever, with an extremely sharp tip used to perform surface imaging. It is based on resonance frequency shifts and amplitude oscillation modulations which are induced by the surface local forces. This technique is one of the most powerful imaging tools with the resolution pushed down to subatomic scale [3]. Because of its versatility and the fact that it can be easily operated in different temperature and pressure conditions, one microscope was even sent to Mars to examine the fine detail structure of soil and water ice samples (Fig.1.1(c)).

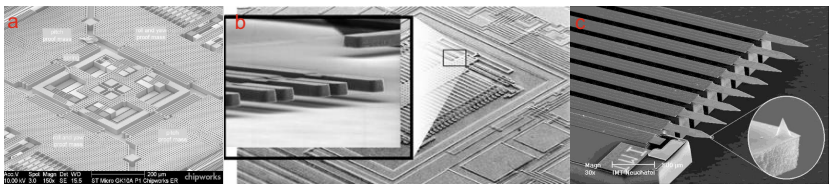

FIGURE 1.1: Examples of commercially available MEMS devices. (a) Part of a gyroscope system embedded inside iPhone4 smartphones. (b) An accelerometer sensor forming part of airbag systems present in every car. (c) The eight sharp tips of the NASA's Phoenix Mars Lander's AFM sent to Mars.

The strength of micro- and nano-electromechanical resonators (NEMS) is the possibility to couple them with other degrees of freedom with an extreme efficiency. Mechanical resonators have been coupled to charges in single-electron transistors (SETs) (Fig.1.2(a)) [4–12], microwave

electromagnetic radiation [13, 14] (Fig.1.2(b)), superconductive qubits [15], superconducing films [16] and superfluids [17–19]opening new horizons in quantum science and technology. In a ground-breaking experiment of the group of Cleland, a mechanical resonator was cooled in the quantum regime, that is, into its ground state [20], and was coupled to a qubit, which was used to measure the quantum state of the resonator.
On the other hand, the exceptional sensitivity of mechanical resonators found a logical application in sensing experiments. These range from mass detection [21, 22], to cantilever magnetometry [23, 24], to charge sensing [4] and force-detected magnetic resonance (MRFM) [25]. In this last class of experiments the physics of nuclear magnetic resonance (NMR) is combined with the techniques of scanning probe microscopy.
In a typical MRFM experiment, a cantilever is used to detect mechanically the very small magnetic force due to electron or nuclear spins in the sample, which is generated by the interaction between these spins and a strong magnetic field gradient. This force can be probed following different read-out schemes, which include periodically flipping the spins by the means of an oscillatory magnetic field using typical NMR protocols. In a milestone experiment Rugar and collaborators mechanically detected a single electron spin with an ultra-soft silicon cantilever [26] (Fig.1.2(c)). Advances in micro- and nano-fabrication of these 'top-down' resonators enables the improvement of their force sensitivity [27], spacial resolution [28] and nanoscale magnetic resonance imaging (MRI) [29].

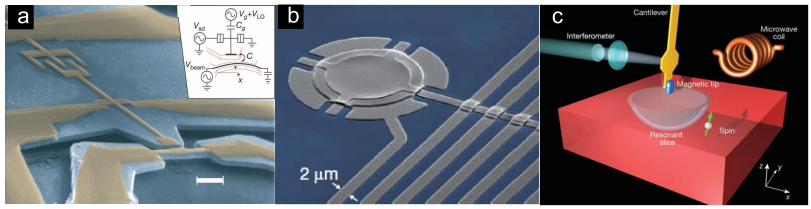

FIGURE 1.2: Examples of nanomechanical resonators. (a) Scanning electron micrograph of a device based on GaAs and aluminium structures, where the mechanical resonator is coupled to a single-electron transistor[5]. (b) An aluminium electromechanical circuit consisting of a vibrating membrane coupled to superconducting microwave cavity [14]. (c) Magnetic resonance force microscopy of a single electron spin with a NEMS cantilever containing a magnetic tip [26]

The push towards even smaller mechanical oscillators generated close attention because of the outstanding mechanical properties of these objects. Recently, extremely small and light nanoscale systems,

such as levitated nanoparticles [30, 31] and carbon nanotubes (CNTs) [32, 33], have shown unprecedented force noise sensitivities approaching 1zN/$\sqrt{\text{Hz}}$ (1zN=10^{-21}N). In Fig.1.3(a), a CNT mechanical resonator in the doubly-clamped geometry is shown.
This value would be exactly the magnitude of the force generated by a single nuclear spin in a typical MRFM experiment [34].

Carbon nanotube mechanical resonators have attracted considerably attention in recent years. The high strength, the extremely low mass and the rich transport physics enabled the realization of resonators with very interesting characteristics. Their mechanical resonance frequency can be pushed in the GHz regime [35, 36], the quality factor can reach very high values [32, 37] and the resonance frequency is highly tunable [38] .
Moreover, it's known that for thermally limited mechanical force transducers the minimum detectable force is limited by the force noise spectral density $S_F = 4k_B T \frac{M\omega_m}{Q}$ associated to the Brownian fluctuation of the resonator's position, where k_B is the Boltzmann constant, T is the modal temperature, M the effective mass, ω_m the resonance frequency and Q the quality factor. This expression indicates that resonators with a small mass tend to be endowed with a weak thermal force noise. Because of their small mass, CNT resonators have been utilized as sensors for mass [22, 39] and force [40]. Together with these exciting mechanical properties, carbon nanotubes possess unique electrical characteristics. The ambipolar transport, in which the electrical current is carried by either holes or electrons, have been coupled to mechanics. Striking effects in such devices due to single-electron tunnelling events, in the so-called Coulomb blockade regime [41], have been reported for almost 20 years [6–8, 10, 42–45]. In the opposite regime, where the electrical conductance shows Fabry-Pérot electron interference patterns [46], the dissipation is extremely low due to the ballistic nature of the charge carriers enabling to reach very high mechanical quality factor [32] (the two transport regimes are shown in Fig.1.3(b)).

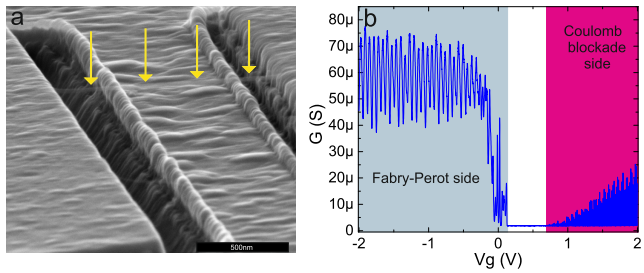

FIGURE 1.3: A CNT electro-mechanical resonator. (a) Scanning electron microscopy image of a CNT mechanical resonator clamped between two metal electrodes and suspended and vibrating above a gate electrode. (b) Electrical conductance as a function of the DC gate voltage measured at the base temperature of our dilution refrigerator.

My Ph.D thesis work finds his motivation in all these intriguing experimental phenomena. In this dissertation we want to explore the vast possibilities offered by CNT mechanical resonators at low temperatures. First, we develop a read-out scheme that allows us to carry out ultra-sensitive measurements, and to demonstrate the great performances of CNT resonators as force sensors. Secondly, we investigate the electron-phonon interaction in a new regime where the coupling between vibrations and electrons is ultra-strong, and the restoring mechanical potential is highly nonlinear near the quantum regime. An outline of the thesis is given below:

- Chapter 2 gives a brief introduction on the main theoretical concepts to understand the basic dynamical properties of nanomechanical resonators.
- Chapter 3 provides a basic introduction of the electron transport in carbon nanotube based quantum dots.
- Chapter 4 discusses the implementation of the low-noise read-out scheme and the measurement of force and displacement noise performances in CNT mechanical resonators.
- Chapter 5 investigates the formation of polarons in CNT-based SET mechanical resonators and the related effects on the mechanics and electron transport.

Chapter 2

Basics of nanomechanics

In this chapter we briefly review the basics of nanomechanics and introduce essential concepts to understand the mechanical properties of nanoresonators. First, we start with the model of a simple harmonic oscillator with an external coherent drive. We then describe its response to incoherent fluctuating thermal forces. We mention the nonlinear response of a Duffing oscillator. We conclude discussing the mechanics of a double clamped beam in the context of continuum mechanics model, which is a good approximation for the description of a carbon nanotube mechanical resonator.

2.1 The linear harmonic oscillator with coherent driving

The simplest way to describe the motion of a mechanical resonator, with an arbitrary geometry, is to use the concept of a harmonic oscillator. In absence of damping and external driving a harmonic oscillator is subject to the force: $F = -kz(t)$, where $z(t)$ is the displacement and k is the mechanical spring constant.
According to the Newton's second law, we get:

$$F = m_{\text{eff}} \frac{d^2 z(t)}{dt^2} = -kz(t), \tag{2.1}$$

where m_{eff} is the effective mass of the nanomechanical oscillator. The effective mass can be lower than the physical mass of the resonator. The solution of the equation 2.1 results in:

$$z(t) = z_0 \ \exp(-i\omega_m t + i\phi) \tag{2.2}$$

where ω_m is the mechanical angular resonance frequency of the oscillator, also given by $\omega_m = \sqrt{\frac{k}{m_{\text{eff}}}}$, z_0 and ϕ are the initial values for the amplitude and the phase of the motion.
However, in a realistic situation the interaction with the environment

has to be taken into account. This interaction expresses itself through a force δF and dissipation Γ_m. The equation 2.1 can be written as:

$$m_{\text{eff}}\frac{d^2z(t)}{dt^2} + kz(t) + m_{\text{eff}}\Gamma_{\text{m}}\frac{dz(t)}{dt} = \delta F(t) \tag{2.3}$$

where Γ_{m} and δF are related through the fluctuation-dissipation theorem. In the case of a coherently driven harmonic oscillator, assuming a weak sinusoidal drive $\delta F(t) = F_{\text{d}}\cos(\omega_{\text{d}}t)$ with F_{d} the driving amplitude and ω_{d} the driving frequency, the equation can be solved with the ansatz in the equation 2.2 where ϕ is now the phase difference between the mechanical motion and the driving force. The driving frequency dependent amplitude and phase response take the following forms:

$$z(\omega_{\text{d}}) = \frac{F_{\text{d}}}{m_{\text{eff}}}\frac{1}{\sqrt{(\omega_{\text{m}}^2 - \omega_{\text{d}}^2)^2 + (\Gamma_{\text{m}}\omega_{\text{d}})^2}} \tag{2.4}$$

$$\phi(\omega_{\text{d}}) = \arctan\left(\frac{\Gamma_{\text{m}}\omega_{\text{d}}}{\omega_{\text{m}}^2 - \omega_{\text{d}}^2}\right) \tag{2.5}$$

The amplitude of the motion is maximum at resonance ($\omega_{\text{d}} = \omega_{\text{m}}$). There the mechanical motion and the drive acquire a phase difference of $\pi/2$ (see Fig.2.1). Before finishing this section, we want to intro-

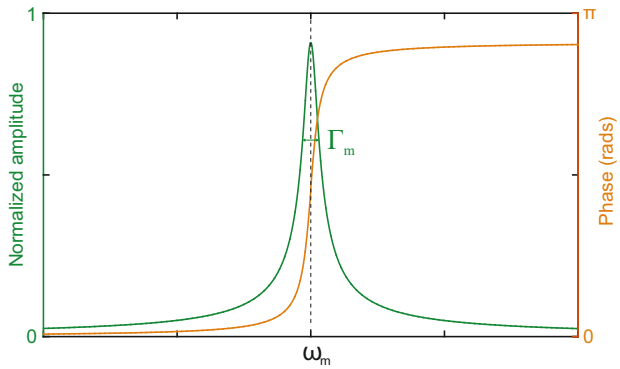

FIGURE 2.1: Amplitude and phase response of a harmonic oscillator as a function of coherent driving force. At resonance ($\omega = \omega_m$) the amplitude reaches a maximum and it is $\pi/2$ out of phase with the driving force. Panel is adapted from [47]

duce a very important figure of merit that characterizes a mechanical resonator, the quality factor Q. It quantifies the interaction between the resonator and its environment, which induces the damping of the

motion. The quality factor is defined as the total energy E_{tot} stored in the resonator divided by the energy lost per cycle of vibration ΔE_{cycle}:

$$Q = 2\pi \frac{E_{tot}}{\Delta E_{cycle}} \tag{2.6}$$

For small damping, $\Gamma_m << \omega_m$, the quality factor reads:

$$Q = \frac{\omega_m}{\Gamma_m} \tag{2.7}$$

2.2 The linear harmonic oscillator with incoherent driving: thermomechanical motion

The coupling of the mechanical resonator to a thermal bath leads to dissipation, quantified by the quality factor. Moreover, this coupling also manifests itself as a statistical random driving force δF acting on the resonator. This induces the so-called thermal Brownian motion. Basically, the dissipative term $m_{eff}\Gamma_m \frac{dz}{dt}$ in equation 2.3 represents the thermalization process of the resonator with its environment. This is well described by the fluctuation-dissipation theorem [48], which asserts that, in thermal equilibrium, the dissipation of the resonator is directly linked to the fluctuating thermal forces acting on it. Let's derive it.
Inserting in the equation 2.3 this statistical random force, it gives us the equation of motion for a resonator driven by random thermal fluctuating forces. For the sake of convenience, we perform the Fourier transform of this equation in frequency space and it reads:

$$z(\omega) = \chi(\omega) \cdot \delta F(\omega) \tag{2.8}$$

where $\chi(\omega)$ is the mechanical susceptibility given by:

$$\chi(\omega) = \frac{1}{m_{eff}(\omega_m^2 - \omega^2 - i\Gamma_m\omega).} \tag{2.9}$$

This represents the linear response of the displacement $z(\omega)$ to the random fluctuating force. What is often measured in the lab is the power spectral density (PSD) $S_{zz}(\omega)$ of the displacement $z(t)$. We now introduce the autocorrelation function of $z(t)$:

$$C_z(\tau) = \langle z^*(t)z(t+\tau)\rangle = \int_{-\infty}^{\infty} z(t)^* z(t+\tau)dt \tag{2.10}$$

where $z^*(t)$ is the complex conjugate of $z(t)$ and $\langle ...\rangle$ denotes the statistical average. From the Wiener-Khinchin theorem we know that the

Fourier transform of the autocorrelation function of $z(t)$ and its PSD $S_{zz}(\omega)$ are Fourier transform [1] pair:

$$S_{zz}(\omega) = \int_{-\infty}^{\infty} d\tau \langle z^*(t) z(t+\tau) \rangle e^{i\omega t} \tag{2.11}$$

The unit of PSD is $[(\mathrm{m})^2/\mathrm{Hz}]$. Using this relation in equation 2.8 we can make a connection between the PSD of the force $S_{FF}(\omega)$ and PSD of the displacement $S_{zz}(\omega)$, via the mechanical susceptibility $\chi(\omega)$:

$$S_{zz}(\omega) = |\chi(\omega)|^2 S_{FF}(\omega) \tag{2.12}$$

This equation is the equivalent of equation 2.8, but expressed in experimentally measurable quantities.
According to the linear response theory [49], the single-sided PSD of the thermal force noise reads as:

$$S_F^{th}(\omega) = -\frac{4k_B T}{\omega} Im\left(\frac{1}{\chi(\omega)}\right) \tag{2.13}$$

where k_B is the Boltzmann constant and T is the temperature. In the classic limit and for weak damping, the fluctuation-dissipation theorem can be written as:

$$S_F^{th} = 4k_B T m_{eff} \Gamma_m \tag{2.14}$$

The thermal force noise S_F^{th} is white. It is similar to the Johnson-Nyquist noise used to express the voltage noise of a resistor. Combining equations 2.14 and 2.12 we get the PSD of the thermal displacement:

$$S_z^{th}(\omega) = \frac{4k_B T \Gamma_m}{m_{eff}[(\omega_m^2 - \omega^2)^2 + (\Gamma_m \omega)^2]} \tag{2.15}$$

From the equipartition theorem for a harmonic oscillator in thermal equilibrium we know:

$$\frac{1}{2} m_{eff} \langle \dot{z}_{th}^2 \rangle = \frac{1}{2} k \langle z_{th}^2 \rangle = \frac{1}{2} k_B T \tag{2.16}$$

This equation, together with the fact that the variance of the displacement $\langle z_{th}^2 \rangle$ can be estimated from the area under the single-sided PSD of the thermal displacement $S_z^{th}(\omega)$, give us:

$$\langle z_{th}^2 \rangle = \frac{k_B T}{m_{eff} \omega_m^2} = \int_0^{\infty} \frac{1}{2\pi} S_z^{th}(\omega) d\omega \tag{2.17}$$

This last observation allows us to extract the modal temperature of a resonator by simply integrating over the resonance, as schematized in Fig.2.2

[1] We use the following convention $z(t) = \frac{1}{2\pi} \int_{-\infty}^{\infty} z(\omega) e^{i\omega t} d\omega$ and $z(\omega) = \int_{-\infty}^{\infty} z(t) e^{i\omega t} dt$

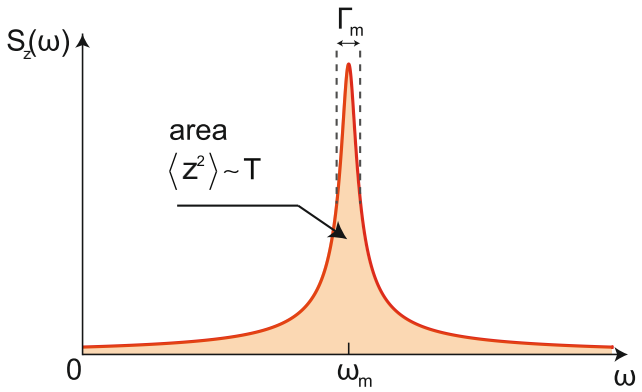

FIGURE 2.2: Thermal noise displacement power spectrum. The area under the displacement PSD is proportional to the modal temperature. Panel is adapted from [47]

2.3 Nonlinear response: Duffing oscillator

When a nanomechanical resonator is driven to large displacement amplitude its behaviour deviates from the harmonic oscillator approximation. In this case nonlinear restoring forces have to be taken into account; their origin can be geometrical or due to external nonlinear potentials. The equation of motion has an additional term which is proportional to the cubic displacement of the resonator:

$$m_{\mathrm{eff}}\frac{d^2z(t)}{dt^2} + kz(t) + m_{\mathrm{eff}}\Gamma_{\mathrm{m}}\frac{dz(t)}{dt} + \alpha z^3(t) = F_{\mathrm{d}}(t) \tag{2.18}$$

with α the Duffing nonlinear constant. In the limit of small amplitude, we obtain:

$$z(\omega_{\mathrm{d}}) \approx \frac{F_{\mathrm{d}}}{2m_{\mathrm{eff}}\omega_{\mathrm{m}}^2}\frac{1}{\sqrt{\left(\frac{\omega_{\mathrm{d}}-\omega_{\mathrm{m}}}{\omega_{\mathrm{m}}} - \frac{3}{8}\frac{\alpha}{m_{\mathrm{eff}}\omega_{\mathrm{m}}^2}z^2\right)^2 + (2Q_{\mathrm{m}})^{-2}}} \tag{2.19}$$

It can be demonstrated that above a critical amplitude the equation has three solutions, two of which are stable. The appearance of bistable and hysteretic behaviour when sweeping back and forth the driving frequency is a consequence of the nonlinear contribution in the motion of the resonator. The amplitude response below and above this critical driving is shown in Fig.2.3. As we already showed for low driving, the amplitude response is described by a Lorentzian function while, for high driving, the resonance frequency shifts to higher ($\alpha > 0$) or

lower ($\alpha < 0$) values leading to hardening or softening of the effective mechanical spring constant.

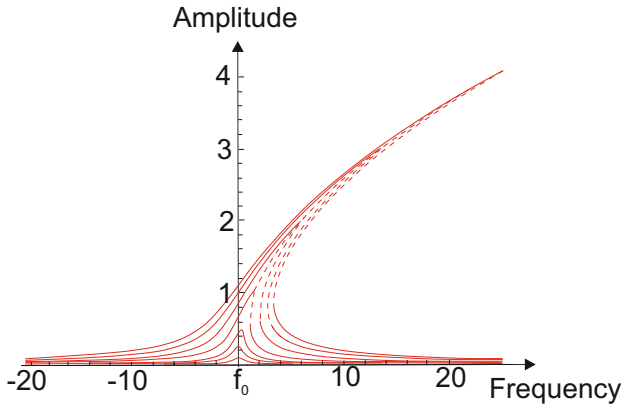

FIGURE 2.3: Amplitude response of a Duffing oscillator versus frequency for increasing driving amplitudes. Figure adapted from [50]

For a long time, nonlinearity in nanoresonators has been the subject of many theoretical [50] and experimental [51, 52] works and, because of its great importance to the understanding of ultimate nanomechanical resonators behaviour, it still attracts considerable attention [53, 54].
To conclude this part, we just mention that nonlinearity can also appear in the damping due to mechanisms whose microscopic origin is not yet clear. This effect can be taken into account by adding in the equation of motion a term $\eta z^2(t)\frac{dz(t)}{dt}$. Nonlinear damping has been observed recently in graphene and carbon nanotubes [55], and in diamond nanoelectromechanical resonators [56].

2.4 Mechanics of a double clamped beam: the case of a carbon nanotube

In this last section of the chapter we want to discuss the mechanics of a double clamped beam using the continuum mechanics model. This is interesting because carbon nanotube can be modeled as a double clamped beam with a tubular cross section. This model allows us to extract, for example, the tension T of the resonator and its effective mass m_{eff}.

In the continuum model that we are discussing, only flexural modes

of vibration are considered. This means that only displacement in z-direction is taken into account (see Fig.2.4(a)). The nanotube is oriented in the x-direction and a tension T in the beam is induced by the clamping electrodes. The total elastic energy reads [57, 58]:

$$U = \frac{1}{2}\int_0^L \left(EI\frac{\partial^2 z}{\partial x^2} + T_0 + \frac{1}{2}EA\left(\frac{\partial z}{\partial x}\right)^2 + Kz \right) dx \tag{2.20}$$

where E is the Young's modulus, I the moment of inertia, A the uniform circular cross sectional area, T_0=$A\sigma$ the in-built tension with σ being the stress and finally K a constant downward force in the x-z plane.
Minimizing U leads to following equilibrium equation:

$$EI\frac{\partial^4 z}{\partial x^4} - T\frac{\partial^2 z}{\partial x^2} - K = 0 \tag{2.21}$$

where the tension is given by $T = T_0 + \frac{EA}{2L}\int_0^L \left(\frac{\partial z}{\partial x}\right)^2 dx$. Equation 2.21 can be solved in two limits.
In the first limiting case, called bending limit, the tension is smaller than the bending rigidity ($T \ll EI$) and the resonance frequency of the first mode is given by:

$$\omega = \frac{22.4}{L^2}\sqrt{\frac{EI}{\mu}} + 0.28T\sqrt{\frac{1}{\mu EI}} \tag{2.22}$$

where L is the length and μ is the linear mass density.
In the opposite limit, called the tension limit, the tension is larger than the bending rigidity ($T \gg EI$) and the resonance frequency is:

$$\omega = \frac{\pi}{L}\sqrt{\frac{T}{\mu}} + \frac{2\pi}{L^2}\sqrt{\frac{EI}{\mu}}. \tag{2.23}$$

The effective mass m_{eff} of an eigenmode depends on the mode shape. Following the derivation in [59], in the bending regime we get for the effective mass of the fundamental mode $m_{eff} = m \cdot 0.3965$ (where m is the mass of the resonator). Instead, in the tension regime, we get $m_{eff} = \frac{m}{2}$.

Finally, we consider the case of a nanotube resonator subject to an electrostatic force induced by an applied DC gate potential V_g^{DC} (like in Fig.2.4(a)). A tension T (beside the pre-existing one T_0) can arise from the electrostatic force that reads:

$$F_{el}^{DC} = \frac{1}{2}C_g'(V_g^{DC} - V_0)^2 \tag{2.24}$$

where V_0 is the effective charge neutrality voltage of the nanotube and C'_g the derivative of the gate-nanotube capacitance C_g with respect to the displacement in z-direction. From [57], we assume that the tension depends on the electrostatic force as $T \approx F_{el}^{DC}/\sqrt{24s}$, where s is the slack [2] in the nanotube beam.
For low enough gate voltage, we are in the bending regime. From equation 2.22 we obtain:

$$\Delta\omega_{bend} \sim \Delta T \sim (V_g^{DC} - V_0)^2 \tag{2.25}$$

For high gate voltage, we are in the tension regime and using 2.23 we get:

$$\Delta\omega_{tens} \sim \sqrt{\Delta T} \sim V_g^{DC} - V_0 \tag{2.26}$$

In Fig.2.4(b) both regimes are shown. The transition between the two behaviours occurs for $T = EI/L^2$, at the gate voltage V_g^*:

$$V_g^* \approx \sqrt{\frac{2EI\sqrt{24s}}{C'_g}} \tag{2.27}$$

[2] The slack s is given by the ratio $\frac{L-L_0}{L}$ where L is the length of the beam and L_0 is the distance between the two clamping points.

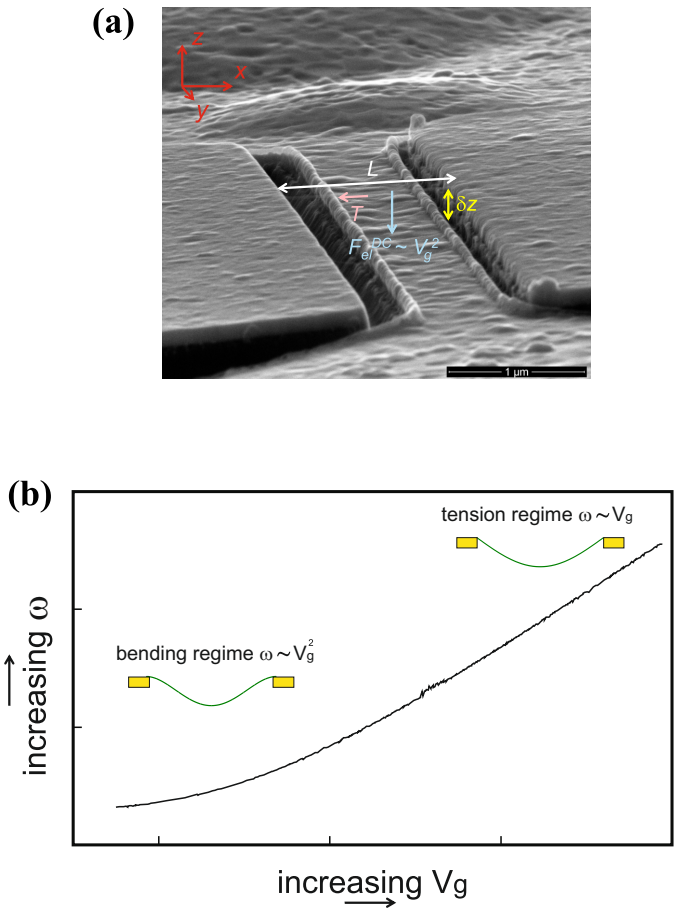

FIGURE 2.4: Double clamped carbon nanotube mechanical resonator. (a) A suspended carbon nanotube resonator with a length L. A constant electrical force F_{el}^{DC}, generated by a gate voltage, induces a tension T in the beam. (b) Dependence of the resonance frequency of double clamped beam on the static gate voltage. In the bending regime, the force is small and the frequency has a quadratic dependence. In the tension regime, the frequency increases linearly with the gate voltage.

Chapter 3

Electron transport in carbon nanotube quantum dots

In this section we introduce essential concepts of electron transport in zero-dimensional systems, with a special focus on carbon nanotube based quantum dots. First, we give a rapid review on the band-structure of carbon nanotube which will help us to understand the peculiar features of transport experiments at low temperatures. A large part of this chapter is dedicated to Coulomb blockade physics. The quantization effect of the charge and the main energy scales are introduced. The constant interaction model (CI) is used to explain the origin of the well known Coulomb blockade stability diagrams. Finally, we briefly present the cases of co-tunnelling and Fabry-Pèrot interference which are important effects in CNT electron transport, but not the focus of this dissertation.

3.1 From graphene band-structure to carbon nanotubes

3.1.1 Graphene

A carbon nanonotube (CNT) can be described as a sheet of graphene, a single atomic layer of graphite, rolled up into a cylinder with a radius of about one nanometer. Because of this, it is helpful to start from the graphene band-structure to understand the electronic properties of a CNT. Graphene consists of a two-dimensional honeycomb lattice in which every carbon atom has three nearest neighbors with a C-C bond length of $a_0 = 1.42$ Å. In Fig.3.1(a) the unit cell is represented. It is defined by the two lattice vectors $\vec{a}_1$ and $\vec{a}_2$ and contains two carbon atoms.

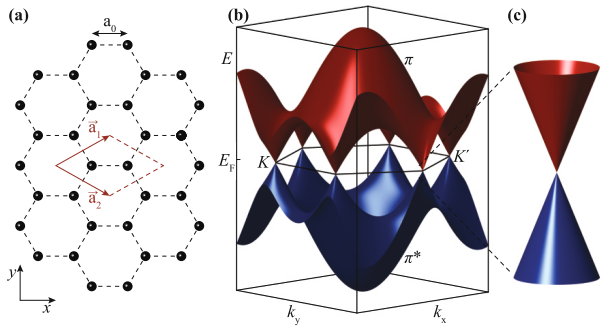

FIGURE 3.1: Lattice and band-structure of graphene. (a) Honeycomb lattice of a graphene sheet with an inter-atomic distance of a_0=1.42 Å. The unit cell is determined by the two lattice vectors $\vec{a}_1$ and $\vec{a}_2$ and contains two atoms. (b) The band-structure with the π^* and π orbitals merging at the K and K′ corner points of the exagonal first Brillouin zone. (c) The linear dispersion of graphene at Dirac-like low energy points [60]

Every carbon atom has four covalent electrons, three of them hybridize in a strong covalent sp^2 bond which determines the binding energy and the elastic properties of the sheet of graphene. The fourth electron is in a p_z orbital which forms delocalized π (bonding) and π^* (antibonding) orbitals. They can overlap with their neighboring orbitals and determine the conductivity of the graphene.
Using the tight binding model the energy-momentum relation can be written as follow [61]:

$$E(\vec{k}) = \pm\gamma\sqrt{3 + 2\cos(\vec{k}\cdot\vec{a}_1) + 2\cos(\vec{k}\cdot\vec{a}_2) + 2\cos(\vec{k}\cdot(\vec{a}_2 - \vec{a}_1))} \tag{3.1}$$

where γ is the overlap integral and the positive and negative solutions are for π^* and π orbitals, respectively.
The band-structure is depicted in Fig.3.1(b). It consists of the two subbands π and π^* which meet at the so-called charge neutrality points, or Dirac points, forming cone shaped structures, located at the vertices of the hexagonal Brillouin zone. Because of symmetry reasons, only two of these six points are non-equivalent and they are denoted as K and K′ valleys. Near the Dirac point (at low energy, where the Fermi energy $E_F = 0$), the energy dispersion is linear (Fig.3.1(c)). This means that all charge carriers have the same velocity and the dispersion relation can be expressed as:

$$E(\vec{\kappa}) = \pm\hbar v_F|\vec{\kappa}| \tag{3.2}$$

with $\vec{\kappa} = \vec{k} - \vec{K}$ and $v_F = 3\gamma a_0/2\hbar \approx 10^6$ m/s for $\gamma = 3$ eV [62].

3.1.2 Rolling up a graphene sheet to obtain a carbon nanotube

A CNT can be visualized as a layer of graphene rolled up into a seamless tube. The electronic properties of a CNT depend on its circumferential, or the so-called chiral vector $\vec{C} = n\vec{a}_1 + m\vec{a}_2$ with $n, m \in \mathbb{N}$ depicted in Fig.3.2(a). This chiral vector together with the translation vector $\vec{T}$ define the surface area of the carbon nanotube (yellow and orange areas in the figure).

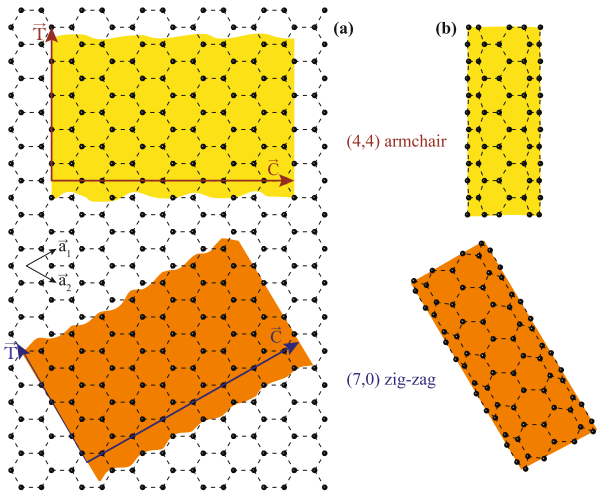

FIGURE 3.2: Rolling-up a graphene sheet: a carbon nanotube. (a) The chiral vector $\vec{C}$ and the translation vector $\vec{T}$ define the surface area and the electronic properties of a CNT. (b) Representation of a (4,4) armchair and a (7,0) zig-zag CNTs with the chiral indices (n, m).

The chiral indices (n, m) determine the type of CNT. A nanotube is armchair if $(n, m = n)$ and zig-zag if $(n, 0)$. CNTs with arbitrary values for the indices (n, m) are called chiral. Two examples are illustrated in Fig.3.2(b). The zone-folding approximation introduces periodic boundary conditions in the circumferential direction, which implies quantization of the wave vector component $\kappa_\perp$ perpendicular to the axial direction of the tube. The longitudinal wave vector $\kappa_\parallel$ can instead be considered continuous since electrons can move freely in this direction. The quantization of $\vec{k}$ along $\vec{C}$ gives the allowed values for $\kappa_\perp$:

$$\vec{C} \cdot \vec{\kappa} = \pi d \kappa_\perp = 2\pi \left(\frac{m-n}{3} + p \right) \tag{3.3}$$

where $p \in \mathbb{Z}$ [63]. This generates a series of one-dimensional sub-band for each $\kappa_\perp$ mode (as showed in Fig.3.3(a)). The contribution to the charge transport comes from the states in sub-bands with $E(\kappa)$ close to E_F (similarly to graphene with K and K' valleys) and the way κ states and K points are aligned is set by the chiral indices and determines the electrical properties: if one subband goes through the Dirac point, the density of states will be finite (see Fig.3.3(b)). Such nanotubes are defined as metallic. Otherwise, the nanotube is semiconducting (see Fig.3.3(c)).

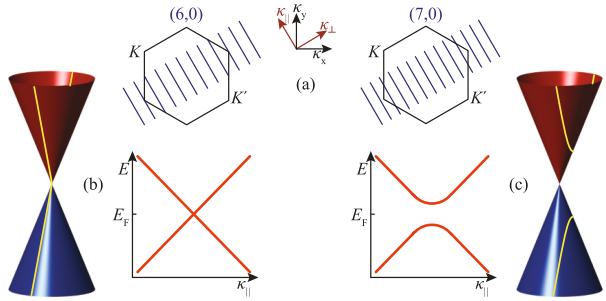

FIGURE 3.3: Sub-bands and dispersion curves at low energy. (a) The zone-folding approximation gives rise to one-dimensional sub-bands via the circumferential boundary conditions [64]. (b,c) Energy dispersion for a metallic nanotube and a semiconducting nanotube. Examples for a metallic with (6,0) chiral indices and semiconducting with (7,0) zig-zag CNTs are shown.

By putting together equations 3.2 and 3.3 it is possible to obtain the energy dispersion:

$$E(\kappa_\parallel) = \pm \frac{2\hbar v_F}{d} \sqrt{\left(\frac{m-n}{3} + p\right)^2 + \left(\frac{\kappa_\parallel d}{2}\right)^2} \tag{3.4}$$

where d is the diameter of the tube. It is clear that $E(\kappa_\parallel = 0) = 0$ if $(m-n)/3 = -p$, so that all armchair tubes are metallic. Note that a small band gap can be created in metallic nanotubes due to nanotube curvature and the strain [65, 66].

3.2 Charge quantization in carbon nanotubes

A quantum dot (QD) is a zero-dimensional system, where electron wave functions are confined in the three directions. For this reason the energy states of this quantum island have only discrete values and often QD are referred to as artificial atoms. The energy-level spacing is given by the interference condition $\Delta E = \frac{hv_F}{2L}$, where L is the length

of the nanotube dot and v_F is the Fermi velocity.

As we just saw in the previous section, a CNT can be considered as a one-dimensional conductor. By contacting a CNT with a source (S), drain (D) and gate (G) metallic contacts, tunnel barriers form at the interfaces. This further reduces the dimensionality of the system, creating a QD in the CNT (see Fig 3.4).

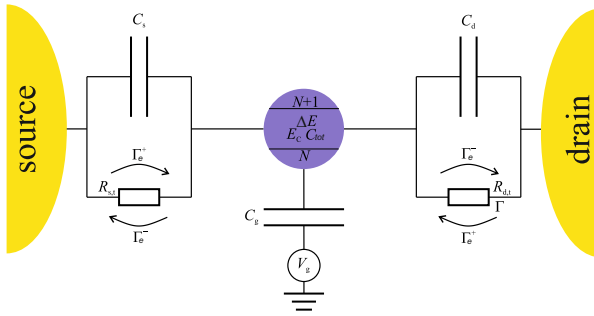

FIGURE 3.4: Schematic drawing of the equivalent circuit. A single quantum dot, characterized by quantized states, is capacitively coupled to source, drain and gate electrodes through the capacitances C_s, C_d and C_g. The coupling is parametrized by the tunnelling rate Γ_e and the tunnelling barrier resistance R_t.

Electrodes can be described as electron reservoirs, from where charges can tunnel in and out of the QD at the tunnelling rate Γ_e. This parameter reflects the coupling between the electrodes and the dot. It depends on the electronic density in the leads and the overlap of the lead and the dot wavefunctions; the latter can be partially tuned with the gate voltage. We must also consider that confining electrons in this small island costs energy because of Coulomb repulsion. To overcome this repulsion when adding one electron, the so-called charging energy $E_c = \frac{e^2}{C_{tot}}$ has to be provided. Here $C_{tot} = C_s + C_d + C_g$ is the total capacitance of the dot which is the sum of the source, drain and gate capacitances to the QD.

When the temperature of the system as well as the coupling of source and drain leads to the dot are sufficiently low, an effect called Coulomb blockade emerges in transport measurements. Indeed there are two major conditions for this effect to take place:

1. The temperature of the system has to be sufficiently low in order to suppress thermally induced fluctuations of the charge number

in the dot. This leads to the following condition:

$$E_c = \frac{e^2}{C_{tot}} \gg k_B T \tag{3.5}$$

2. The number of charges has to be well defined inside the dot. This means that the time for charging and discharging the dot has to be long enough. The typical time to charge or discharge is $\Delta t = R_t \cdot C_{tot}$, where R_t is the resistance of the tunnelling barrier. Using the Heisenberg uncertainty relation, $\Delta E \Delta t = \frac{e^2}{C_{tot}} \cdot R_t C_{tot} = e^2 \cdot R_t > h$. Coulomb blockade emerges when the condition for the tunnelling resistance is:

$$R_t \gg R_K = \frac{h}{e^2} \tag{3.6}$$

where $R_K = 25.813\ \text{k}\Omega$ is the Von Klitzing constant.

These two conditions are necessary to observe Coulomb blockade. It consists in the blockage of the current flow through the quantum dot, unless extra energy is paid externally to accommodate another electron in the next level of the dot.
This scenario was first suggest by Gorter [67] and then by Kulik [68] to explain an anomalous resistance increase of thin granular metallic films at low temperature [69]. Fulton and Dolan [70] later observed Coulomb blockade signature in microscopic metallic devices. More recently Tans [41] showed it for the first time in a carbon nanotube based QD.

3.3 The constant interaction model

The simplest model that explains the energy spectrum of a quantum dot is the constant interaction model (CI). The CI model is based on two main assumptions: (1) electronic interactions inside the dot and between the dot and its environment are constant and parameterized by the total capacitance of the dot C_{tot}, and (2) the single-particle energy-level spectrum (ϵ_i) holds independently of the number of the electrons N [71, 72].
We start by considering that the QD is coupled to the source and drain electrodes via tunnel barriers. (see Fig.3.4). The charge on a conductor i (quantum dot) surrounded by m conductors (source, drain and gate) can be written as:

$$Q_i = \sum_{j=0}^{m} C_{ij} V_j \tag{3.7}$$

where C_{ij} is the capacitance between the quantum dot i to the contact j, and V_j is the electrostatic potential of the contact j.
Defining the dot as $i = 0$, its electrostatic potential reads as:

$$V_0(Q_0) = \frac{1}{C_{tot}} \left(Q_0 - \sum_{j=1}^{m} C_{0j} V_j \right) \tag{3.8}$$

using the self-capacitance of the dot $C_{tot} = C_{00}$, that is equal to the negative sum of all capacitances to the quantum dot $C_{00} = -\sum_{j \neq 0} C_{0j}$.
For the total electrostatic energy of the quantum dot charged with N electrons ($Q_0 = -eN$), we can write:

$$U(N) = \int_0^{-eN} V_0(Q_0) dQ_0 = \frac{e^2 N^2}{2C_{tot}} + eN \left(\sum_{j=1}^{m} \frac{C_{0j}}{C_{tot}} V_j \right) \tag{3.9}$$

To compute the total energy $E(N)$ of the dot, we need to sum $U(N)$ to the values of the single-particle energy (ϵ_i) to take into account the quantum confinement (in the CI model they are independent of N, so they are constant).

$$E(N) = U(N) + \sum_{i=1}^{N} \epsilon_i \tag{3.10}$$

We can now define the electrochemical potential (μ_N) as the energy required to add the Nth electron to the dot. Accordingly μ_N can be written:

$$\mu_N = E(N) - E(N+1) = \epsilon_N + \frac{e^2}{C_{tot}} \left(N - \frac{1}{2} \right) - e \left(\sum_{j=1}^{m} \alpha_j V_j \right) \tag{3.11}$$

where we have introduced the lever arm $\alpha_j = -\frac{C_{0j}}{C_{tot}}$ of the contact j. Specifically, α_g is the gate-lever arm and can be used to convert gate voltage in energy scales. It quantifies the influence of the gate voltage on the electrochemical potential of the dot.
Finally, we can introduce the addition energy $E_{add}(N)$ that represents the change in electrochemical potential once the Nth electron is added to the dot:

$$E_{add}(N) = \mu_N - \mu_{N-1} = \epsilon_N - \epsilon_{N-1} + \frac{e^2}{C_{tot}} = \Delta E + E_c \tag{3.12}$$

Here we recognize the electrostatic contribution given by the charging energy E_c and the energy-level spacing ΔE, both introduced previously.

At this point it is very useful to look at energy diagrams, which are commonly used to visualize what we said so far. In Fig.3.5, the energy diagram of a quantum dot surrounded by source, drain and gate electrodes is shown. In the left panel no level is aligned within the bias window (eV_{sd}, gray area), so that the system is in the Coulomb blockade regime with N electrons in the dot and no single-electron tunnelling event is allowed. However, the dot energy level can by pulled down by means of the gate. In the right panel an energy level falls inside the bias window. A current can flow through the quantum dot as a sequential tunnelling of electrons. The number of charge carriers oscillates between N and $N+1$. By tuning the gate voltage electrons can be added into the dot one by one. For this reason this kind of devices are also known as single-electron transistors (SET).

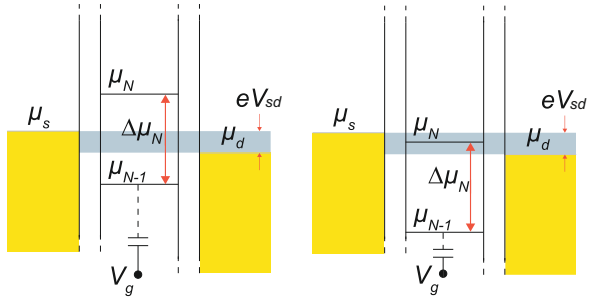

FIGURE 3.5: Schematic diagram of the electrochemical potential levels of a QD coupled to source and drain with their electrochemical potential (μ_D and μ_S). In the left panel the dot is in a stable configuration with $N-1$ electrons. A small bias V_{sd} is applied but there is no current through the dot. In the right panel, by means of the gate voltage, a dot level is shifted down in the bias window. The number of electrons in the dot oscillates between $N-1$ and N, so that conduction is established.

If we measure the current flowing through such a device, while sweeping the gate voltage V_g (with a small bias V_{sd}), the result is a series of oscillations, referred as Coulomb oscillations, see Fig.3.6. Typically, for a CNT single quantum dot device the conductance is modulated by the gate voltage with two different values. This reflects the degeneracy of the spin and the valley (K and K'). In Fig.3.6(a) a fourfold periodicity is shown. This is due to the valley (K and K') and spin (up and down) degeneracy which, in this case, are not lifted. In Fig.3.6(b) instead, the valley degeneracy is lifted. This may happen because of the scattering at the electrodes, which induce a orbital mismatch (between K and K') in the CNT band-structure.

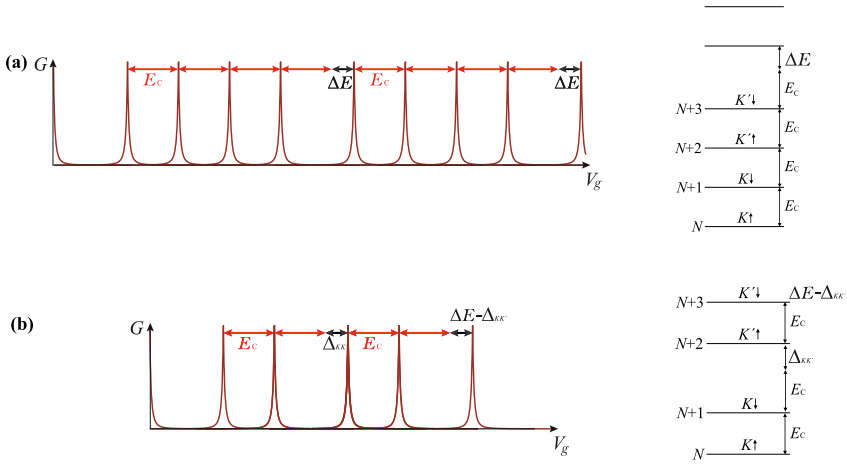

FIGURE 3.6: Schematic representation of the dot conductance G as a function of the gate voltage V_g. (a) In this case each electronic shell contains four levels due to spin and valley degeneracies. (b) Two fold symmetry is due to spin degeneracy while the orbital one is lifted.

3.3.1 Quantum dot spectroscopy: stability diagrams and Coulomb diamonds

In order to perform a precise spectroscopy of a quantum dot, a finite voltage bias V_{sd} is often applied in transport measurements. We assume a symmetric bias to the source and drain contacts, which means $\mu_S = \mu_0 + eV_{sd}/2$ and $\mu_D = \mu_0 - eV_{sd}/2$ (where μ_0 is the electrochemical potential in both contacts without bias). We now estimate the conditions to have Coulomb blockade current, that is, when the charge number remains constant in time. For $V_{sd} > 0$:

$$\mu_N < \mu_0 - eV_{sd}/2$$
$$\mu_{N+1} > \mu_0 + eV_{sd}/2$$

and for $V_{sd} < 0$:

$$\mu_N < \mu_0 + eV_{sd}/2$$
$$\mu_{N+1} > \mu_0 - eV_{sd}/2$$

Plugging this group of inequalities in the equation 3.11 we get the so-called Coulomb diamonds in the measurement of G as a function of V_{sd} and V_g (white areas, see Fig.3.7) where there are no tunnelling events. We want to note that imposing $\mu(N, V_g, V_{sd} = 0) = 0$ in equation 3.11 we obtain that the distance between two consecutive Coulomb peaks (points of the Coulomb diamonds at zero-bias) are spaced by E_{add}/α_g. The borderlines cross at $eV_{sd} = E_{add}$ (half-height of the diamond). Diamond slopes are related to source and drain capacitances. The positive one is $\frac{C_g}{C_g+C_d}$ (when the drain is grounded) and the negative one is $-\frac{C_g}{C_s}$. The gate capacitance can be determined from the separation in gate voltage ΔV_g between two Coulomb blockade peaks when the two associated levels are separated by E_c only. This can be done using $C_g = \frac{e}{\Delta V_g} = \frac{e^2\alpha_g}{E_c}$. Additional lines in the non blockade regions can appear alongside the borderline (blue dashed lines in the dark purple areas). This occurs when an excited state enters in the bias window.

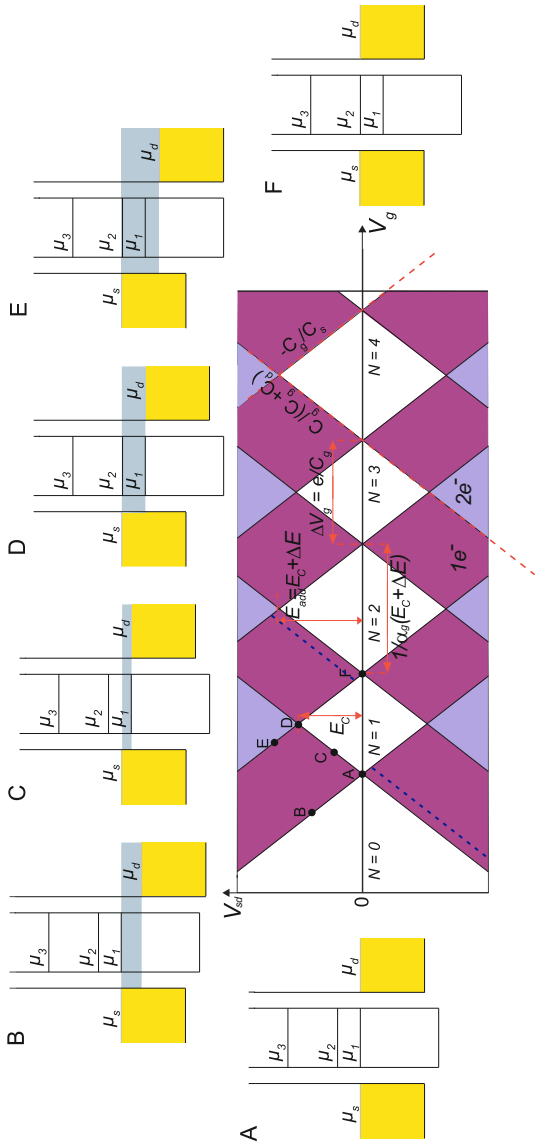

FIGURE 3.7: Schematic illustration of a charge stability diagram. Assuming spin degeneracy for free electrons in a system without valley degeneracy. In the white areas, known as Coulomb diamonds, the system is in the Coulomb blockade regime and the number of electrons in the dot is fixed. In the dark and purple areas the levels of the dot are in the bias window so that the electron number can fluctuate. Points from A to F are associated to different configurations in the electrochemical potential diagrams.

3.4 Coulomb oscillation lineshape

The lineshape of a Coulomb blockade peak in the measurement of G as a function of V_g depends on three different quantities: the temperature T, the tunnelling rate Γ_e and the electronic level spacing ΔE. The Fermi-Dirac distribution in the source and drain reservoirs at finite T can lead to a broadening of the measured lineshape. The intrinsic linewidth $\hbar\Gamma_e$ of the energy level is set by the Heisenberg's uncertainty relation containing the finite lifetime $\tau \approx 1/\Gamma_e$ of the dot.

3.4.1 Weak coupling: Thermal broadening ($\hbar\Gamma_e \ll k_B T \ll E_c, \Delta E$)

In this regime, the thermal broadening of the Fermi-Dirac distributed electrons in the electrodes determines the lineshape. Following the treatment of Beenaker [71], the energy levels in the dot are treated as delta functions and a master equation for the probability of the system $p_i(t)$ to be in the state i at the time t can be written. It gives us an expression for the conductance G for a single level:

$$G^{(i)} = \frac{e^2}{h}\frac{\Gamma_S\Gamma_D}{\Gamma_S+\Gamma_D}\frac{1}{4k_BT\cosh^2\left(\frac{\alpha_g(V_g^{(i)}-V_g)}{2k_BT}\right)} \tag{3.13}$$

where $V_g^{(i)}$ is the position of the Coulomb peak on the gate voltage axis, and $\Gamma_e = \Gamma_S + \Gamma_D$, where S and D stand for source and drain. We can notice many things. When increasing the temperature the conductance height of the peak decays with $1/T$. The full width at half maximum (FWHM) in energy units is FWHM$= 4k_BT(\sqrt{2}) \approx 3.5k_BT$. Another peculiar feature of this regime is the random conductance height of the different Coulomb peaks as the gate voltage is swept. This is because the peak height reflects the overlap between the wave function of the electron state in the dot and that in the electrodes [73]. In the high temperature limit when $\hbar\Gamma_e, \Delta E \ll k_BT \ll E_c$, the thermal energy is larger than the single level spacing so that several single-particle levels contribute to transport. In this high temperature regime the FWHM remains proportional to the temperature but with a different factor, FWHM $\approx 4.5k_BT$.

3.4.2 Strong coupling: Tunnelling broadening ($k_BT \ll \hbar\Gamma_e \ll E_c, \Delta E$)

This regime cannot be treated as the previous one. The transport mechanism is related to the one of resonant transmission through a double barrier [74]. The lineshape of the conductance can be described with the Breit-Wigner expression [75]:

$$G = \frac{4e^2}{\hbar}\left(\frac{1}{\Gamma_S}+\frac{1}{\Gamma_D}\right)^{-1}\frac{\hbar^2\Gamma_e}{\alpha_g^2(V_g^{(i)}-V_g)^2+(\hbar\Gamma_e/2)^2} \tag{3.14}$$

Neither the height nor the width of the conductance peak are temperature dependent. In this case the FWHM is given by the tunnelling-rate-induced level broadening $\hbar\Gamma_e$.

3.5 Co-tunnelling and Fabry-Pérot interference

In the previous section, we considered only first-order tunnelling events in the transport through a quantum dot. Now we deal with higher-order processes leading to additional features in the dot spectroscopy. When the tunnel barriers become more transparent, the dot starts to be more coupled to the leads, so that the tunnelling rate Γ_e onto and off the dot increases. The Coulomb interaction is still important but co-tunnelling events start to kick in. The term co-tunnelling generally refers to ridges of conductance appearing in the blockade regions of the Coulomb diamond. Cotunneling processes can be either elastic or inelastic. The first involves the ground state of the QD while the latter appear at finite V_{sd} and involves ground and excited states of the QD. Another important higher-order process is the Kondo effect.
A detailed analysis of this phenomenon would go far beyond the scope of this chapter. During many decades, it was the subject of considerable theoretical [76, 77] and experimental [78–80] works. The Kondo-spin version involves the formation of a spin singlet between an electron in the dot and another one in the lead, with a spin-flip of the dot-electron at the end of the process. Similarly, the valley version produces a flip from K to K'. The Kondo effect in CTN exists in three versions: SU(2)-spin, SU(2)-orbital and SU(4) including the flip of both degrees of freedom. It remains a very open and interesting many-body problem, largely investigated in the community [81].

To conclude this chapter, we briefly mention the Fabry-Pèrot electron interference regime. When the tunnelling rate $\hbar\Gamma_e$ becomes much larger than the charging energy E_c, the dot can be considered "open" and interference effects emerge. Assuming ballistic transport along the nanotube, interference between right- and left- moving electron waves lead to peculiar oscillating patterns in transport measurements [46].

Chapter 4

Ultra-sensitive displacement noise measurements

Parts of this chapter have been published in:
Ultrasensitive displacement noise measurement of carbon nanotube mechanical resonators
S. L. De Bonis*, C. Urgell*, W. Yang, C. Samanta, A. Noury, J. Vergara-Cruz, Q. Dong, Y. Jin and A. Bachtold
Nano Letters, 18, 5324, (2018)

In this chapter, we report on an ultra-sensitive scheme based on a RLC resonator and a low-temperature amplifier to detect nanotube vibrations. We also show a new fabrication process of electromechanical nanotube resonators to reduce the separation between the suspended nanotube and the gate electrode down to $\sim$ 150 nm. These advances in detection and fabrication allow us to reach 0.5 pm/$\sqrt{\text{Hz}}$ displacement sensitivity. Thermal vibrations cooled cryogenically at 300 mK are detected with a signal-to-noise ratio as high as 17 dB. We demonstrate 4.3 zN/$\sqrt{\text{Hz}}$ force sensitivity, which is the best force sensitivity achieved thus far with a mechanical resonator. Our work is an important step towards imaging individual nuclear spins and studying the coupling between mechanical vibrations and electrons in different quantum electron transport regimes.

*Equal contribution

4.1 Introduction

The smallest operational mechanical resonators are based on low-dimensional materials, such as carbon nanotubes [38], graphene [82–84], semiconducting nanowires [85–88], and levitated particles [30, 89]. Such resonators are fantastic sensors of external forces [40, 90–92] and the adsorption of mass [22, 93, 94]. They also provide a versatile platform for fundamental science, including the study of noise [53, 95, 96], nonlinear phenomena [54, 55, 97–99], electron-phonon coupling [7–9, 42, 100], and light-matter interaction [101, 102]. The greatest challenge with these tiny resonators is to transduce their mechanical vibrations into a measurable electrical or optical output signal. Novel detection methods have been continuously developed over the years [32, 37, 103–116]. This effort has often been paid off with the improvement of sensing capabilities and the measurement of unexpected phenomena.

Care has to be taken to avoid heating when improving the detection of the motion. The transduction of the motion is achieved by applying some input power to the resonator. In the case of nanotube resonators, the input power is usually related to the oscillating voltage applied across the nanotube [38] or the laser beam illuminating the nanotube [107, 116]. The displacement sensitivity becomes better when increasing the input power. However, the input power has to be kept low enough to avoid electrical Joule heating and optical adsorption heating. Heating is especially prominent in tiny objects, such as nanotubes, because of their small heat capacity. Heating is detrimental, because it deteriorates the force and the mass sensitivity and increases the number of quanta of vibrational energy.

In this chapter, we report on a novel detection method that allows us to measure the mechanical vibrations of nanotube resonators with an unprecedented sensitivity. The detection consists in measuring the electrical signal employing a RLC resonator and a high electron mobility transistor (HEMT) amplifier cooled at liquid-helium temperature. In order to further improve the detection, we optimize the fabrication process to enhance the capacitive coupling between the ultraclean carbon nanotube and the gate electrode. This allows us to achieve 1.7 $\mathrm{pm}/\sqrt{\mathrm{Hz}}$ displacement sensitivity and 4.3 $\mathrm{zN}/\sqrt{\mathrm{Hz}}$ force sensitivity when the temperature of the measured eigenmode is 120 mK. At higher vibration temperature, the resonator can be probed with larger input power, so that the sensitivity reaches 0.5 $\mathrm{pm}/\sqrt{\mathrm{Hz}}$ at 300 mK.

4.2 Fabrication

We use a new fabrication process to grow ultraclean carbon nanotube resonators suspended over shallow trenches. Figure 4.1 shows a $\sim$

1.3 μm long nanotube contacted electrically to two electrodes and separated from the local gate electrode by $\sim$ 150 nm. The electrodes made from platinum with a tungsten adhesion layer are evaporated on top of silicon dioxide grown by plasma-enhanced chemical vapour deposition. Nanotubes are grown by the 'fast heating' chemical vapour deposition method in the last fabrication step [117] (see AppendixC). This method consists in rapidly sliding the quartz tube through the oven under a flow of methane, so that the sample moves from a position outside of the oven to the center of the oven, whose temperature is $T_{\text{growth}} = 820\ ^{\circ}\text{C}$. This growth process has two assets compared to the usual growth of nanotube resonators[32]. It allows us to suspend nanotubes over wide trenches. In addition, the electrodes are less prone to melt and change shape.

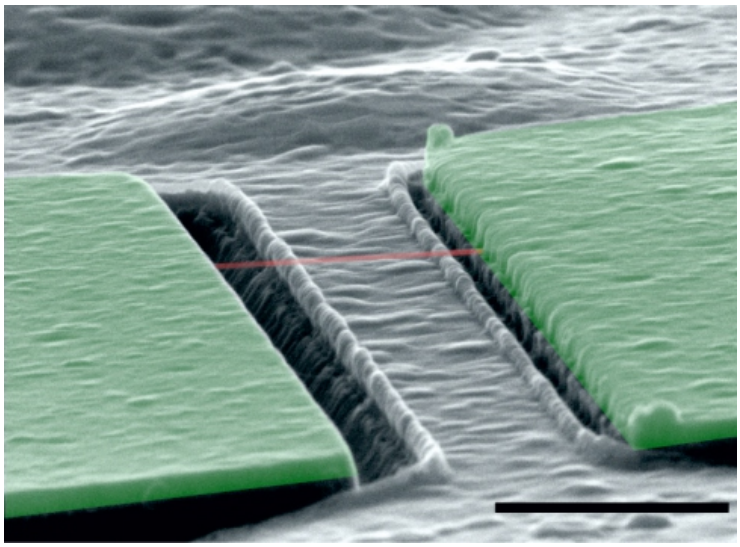

FIGURE 4.1: False-colour scanning electron microscopy image of a typical nanotube resonator fabricated with the 'fast heating' chemical vapour deposition method. The $\sim$ 20 nm high ridges at the edges of the gate electrodes are attributed to resist residues. The scale bar is 1 μm.

4.3 Detection of mechanical vibrations

Mechanical vibrations are detected electrically using a RLC resonator and a HEMT amplifier cooled at liquid-helium temperature (Fig.4.2(a)). Displacement modulation is transduced capacitively into current modulation by applying an input oscillating voltage V_{sd}^{ac} across the nanotube [32, 38, 40]. The frequency $\omega_{sd}/2\pi$ of the oscillating voltage is set to match $\omega_{sd} = \omega_m \pm \omega_{RLC}$, where $\omega_m/2\pi$ is the resonance frequency of the nanotube resonator and $\omega_{RLC}/2\pi = 1.73$ MHz the resonance frequency of the RLC resonator. Driven vibrations are measured with the two-source method [38]. Thermal vibrations are measured by recording the current noise at $\sim \omega_{RLC}$ [32, 40]. These current noise measurements are similar to those recently carried out on quantum electron devices [118–120]. The RLC resonator and the HEMT amplifier [121] allow us to reduce the current noise floor at $\sim \omega_{RLC}$ down to 38 fA$/\sqrt{\text{Hz}}$ below $\sim$ 100 mK (Fig.4.2(b)). The current noise floor is temperature dependent above $\sim$ 100 mK because of the Johnson-Nyquist noise of the impedance of the RLC resonator. Below $\sim$ 100 mK, the Johnson-Nyquist noise becomes vanishingly small. The noise floor is then given by the current noise (21.6 fA$/\sqrt{\text{Hz}}$) and the voltage noise (0.125 nV$/\sqrt{\text{Hz}}$) of the HEMT amplifier and the voltage noise of the room temperature amplifier. The gain of the HEMT amplifier is set at 6.4. The inductance of the circuit is given by the 66 μH inductance soldered onto a printed-circuit board (PCB). The 129 pF capacitance measured from the RLC resonance frequency comes from the capacitance of the radio-frequency cables and the low-pass filter VLFX-80 between the device and the HEMT. The 7.79 kΩ resistance obtained from the 156 kHz line-width of the RLC resonator is attributed to the 10 kΩ resistance soldered onto the PCB and the input impedance of the HEMT amplifier.
The details of the noise characterization are presented in the AppendixA.

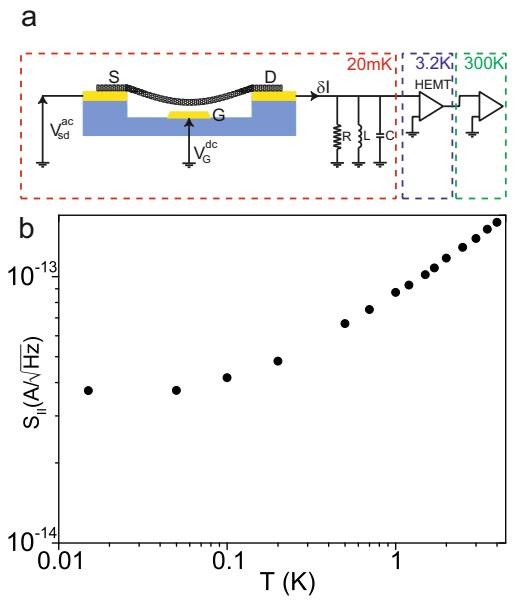

FIGURE 4.2: Electrical circuit for the detection of the vibrations. (a) Schematic of the measurement of the nanotube vibrations using the RLC resonator and the HEMT amplifier cooled at 3.2 K. The base temperature of the cryostat is $\sim$ 20 mK. An oscillating voltage with amplitude V_{sd}^{ac} is applied between electrodes S and D, and a constant voltage V_G^{dc} is applied to electrode G. (b) Temperature dependence of the current noise floor of the circuit measured at ω_{RLC}

4.4 Measurements of the fundamental mechanical mode

The lowest-lying flexural eigenmodes are identified by capacitively driving the resonator with an oscillating force and measuring the motion with the two-source method [38]. The dependence of the resonance frequency as a function of the static voltage V_G^{dc} applied to the gate electrode demonstrates that the measured resonance is related to a mechanical eigenmode of the nanotube (Fig.4.3(a)). The amplitude of the lowest-frequency resonance is much larger than that of the second detected resonance (Fig.4.3(b)). We conclude that the detected eigenmodes are polarized in the direction perpendicular to the surface of the gate electrode to a good approximation, and that eigenmodes polarized in the parallel direction cannot be detected. The thermal vibrations are recorded at the base temperature of the dilution cryostat (Fig.4.3(c)). We switch off the driving force, and the displacement

noise is recorded with the method described in Refs. [32, 40]. The quality factor is Q =627,000 with the gate voltage set at V_G^{dc}=-0.21 V. We choose this gate voltage so that the electron transport is not in the Coulomb blockade regime. The Q-factor becomes lower at more negative gate voltages because of electrical losses [122] and at positive gate voltages due to Coulomb blockade [7].
We now recall in more details the important relations for the transduction of current into displacement [32]. We use the fact that the mechanical eigenmode is polarized in the direction perpendicular to the surface of the gate electrode, as just discussed. The current δI at the frequency close to the difference between the mode eigenfrequency and the frequency of the source-drain voltage is

$$\delta I = \beta \delta z, \tag{4.1}$$

$$\beta = \frac{1}{2}\frac{dG}{dV_G} V_G^{dc} V_{sd}^{ac} \frac{C_G'}{C_G}. \tag{4.2}$$

Here, δz is the displacement of the nanotube, dG/dV_G is the transcondutance, V_G^{dc} is the static gate voltage, V_{sd}^{ac} is the amplitude of the oscillating source-drain voltage, C_G is the capacitance between the nanotube and the gate electrode, and C_G' is the derivative of C_G with respect to z. We measure $dG/dV_G = 1.4 \times 10^{-3}$ S/V at the gate voltage V_G^{dc}=-0.21 V.

We estimate the capacitance C_G from the separation $\Delta V_G^{dc} = 16.8 \pm 0.6$ mV between two conductance peaks in the Coulomb blockade regime at large positive V_G^{dc} values. We obtain $C_G = e/\Delta V_G^{dc} = 9.5 \pm 0.3 \times 10^{-18}$ F. We quantify C_G' using the relation

$$C_G' = \frac{C_G}{d \ln(2d/r)} = (1.11 \pm 0.17) \times 10^{-11} \mathrm{F/m}, \tag{4.3}$$

with $d = 150 \pm 10$ nm for the separation between the nanotube and the gate electrode and $r = 1 \pm 0.3$ nm for the radius of the nanotube.

We measure the dependence of the variance of the displacement $\langle \delta z^2 \rangle$ on the cryostat temperature T (Fig.4.3(d)). The linear dependence is in agreement with the equipartition theorem $m\omega_m^2 \langle \delta z^2 \rangle = k_b T$, where m is the effective mass of the resonator and $\omega_m/2\pi$ is the resonance frequency of the eigenmode. We obtain $m = 8.6 \pm 3.6$ ag from the slope, which is consistent with the mass expected for a $\sim$ 1.3 μm long nanotube. Below $\sim$ 120 mK the eigenmode does not thermalize well with the cryostat (see again Fig.4.3(d)). The origin of this poor thermalization at low temperature may be related to a non-thermal force noise, such as the electrostatic force noise related to the voltage noise in the device [123].

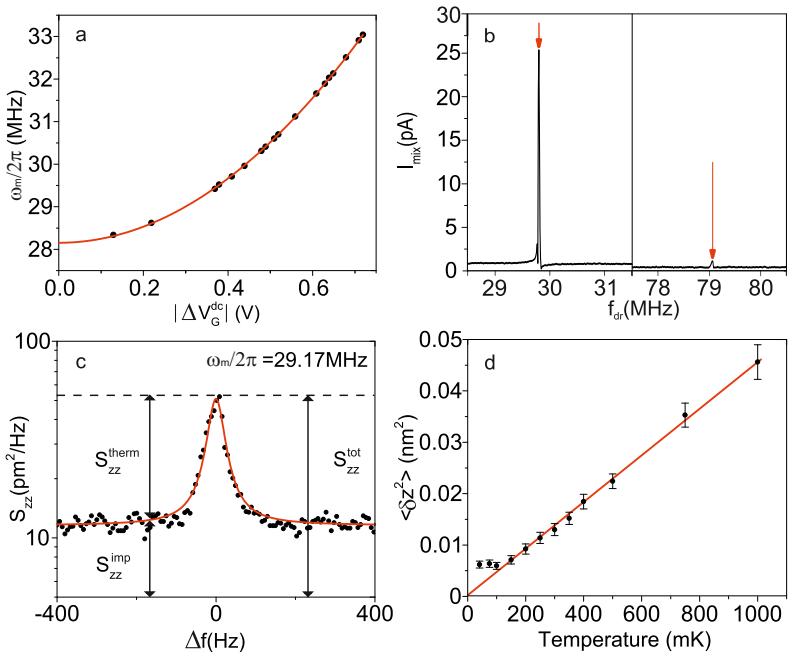

FIGURE 4.3: Driven and thermal vibrations of the nanotube resonator. (a) Gate voltage dependence of the resonance frequency of the fundamental eigenmode. The small positive offset voltage $V_{\rm off} = 0.119$ V due to the work function difference between the nanotube and the gate electrode is subtracted from the applied $V_{\rm G}^{\rm dc}$ value. The red line is a parabolic fit. (b) Driven response of the two lowest-frequency detected mechanical eigenmodes as a function of the drive frequency measured with the two-source method. The resonances are indicated by two red arrows. (c) Spectrum of the displacement noise of the fundamental eigenmode measured at the base temperature of the cryostat when applying $V_{\rm G}^{\rm dc}$=-0.21 V and $V_{\rm sd}^{\rm ac} = 40$ μV. The resonance frequency $\omega_{\rm m}/2\pi$ is given in the figure. The red line is a Lorentzian fit. (d) Variance of the displacement measured as a function of cryostat temperature.

4.5 Force sensitivity and displacement sensitivity

The force sensitivity derived from the noise spectrum in Fig.4.3(c) is $\sqrt{S_{\rm FF}} = 4.3 \pm 2.9$ zN$/\sqrt{\rm Hz}$. The force sensitivity is given by the sum of the thermal force noise $S_{\rm FF}^{\rm therm}$ and the imprecision force noise of the detection $S_{\rm FF}^{\rm imp}$, $S_{\rm FF} = S_{\rm FF}^{\rm therm} + S_{\rm FF}^{\rm imp}$. Because the thermal resonance is described by a Lorentzian line shape, the force sensitivity is quantified from the total displacement noise at resonance frequency

using $S_{FF} = S_{zz}(\omega_m)/|\chi(\omega_m)|^2$ [1] with the mechanical susceptibility $|\chi(\omega_m)| = Q/m\omega_m^2$. The force sensitivity is given to a large extent by the thermal force noise of the resonator $\sqrt{S_{FF}^{th}} = \sqrt{4k_bTm\omega_m/Q} = 4.0\,\mathrm{zN}/\sqrt{\mathrm{Hz}}$, which is the fundamental limit of the force sensitivity set by the fluctuation-dissipation theorem. The noise of the imprecision in the detection contributes to the force sensitivity by a low amount. The error bar in the estimation of the force sensitivity originates essentially from the uncertainty in the nanotube diameter and the separation between the nanotube and the gate electrode. Table 4.1 shows that the force sensitivity measured here is better than what is reported with resonators micro-fabricated from bulk material [124–126], and resonators based on nanotube [40], semiconducting nanowire [91, 92, 127], graphene [123], and levitating particles [53]. In [32], the reported thermal force noise is lower, but the cross-correlation noise measurement does not quantify the force noise due to the imprecision in the detection, so that the total force noise cannot be quantified.

We now look at how the displacement noise is affected by the input power related to the oscillating voltage V_{sd}^{ac}. The variance of the displacement increases abruptly above $V_{sd}^{ac} \simeq 80\ \mu$V when the cryostat is at base temperature (see Fig.4.4(c)). This indicates the rise of the thermal vibration amplitude due to Joule heating. By contrast, the variance of the displacement remains constant over the whole range of V_{sd}^{ac} that we apply when the cryostat temperature is set at 300 mK (see Fig.4.4(d)).

Our detection scheme allows us to reach an excellent displacement sensitivity for input powers below the onset of Joule heating. The displacement sensitivity is given by the noise floor of the spectrum of thermal vibrations. In Figures 4.4(e,f) it is evident that the displacement sensitivity gets better when increasing V_{sd}^{ac}. The displacement sensitivity at base temperature is $1.7\ \mathrm{pm}/\sqrt{\mathrm{Hz}}$ at $V_{sd}^{ac} = 80\ \mu$V before that Joule heating starts to increase the variance of the displacement. When the cryostat temperature is set at 300 mK, the displacement sensitivity is $0.5\ \mathrm{pm}/\sqrt{\mathrm{Hz}}$ at the largest V_{sd}^{ac} value that we apply. The corresponding signal-to-noise ratio in the spectrum of thermal vibrations is 17 dB (see Fig.4.4(b)).

The measured displacement sensitivity S_{zz}^{imp} scales as $(1/V_{sd}^{ac})^2$ (see Figures 4.4(e,d)), indicating that S_{zz}^{imp} is limited by the noise of the detection circuit and not by the electron shot noise through the nanotube [128].

The Q-factor in Fig.4.4(a) is lower than that in Fig.4.3(c) due to an unknown reason while cycling the cryostat through room temperature;

[1] The spectral density S_{zz} of the displacement noise is obtained from the measured spectral density of the current noise using equations 4.1 and 4.2. The displacement sensitivity S_{zz}^{imp} is estimated from the current noise floor S_{II}^{imp} in the measured spectrum using $S_{zz}^{imp} = \frac{1}{\beta^2} S_{II}^{imp}$.

the resonance frequency and the mass are not modified by the thermal cycling.

$\sqrt{S_{FF}^{th}}$ ($N/\sqrt{Hz}$)	$\sqrt{S_{FF}^{imp}}$ ($N/\sqrt{Hz}$)	$\sqrt{S_{FF}}$ ($N/\sqrt{Hz}$)	Description
$4.0 \cdot 10^{-21}$	$1.6 \cdot 10^{-21}$	$4.3 \cdot 10^{-21}$	Nanotube (this work)
$2.0 \cdot 10^{-20}$	negligible	$2.0 \cdot 10^{-20}$	levitating particle [53]
$2.7 \cdot 10^{-19}$	$2.7 \cdot 10^{-19}$	$3.9 \cdot 10^{-19}$	Graphene [123]
$1.0 \cdot 10^{-18}$	negligible	$1.0 \cdot 10^{-18}$	Silicon nanowire [127]
$5.0 \cdot 10^{-18}$	negligible	$5.0 \cdot 10^{-18}$	GaAs/AlGaAs nanowire [92]
$1.6 \cdot 10^{-19}$	$1.0 \cdot 10^{-19}$	$1.9 \cdot 10^{-19}$	Microfabricated ladder [126]
$5.1 \cdot 10^{-19}$	negligible	$5.1 \cdot 10^{-19}$	Microfabricated beam [124]
$2.0 \cdot 10^{-17}$	negligible	$2.0 \cdot 10^{-17}$	Microfabricated trampoline [125]
$1.2 \cdot 10^{-20}$	unknown	unknown	Nanotube [40]
$\sim 1 \cdot 10^{-21}$	unknown	unknown	Nanotube [32]

TABLE 4.1: Thermal force noise S_{FF}^{th}, force noise due to the imprecision of the detection S_{FF}^{imp}, and total force sensitivity S_{FF} for different resonators. The three force noises are related by $S_{FF}^{th} + S_{FF}^{imp} = S_{FF}$.

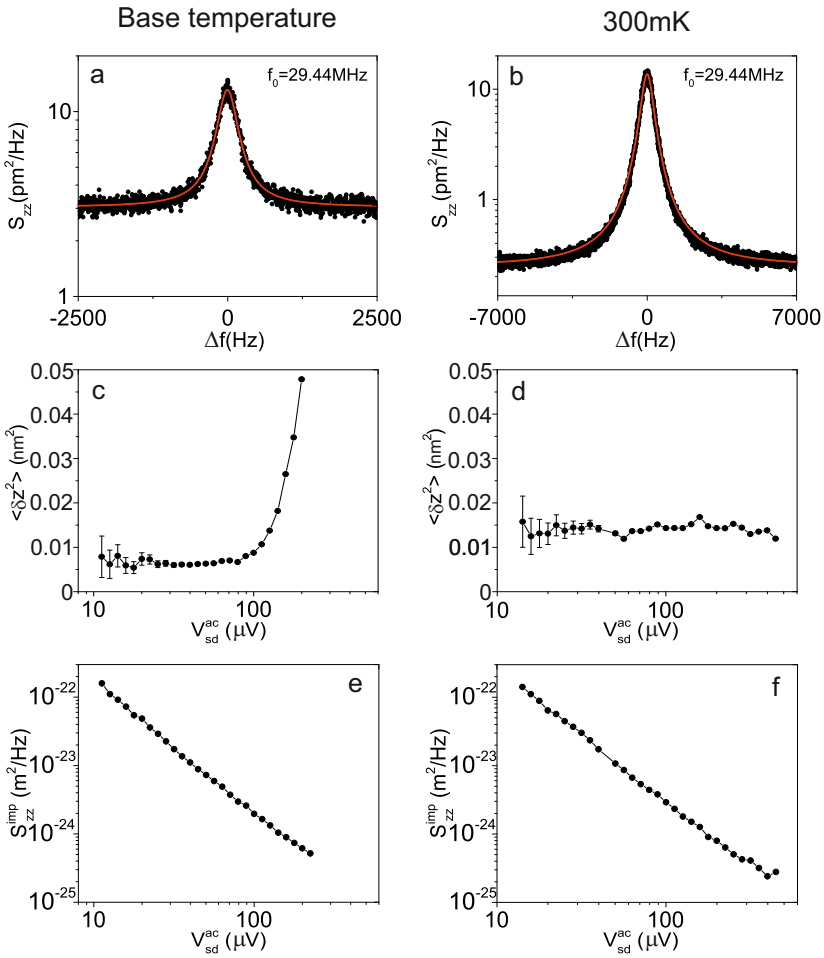

FIGURE 4.4: Spectrum of the displacement noise modified by the oscillating voltage with amplitude $V_{\rm sd}^{\rm ac}$ applied across the nanotube. (a) Spectrum of the displacement noise of the fundamental eigenmode measured at the base temperature of the cryostat when applying $V_{\rm G}^{\rm dc}$=-0.255 V and $V_{\rm sd}^{\rm ac} = 70$ μV. (b) Same as (a) but with the cryostat temperature set at 300 mK and $V_{\rm sd}^{\rm ac} = 400$ μV. The red lines are Lorentzian fits. (c,d) Dependence of the variance of the displacement on $V_{\rm sd}^{\rm ac}$ measured at the base temperature of the cryostat and 300 mK. (e,f) Dependence of the displacement sensitivity on $V_{\rm sd}^{\rm ac}$ measured at the base temperature of the cryostat and 300 mK.

4.6 Conclusions and outlook

In conclusion, we report on a detection scheme of nanotube resonators with an unprecedented displacement sensitivity. It allows us to reach

4.3 zN/$\sqrt{\text{Hz}}$ force sensitivity, which surpasses what has been achieved with mechanical resonators to date. This high force sensitivity is an important step towards detecting individual nuclear spins with nuclear magnetic resonance measurements [28, 29]. The coupling between mechanical vibrations and spins can be achieved by applying a gradient of magnetic field that is generated with the current biased through the gate electrode in Fig.4.1 [127]. In this context, the new fabrication process of nanotube resonators presented here is useful for increasing the gradient of the magnetic field, since it reduces the separation between the current-carrying electrode and the nanotube down to $\sim$ 150 nm. The device layout might also allow us to carry out magnetic resonance force microscopy (MRFM) measurements to image the location of individual nuclear spins adsorbed along the nanotube. Imaging can be done by periodically applying radio-frequency pulses though the current-carrying electrode [129]. Moreover, the advances in fabrication and detection described in this chapter offer new possibilities for studying the strong coupling between electrons and vibrations in nanoscale resonators [12, 130–132]. In the Coulomb blockade regime, the system has been predicted to feature a transition towards a mechanically bistable and blocked-current state [132–135]. This hitherto unobserved transition is expected to occur at higher temperature for shorter separation between the nanotube and the gate electrode [132]. The high quality displacement noise spectra reported here might allow us to study this transition in details [132] as well as the different cooling schemes that have been proposed theoretically using different quantum electron transport regimes [136–140].

Chapter 5

Tunable polarons in a carbon nanotube electromechanical resonator

Parts of this chapter will be submitted in:
Tunable polarons in a carbon nanotube electromechanical resonator
S. L. De Bonis*, C. Samanta*, W. Yang, C. Urgell, B. Stamenic, B. Thibeault, F. Pistolesi and A. Bachtold

In the work described in this chapter, we strongly couple the fundamental phonon mode of a suspended nanotube to the two electron states involved in single-electron tunnelling (SET). The resulting potential of the phonon mode is highly nonlinear at the lowest measured temperature, which corresponds to $\simeq 78$ quanta. This enables us to demonstrate the formation of polarons in a nanotube electromechanical resonator. The polaronic nature of charge carriers results in the reduction of the electrical conductance by up to about half its value. The electron-phonon interaction suppresses the resonance frequency of the fundamental phonon mode by up to 25%. Our device is in the so-called ultra-strong coupling regime, where the electromechanical coupling per phonon is one order of magnitude larger than the resonance frequency. Our work establishes nanotube resonator as a possible platform for the demonstration of mechanical quantum bits.

*Equal contribution

5.1 Introduction to polaron physics in electromechanical resonators

Polarons are quasiparticles introduced by Landau and Pekar to describe electrons coupled to phonons [141]. An electron moving in a crystal lattice is dressed by a phonon cloud due to the electrostatic interaction between the electron and the crystal ions (Fig.5.1(a)). This tends to increase the electron mass and to lower the device mobility. Polarons account for transport measurements in a large number of bulk crystals [141], but the electron-phonon interaction is difficult to modify in these systems.

Polarons are expected to emerge in a single-electron tunnelling (SET) device strongly coupled to a mechanical (phonon) mode [132–134, 142, 143]. The two states with N and $N+1$ electrons in a SET island are associated with two different equilibrium positions, as depicted in Fig.5.1(b). We tune the average charge in the island to $N+\frac{1}{2}$ using the voltage $V_{\rm G}^{\rm dc}$ applied to the gate electrode, so that the system fluctuates between the N and $N+1$ electron states. We consider that the corresponding electronic rate $\Gamma_{\rm e}$ is much faster than the mechanical resonance frequency $\omega_{\rm m}$. In this adiabatic regime, the nanotube moves much slower than electrons. This effectively results in a symmetric double-well potential for the mechanical displacement at low temperature, with the minima given by the equilibrium positions associated to the N and $N+1$ states (Fig.5.1(c), top). The mechanical displacement experiences thermal fluctuations around the two minima. The probability distribution of the position consists of two Gaussians with the width given by the equipartition theorem (Fig.5.1(c), bottom). Upon increasing the temperature, there is a transition from a double-well potential to the usual harmonic potential of mechanical resonators (see Fig.5.1(c), top). This occurs when the width of the two Gaussians becomes similar to the separation between the two equilibrium positions, that is, when the thermal energy $k_{\rm B}T$ becomes comparable to the polaronic energy $\varepsilon_{\rm p} = F_{\rm e}^2/k$ (Fig.5.1(c)). Here, $\varepsilon_{\rm p}$ is the relevant parameter to quantify the strength of the electron-phonon interaction, $F_{\rm e}$ is the additional electrostatic force acting on the resonator when adding one electron onto the island (see AppendixB (B.2)), and k is the spring constant of the mechanical mode. A hallmark of electromechanical SET devices is that the electron-phonon interaction strength can be widely tuned by electrostatic means. More importantly, the experimental realization of a nonlinear mechanical potential as described here with the resonator approaching the quantum regime has been a long-sought-after goal in electro- and optomechanics [144].

The nature of polarons in SET devices can have a strong effect on both the electrical conductance of the device and the resonance frequency of the mechanical vibrations. The electronic level of the nanotube fluctuates in energy because of the combination of the thermal

fluctuations of the mode displacement z and the electron-phonon coupling described by the Hamiltonian $H = -F_e n z$, where n is the charge operator of the SET island (see AppendixB). At high temperature, the energy distribution of the electronic level features one broaden peak at the Fermi energy. When reducing the temperature through the transition $\varepsilon_p \sim k_B T$, the peak is split in two Gaussians (see Fig.5.1(d)), so that the electron transmission through the device is reduced compared to the transmission with no electron-phonon interaction. There is also a strong suppression of the mechanical resonance frequency at the transition. Indeed, the potential curvature near zero displacement goes to zero at the transition when $\varepsilon_p \sim k_B T$ (Fig.5.1(c), top). Despite a large number of experimental studies [5, 7–9, 12, 15, 42–44, 145, 146], the renormalisation of the electrical conductance has not been observed thus far. Moreover, the reduction of the resonance frequency has always been modest, indicating that measurements have been carried out in the weak electron-phonon interaction regime when $\varepsilon_p / k_B T \ll 1$.

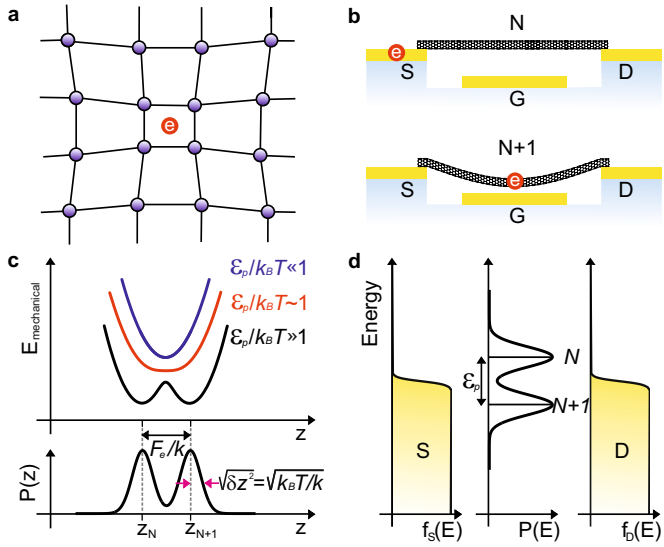

FIGURE 5.1: Electrical and mechanical properties of polarons. (a) Polaron quasi-particle formed by an electron in an ionic crystal lattice. (b) The N and $N+1$ electron states are associated with two different equilibrium positions of the nanotube due to the electrostatic interaction with the gate (G). (c) Double-well potential of the mechanical displacement at low temperature. The separation between the two equilibrium positions is $\Delta z_e = F_e/k$. The probability distribution of the position in the bottom panel consists of two overlapping Gaussians with variance $\delta z^2 = k_B T/k$. There is a crossover from a double-well potential to a harmonic potential via a quartic potential when $\sqrt{\delta z^2} \sim \Delta z_e$, that is, when $\varepsilon_p/k_B T \sim 1$. (d) Charge transfer between the source (S) and drain (D) electrodes when $\varepsilon_p/k_B T \gg 1$. The energy probability distribution of the electrons in the nanotube features two Gaussians.

5.2 Characterization of the device

We reach the strong electron-phonon interaction regime by measuring a device with short nanotube-gate separation in a dilution fridge. We employ the new fabrication process introduced in the Chapter4 (4.2) to reduce the nanotube-gate separation down to $\sim$ 150 nm, while the nanotube is $\sim$ 1.3 μm long (Fig. 5.2(a)). The nanotube is grown by chemical vapour deposition (CVD) in the last fabrication step to minimise surface contamination, and using the 'fast heating' CVD method to avoid the nanotube to collapse onto the gate electrode [33] (see AppendixC).

We measure driven and thermal mechanical vibrations with a high-sensitivity capacitive transduction method using a RLC resonator and

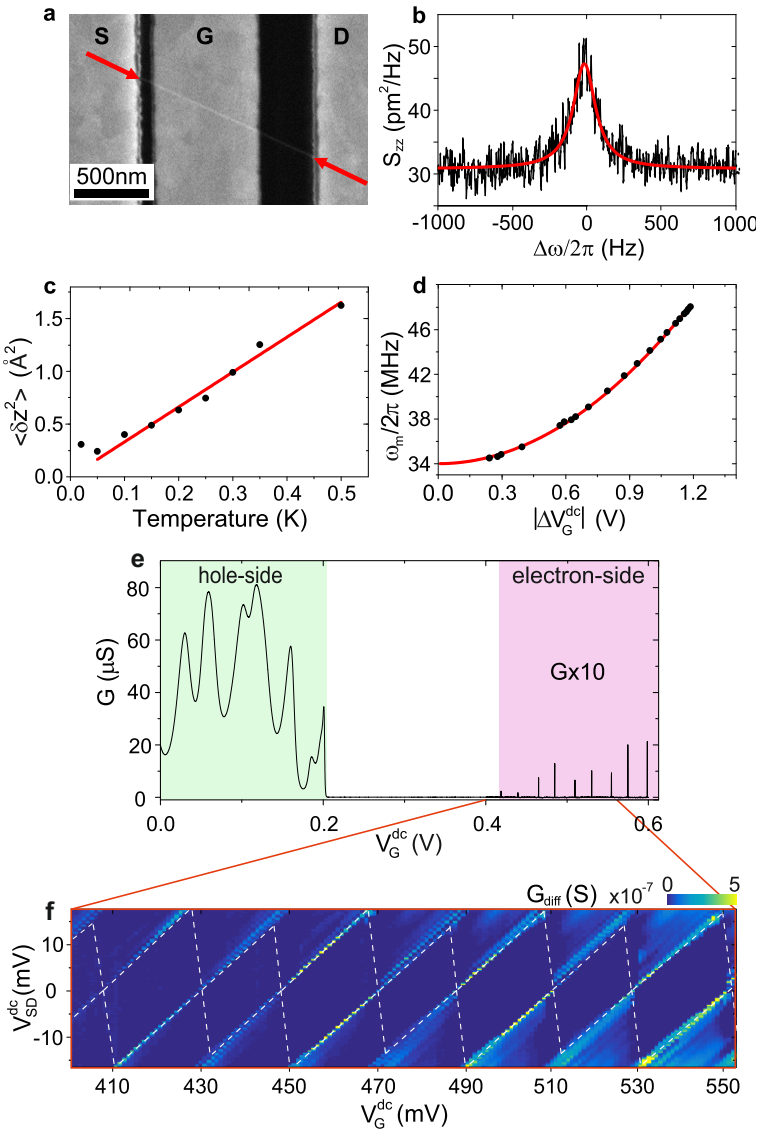

FIGURE 5.2: Characterization of the nanotube electro-mechanical resonator. (a) Scanning electron microscopy image of the device studied in this work. The red arrows indicate the clamping points of the suspended nanotube. (b) Spectrum of the displacement noise of the fundamental eigenmode at base temperature in the hole-side regime when applying V_G^{dc}=-0.07 V. The red line is a Lorentzian fit. (c) Variance of the displacement as a function of cryostat temperature at V_G^{dc}=-0.07 V. (d) Gate voltage dependence of the resonance frequency. The offset voltage $V_{off} = 0.204$ V due to the nanotube-gate work function difference is subtracted from the applied V_G^{dc} value. (e) The gate voltage dependence of the conductance measured at base temperature. The gap region with $G \simeq 0$ S separates the hole-side region from the electron-side region. (f) Differential conductance measured as a function of the source-drain voltage V_{SD}^{dc} and the gate voltage V_G^{dc} at base temperature. The dashed lines indicate the Coulomb diamonds where the current is suppressed.

a HEMT amplifier cooled at liquid-helium temperature [33, 43]. Setting V_G^{dc} in the hole-side regime where the electron-phonon interaction is weak [32], the resonance line-width of the noise of the fundamental mode is narrow, $\Gamma_m^{width} = 2\pi \times 190$ Hz (Fig.5.2(b)). The temperature dependence of the variance of the displacement shows that the mechanical mode temperature saturates at about 100 mK (Fig.5.2(c)), probably because of the noise generated by the HEMT amplifier. The resonance frequency is highly tunable when sweeping V_G^{dc} due to the strong electrostatic coupling between the nanotube and the gate (Fig.5.2(d)). Similarly to what showed in the previous chapter and using Fig.5.2(c and d), we estimate that the effective mass is $m \simeq 8.9$ ag and the spring constant is $k = m\omega_m^2 \simeq 4 - 7 \cdot 10^{-4}$ N/m depending on the gate voltage.

In Fig.5.2(e) we show the gate voltage dependence of the conductance. The measurement is typical of ultraclean, small-gap semiconductor nanotubes [32]. For large positive V_G^{dc} values, $p-n$ junctions are formed near the metal electrodes, forming a SET island along the suspended nanotube. For gate voltage values below $V_G^{dc} \approx 0.2$ V, the nanotube is p-doped along the whole tube, resulting in a larger conductance. The charge stability diagram measurement in the electron-side regime further points to strong electrostatic coupling, since the lever arm of the Coulomb diamonds reaches 0.78 (Fig.5.2(f)). The charge stability diagram indicates even-odd filling upon sweeping V_G^{dc}. We quantify the charging energy $E_C \simeq 14$ meV and the level spacing $\Delta E \approx 2$ meV. The estimated level spacing is consistent with what is expected for a ~ 1.3 μm long nanotube [147]. All the data shown in this chapter are in the regime $k_B T \ll \Delta E, E_C$. The charge stability diagram allows us to quantify the capacitance between the nanotube island and the three electrodes $C_S \simeq 1.2$ aF, $C_D \simeq 1.2$ aF, and $C_G \simeq 9.1$ aF. The large capacitive coupling between the nanotube and the gate electrode $C_G \gg C_S, C_D$ is achieved thanks to the short separation between the nanotube and the gate electrode.

To conclude this section we want to come back to the temperature of phonons and electrons. We attribute the saturation shown in Fig.5.2(c) to the voltage noise produced by the HEMT amplifier. The device is connected to the HEMT amplifier using a semi-rigid coaxial cable with the RLC resonator as the sole filter. We try different connection cables and filter configurations to minimise the current noise floor of the circuit, which is essential to resolve thermal vibrations with a reasonable signal to noise ratio. The electron temperature can be determined by the full width ΔV_G^{SET} at half maximum of the SET conductance peak. Indeed, our model shows that ΔV_G^{SET} scales linearly with temperature to a good approximation, independent of the electron-phonon interaction strength (see Fig.5.5(b) in the next section). Our

measurements at the first Coulomb blockade peak show that the electron temperature saturates at about ≈ 110 mK. Lower electron temperature has been reached with similar electrical circuits using devices in the quantum Hall regime, but such devices are less sensitive to electromagnetic fluctuations [118, 119, 148, 149]. To simplify the analysis of our measurements, we assume that phonons and electrons have the same temperature, i.e. 100 mK, at the base temperature of the cryostat.

5.3 Measurement of polaron effects

We now probe the nature of the polaron state. We set V_G^{dc} in the region of a conductance peak where the system fluctuates between the N and $N+1$ states at high rate (Fig.5.3(a)). Concomitantly, the resonance frequency gets reduced by a large amount, up to 25% (Fig.5.3(b)), which is at least one order of magnitude larger than the values reported in previous works [7–9, 12, 15, 42–44, 145, 146]. Examples of the spectrum of driven vibrations are shown in Fig.5.4(a,b). These are two of the spectra used to quantify the resonance frequency in Fig.5.3(b). The resonance cannot be described by a Lorentzian, as expected for driven spectrum measurements with the mixing technique [38].

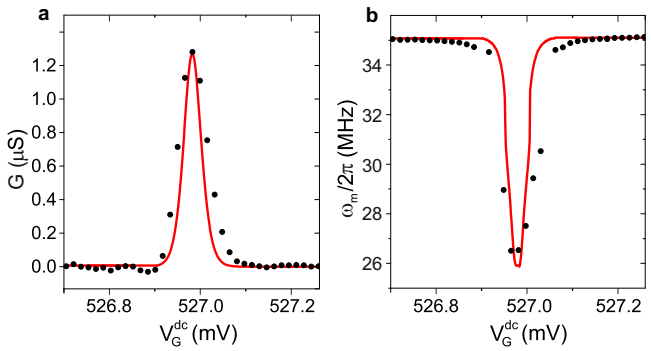

FIGURE 5.3: Electrical and mechanical measurements of polarons at one conductance peak (I). (a,b) Gate voltage dependence of the conductance and the mechanical resonance frequency at base temperature. The red lines are the results of the polaron model estimated with the effective temperature set at 100 mK (for the model, see AppendixB(B.1)).

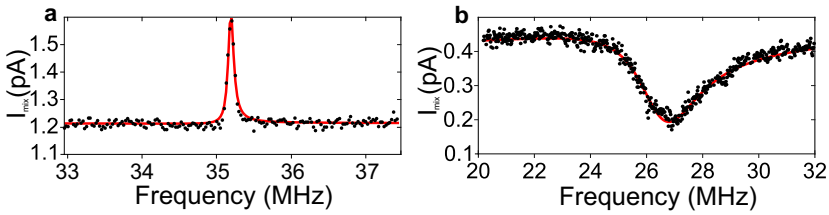

FIGURE 5.4: Spectra of driven vibrations. (a,b) Response of driven vibrations to the drive frequency using the mixing technique at base temperature. The spectra are recorded with V_G^{dc} set at 527.2 mV and 526.98 mV. The red lines correspond to fits expected with the mixing technique [38]

Figure5.5(a) shows that the temperature dependence of the peak conductance deviates significantly from the $1/T$ behaviour (gray dashed line) expected in the regime when the electron-phonon interaction is negligible, and when the temperature is lower than the level spacing ΔE and the charging energy E_C (see AppendixB(B.1)). The measured conductance at 100 mK is about half the value expected in this non-interacting regime. We compare the data to a model treating the electron-phonon interaction non-perturbatively exploiting the time scale separation $\Gamma_e \gg \omega_m$ in the incoherent tunnelling regime $\hbar\Gamma_e \ll k_B T$. The effect of the fluctuating force induced by the electrons transmitted through the nanotube is described by a Fokker-Planck equation that is solved numerically. The agreement between measurements and theory is satisfactory (Figs.5.5(a-d)), especially when considering that only two free parameters are used. We obtain that these two parameters are $\varepsilon_p = 31$ μeV and $\Gamma_e = 2\pi \times 260$ MHz. This is consistent with $\varepsilon_p = F_e^2/k = 33$ μeV estimated from the independent measurements of k and

$$F_e = C'_G \Delta V_G^{dc} \frac{E_C}{e}, \tag{5.1}$$

where $C'_G \simeq 1.1$ x 10^{-11} F/m is the derivative of the nanotube-gate capacitance with respect to z, ΔV_G^{dc} is the gate voltage applied with respect to the offset due to the nanotube-gate work function difference, and e is the charge of an electron.

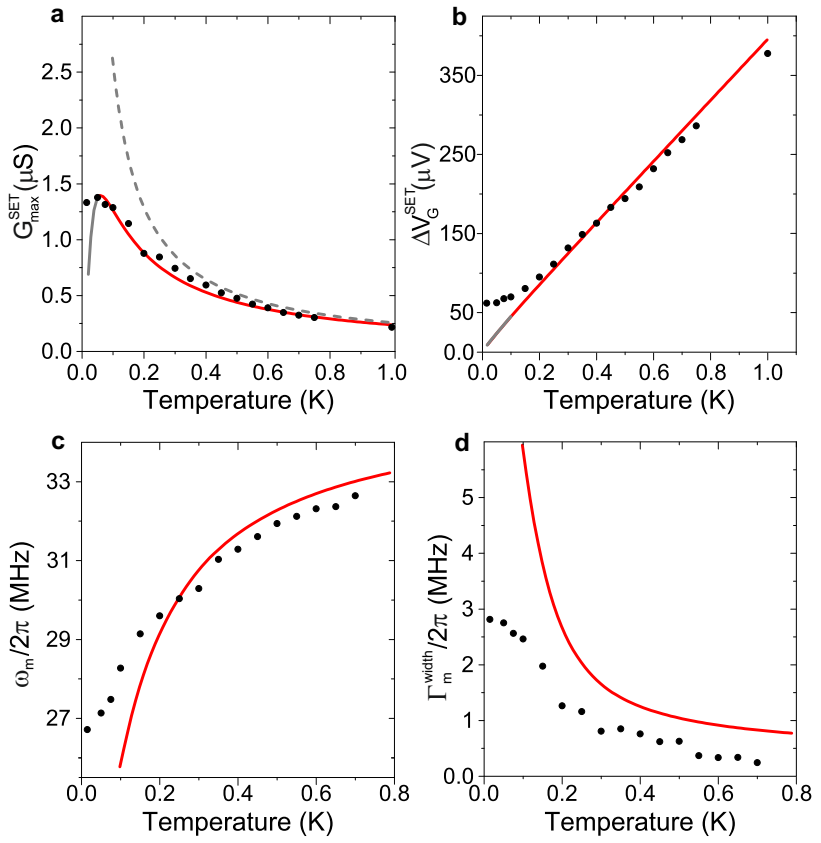

FIGURE 5.5: Electrical and mechanical measurements of polarons at one conductance peak (II). (a-d) Temperature dependence of the peak conductance, the full width at half maximum of the conductance peak, the mechanical resonance frequency, and the mechanical resonance line-width. The red and grey lines are the results of the theoretical model above and below 100 mK, respectively. The grey dashed line is the prediction of the non-interacting regime.

The electron-phonon interaction is tunable by electrostatic means. Figures 5.6(a-f) show the polaron properties at two other conductance peaks. The extracted polaronic energy significantly varies when changing V_G^{dc} (Fig.5.6(g)). The tunability of the electron-phonon interaction is limited by the gate voltage range over which polarons states emerge, that is, when the gate dependent electron rate satisfies $\varepsilon_p \geq \hbar\Gamma_e \geq \hbar\omega_m$ [132].

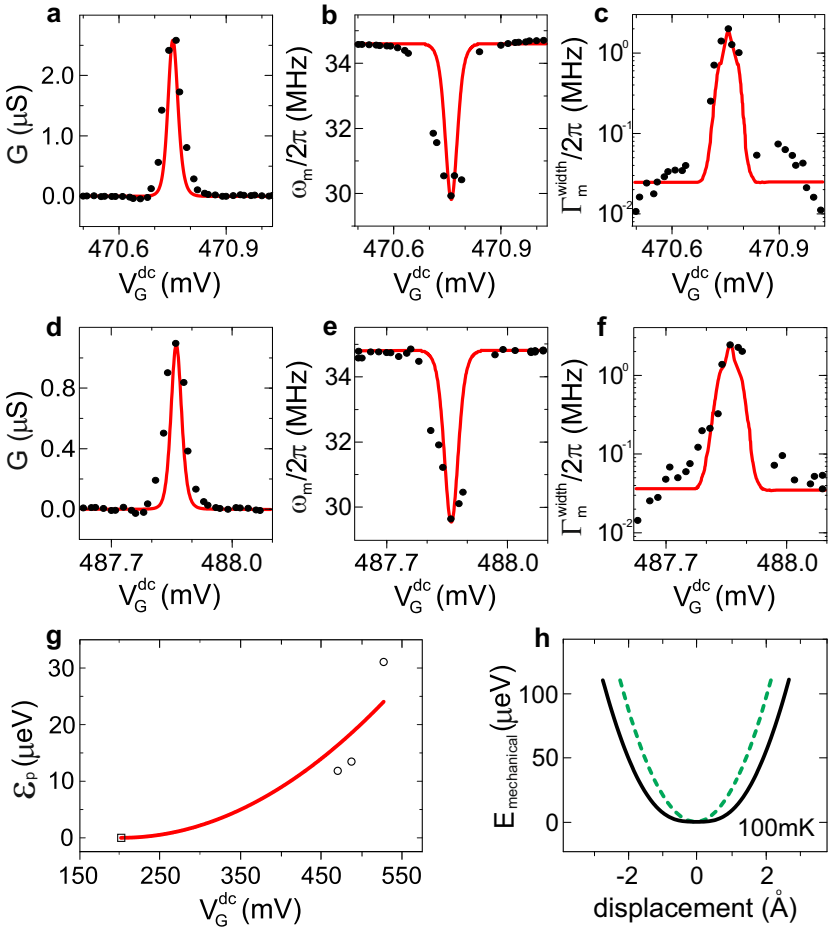

FIGURE 5.6: Electrical and mechanical measurements of polarons at two other conductance peaks. (a-c) Gate voltage dependence of the conductance, the mechanical resonance frequency, and the mechanical resonance line-width at base temperature. The red lines are the results of the polaron model estimated with the effective temperature set at 100 mK. (d-f) Same as a-c but at another gate voltage. (g) Polaron energy as a function of gate voltage (circles). The squared symbol corresponds to zero polaron energy at the nanotube-gate work function offset. The red line is a parabolic fit expected from $\varepsilon_p = F_e^2/k$ and Eq. 5.1. (h) Restoring potential $E_{\text{mechanical}}(z)$ of mechanical vibrations at 100 mK (black line), estimated from the data in Fig.5.5 and 5.3. For comparison, the parabolic potential of the resonator in the non-interaction regime is shown (green dashed line).

The weak interaction regime can be reached by increasing the gate voltage, so that $\hbar\Gamma_e \gg \varepsilon_p$ [132]. The gate voltage controls Γ_e, which is given by the transmission through the $p-n$ junctions formed near the two metal electrodes. By increasing the gate voltage to $V_G^{dc} \simeq$

761 mV with the cryostat set at base temperature, the conductance peak broadens (see Fig.5.7(a)), indicating that the electronic tunneling rate increases to $\Gamma_e \simeq 2\pi \times 75$ GHz. The suppression of the resonance frequency associated to the conductance peak is modest (see Fig.5.7(b)), as measured previously in the weak electron-phonon interaction regime [5–9, 12, 15, 42–44, 97, 145, 146, 150–153].

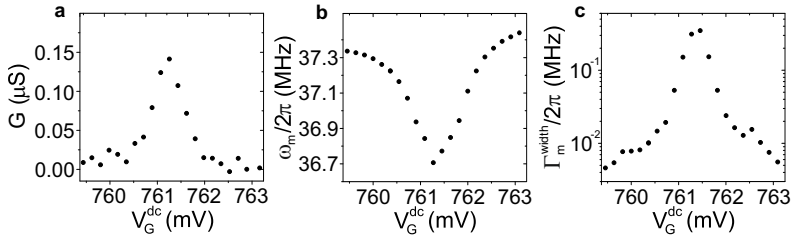

FIGURE 5.7: Electrical and mechanical measurements in the weak electron-phonon interaction regime. (a-c) Gate voltage dependence of the conductance, the mechanical resonance frequency, and the mechanical resonance line-width at base temperature.

Polarons are in the strong interaction regime with $\varepsilon_p/k_BT \simeq 3.6$ at 100 mK in Fig.5.3. The corresponding restoring potential of mechanical vibrations deviates strongly from a harmonic potential (Fig. 5.6(h)), whereas the phonon population is only ≃78 quanta. The quartic potential contributes to the total energy of the resonator by a sizeable amount, 34% at 100 mK. We cannot reach the nonlinear Duffing regime in the response of driven vibrations because of the low quality factor and the weak gate voltage modulation amplitude that we apply; this amplitude has to remain small compared to the width in V_{dc}^G of the conductance peak. This strong nonlinearity generates dephasing of mechanical vibrations, since the curvature of the potential changes with the displacement of thermal vibrations. Our model shows that dephasing contributes by 35% to the mechanical resonance line-width $\Gamma_m^{width} \simeq 2\pi \times 2.4$ MHz in Fig.5.6(f). Dephasing rapidly decreases to zero when lowering ε_p/k_BT (see AppendixB(B.1)). The remaining contribution to the mechanical line-width comes from the energy decay created by the out-of-phase force of the electron dynamics. All the other sources of mechanical dissipation are negligible, since Γ_m^{width} in Fig.5.6(f) is four orders of magnitude larger than that measured in the hole-side regime (Fig.5.2(b)).

Another interesting figure-of-merit of the device is the coupling strength between the mechanical vibrations and the two-level system associated to the N and $N+1$ electron states. It sets the device deep in the ultra-strong coupling regime, since the coupling strength per phonon $g_0 = F_e z_{zp}/\hbar = 2\pi \times 348$ MHz is much higher than $\omega_m = 2\pi \times 35.1$ MHz in Fig.5.3; the zero-point motion is $z_{zp} = 5.2$ pm.

This coupling strength is also larger than the electron rate $\Gamma_e = 2\pi \times$ 260 MHz. The ratio pair g_0/ω_m and g_0/Γ_e compare favourably with the best values reported thus far with electro- and optomechanical systems [154–156].

The physics of the polarons described here is somewhat connected to the Frank-Condon blockade [157, 158] and the excitations of phonon modes [159, 160] in SET devices, where the electron-phonon interaction also modifies the electrical conductance. However, the frequency of the phonon modes in such devices is comparatively much higher, so that their dynamics and their spectra cannot be measured. The decay time of these phonon modes is also extremely short, so that they cannot be manipulated electrically. Finally, the tunability of the electron-phonon interaction has not been demonstrated in these devices.

5.4 Conclusions and outlook

Tunable polarons with strong mechanical nonlinear properties hold promise for a whole series of new electromechanics experiments. Further increasing the interaction strength ε_p/k_BT may enable the demonstration of polaron-blockade, where the conductance is suppressed to zero [132–134]. Moreover, transport measurements in this regime is expected to reveal giant low-frequency electron noise, which arises from the fluctuations of the system between the two minima of the double well potential [132], as observed in phase transitions of systems when the potential is tuned from the single-well to the double-well configurations. In addition, the strong nonlinearity of mechanical vibrations could be used to produce mechanical qubits [161]. This might be achieved by operating the device at $\varepsilon_p \sim k_BT$ when the potential with one minimum is nearly quartic. The mechanical levels are then unequally spaced in energy, similar to what happens in superconducting qubits. An interesting approach to improve the mechanical line-width is to use the second mechanical mode coupled to a double quantum dot formed along the suspended nanotube [42, 43], where a large coupling could be achieved with narrow mechanical line-width [162]. Mechanical qubits might be formed when $k_BT < \hbar\omega_m$ by e.g. cooling a 300–600 nm long nanotube at 10 mK with a cryostat.

Chapter 6

Conclusions

6.1 Summary

In this dissertation, we studied properties of carbon nanotube electromechanical resonators at very low temperature. At dilution temperatures, this class of devices showed their vast capabilities, both in terms of force sensitivity, but also as a very promising platform to investigate ultra-strong coupling related effects.

In Chapter 4, we first presented the implementation of a low noise detection scheme, which consists in a RLC resonator combined with a low temperature HEMT amplifier. It allowed us to lower the setup current noise floor down to 38 fA/$\sqrt{\text{Hz}}$. Moreover, the improved fabrication technique utilized here, helped us to ulteriorly decrease the separation between the carbon nanotube resonator and the underlying metal gate. This increased their coupling while keeping an ultra-high level of cleanness. By employing this new read-out setup, we examined the noise performances of a CNT resonator. We reported on force sensitivity of 4.3 zN/$\sqrt{\text{Hz}}$ and displacement sensitivity of 0.5 pm/$\sqrt{\text{Hz}}$, solely limited by Joule heating. We benchmarked the performance of our device with other micro- and nano-resonators, resulting in a favourable comparison with them, and further confirming the extremely high sensitivity of carbon nanotube resonators.

In Chapter 5, we investigated the electron-phonon coupling in a carbon nanotube based vibrating quantum dot. Measuring such device at dilution temperatures, we demonstrated that our system is in the ultra-strong coupling regime, where the coupling strength is one order of magnitude larger than the resonance frequency. More importantly, for the first time in a mechanical resonator close to the quantum regime, this interaction effectively creates a highly nonlinear potential for the phonon mode. In this system, mechanical vibrations and electrons are so strongly coupled that they need to be treated as a single entity: a quasi-particle called polaron. We showed that the formation of polarons in the device has a strong impact, both on the electron

transport and mechanical properties. For the first time in this kind of devices, we measured a suppression of the electrical conductance by up to about half its value, and the resonance frequency decreased by 25%, a softening at least one order of magnitude bigger than all previously reported experiments. Furthermore, we showed that polaron states can be significantly tuned by electrostatic means.

6.2 Outlook

The work presented in this thesis offers possibilities for studying a whole series of new experiments employing carbon nanotube resonators.

The reported high force sensitivity in Chapter 4 is an important step towards detecting individual nuclear spins with nuclear magnetic resonance measurements [28, 29]. The experiment can be carried out producing a gradient of magnetic field with a current biased through the gate electrode [127], which will generate and exert a coherent force on the nanotube resonator. Magnetic resonance force microscopy (MRFM) measurements, to image the location of individual nuclear spins adsorbed along the nanotube, can be done by periodically applying radio-frequency pulses though the current-carrying electrode [129]. An even more promising approach to detect nuclear spins with a nanotube resonator is to couple them resonantly with mechanical vibrations [163]. Matching the mechanical resonance frequency with the Larmor frequency of the spins by external magnetic field tuning, and driving at resonance the oscillator in the presence of a gradient of magnetic field, would create a resonant coupling between vibrations and spins. Due to the frequency matching condition, this protocol is particularly suitable for nanotube resonators since both frequencies are typically of the order of tens of MHz. Moreover, generating the gradient of the magnetic field with a ferromagnetic nanoparticle, would allow us to perform this experiment with no need for constant or oscillating currents, which would be detrimental to nanotube noise performances.

If the interaction strength ε_p/k_BT presented in Chapter 5 will be further increased, the system could go through a transition towards a mechanical bistability. That may enable the demonstration of polaron-blockade, where the conductance is suppressed to zero [132–135]. In addition as we already anticipated, the strong nonlinearity of mechanical vibrations could be used to engineer mechanical qubits [161]. This might be achieved by tuning the coupling strength such that $\varepsilon_p \sim k_BT$ when the potential with one minimum is nearly quartic. The mechanical levels are then unequally spaced in energy, similar to what happens in superconducting qubits. Cooling a 300–600 nm long nanotube

at 10 mK with a cryostat, mechanical qubits might be formed in their quantum ground state, when $k_B T < \hbar\omega_m$. In a long-term vision, this scheme could be advantageous also because mechanical qubits could be coupled to many other quantum degrees of freedom, such as spins, photons, and atoms.

Appendix A

Additional information on Chapter 4

In this section we describe the read-out line, presenting the implementation of the HEMT amplifier together with the RLC resonator.
We present the modelling of the system and the noise characterization, which allows us to quantify the noise generated by all the different sources.

A.1 Read-out line characterization: low temperature HEMT and RLC resonator

The high electron mobility transistor (HEMT) acts as the active element into the amplifier circuit [164]. This transistor is based on a two-dimensional electron gas formed at the interface of a AlGaAs/GaAs heterostructure obtained by molecular beam epitaxy [121] and provided by our collaborators at the Center de Nanosciences et de Nanotechnologies (CNRS), Univ. Paris-Sud.
In Fig.A.1 the scheme of the HEMT, together with all the passive elements needed to build the amplifier circuit, is illustrated. All the components are soldered onto a oxygen-free copper made PCB, which is thermally anchored at the 3K plate of the cryostat.
Capacitors and resistors placed around the HEMT help to filter high frequency noise. They also fix and stabilize the voltages used to polarize the transistor. The HEMT is polarized at V_{dd} and V_s which are further filtered with some π-filters soldered onto the PCB.
The signal from the nanotube device, filtered by the RLC resonator at the mixing chamber, enters into the amplifier circuit through the gate of the HEMT and gets amplified by a factor G_{HEMT}, then is collected at the drain of the transistor.
The gain G_{HEMT} has a strong dependency on the operating point of the transistor.

We chose a low noise operating point with a source drain voltage difference of 100mV and a current I_{sd} =1mA at 3.2K. Accordingly, the polarization voltages are V_{dd} =326mV and V_s =77mV.

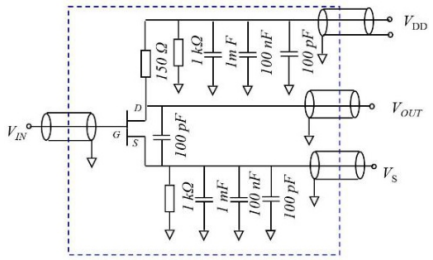

FIGURE A.1: Schematic of the circuit of the HEMT amplifier. Courtesy of Quan Dong and Yong Jin, Centre de Nanosciences et de Nanotechnologies, CNRS, Univ. Paris-Sud.

The RLC resonator is fabricated soldering on a separated PCB the surface mount components, then physically attached at the mixing chamber of the cryostat, just after the carbon nanotube device.
A resistor of 10kOhm and an inductor of 66μH provide the R and L of the resonator. We don't add any capacitor onto the PCB since the capacitance offered by the RF-lines of the fridge is already sufficient to set an high enough resonance frequency for the RLC tank.
In Fig.A.2 is shown the schematic of the RLC resonator and HEMT amplifier with all the noise sources contributing.
The total impedance Z_{tot} of the system is not only due to the resistance R of the RLC, but also to the input impedance of the HEMT Z_{HEMT} and, since they are in parallel, we can write $\frac{1}{Z_{tot}} = \frac{1}{R} + \frac{1}{Z_{HEMT}}$.
The input impedance of the HEMT is due to the Miller capacitance of the amplifier, which is related to the capacitance between the input and the output of the transistor. For the impedance of the RLC, we only consider R and not the resistance *r* of the inductor because at low temperature it is around 1 Ohm.

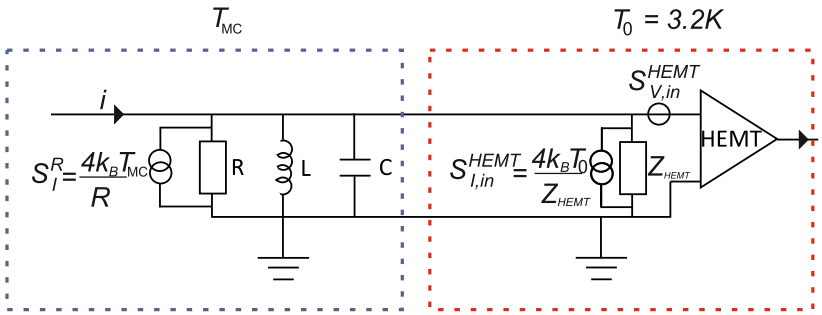

FIGURE A.2: Schematic of the read-out line with all the different noise sources. The thermal noise is due to the the parallel of the RLC impedance and the one of the HEMT. The HEMT contributes also with its input current noise and input voltage noise to the total noise.

In the MHz range $r \ll L\Omega$, so that the power spectral density (PSD) of the thermal noise of the system reads [164]:

$$S_V^{JN} = \frac{G_{HEMT}^2 4k_B T Re(Z_{tot})}{1 + 4(Z_{tot}C)^2 4\pi^2 (f - f_{RLC})^2} \tag{A.1}$$

with C the capacitance of the RLC tank. We measure the PSD and then we fit it with the following equation:

$$S_V^{JN} = \frac{2A}{\pi \Delta f_{RLC}} \frac{1}{1 + 4(f - f_{RLC})^2 / \Delta f_0^2} \tag{A.2}$$

where A is the area under the Lorentzian and Δf_{RLC} its linewidth. A typical Lorentzian response is shown in FigA.3(a), where the RLC tank temperature is 4K. From this fit, we obtain the RLC parameters given the Chapter 4(4.3).
Using the nominal value of L and the value of f_{RLC} =1.73MHz from the fit, we get $C = \frac{1}{4\pi^2 f_{RLC}^2 L}$ =129pF. Using the fact that the quality factor of the RLC is $Q = Re(Z_{tot})\sqrt{\frac{C}{L}}$ and knowing Δf_{RLC} =156kHz from the fit we obtain the real part of the total impedance $Re(Z_{tot})$ =7.79kΩ. Finally, the Lorentzian has an offset from the zero noise level that comes from the input voltage noise of the HEMT $\sqrt{S_{V,in}^{HEMT}}$ =0.125nV/$\sqrt{\text{Hz}}$, which we also obtain from the fitting.
The Johnson-Nyquist noise is given by $4k_BTRe(Z_{tot}^2)/R$. From the temperature dependence of the normalized area under the Lorentzian curve of the thermal noise, the gain of the HEMT G_{HEMT} and the input current noise of the HEMT $\sqrt{S_{I,in}^{HEMT}}$ can be extracted. In Fig.A.3(b)

this dependence is shown[1].
The fact that the whole system is a parallel of the HEMT amplifier and RLC resonator allow us to perform a linear fit of the experimental data with the following equation:

$$\frac{2A}{\pi\Delta f_{RLC}} = G^2_{HEMT} 4k_B \frac{Re(Z^2_{tot})}{R} T + S^{HEMT}_{I,in} Re(Z^2_{tot}) G^2_{HEMT} \quad \text{(A.3)}$$

Finally, we obtain the gain of the HEMT amplifier G_{HEMT} =6.4 and the input current noise of the HEMT $\sqrt{S^{HEMT}_{I,in}}$ =21.6fA/$\sqrt{\text{Hz}}$.

To conclude, we point out that the total voltage noise measured at the output of the HEMT (as shown in Fig.A.3(a)) is summarized in the following expression:

$$S^{tot}_V = G^2_{HEMT}[4k_B T Re(Z^2_{tot})/R + S^{HEMT}_{I,in} Re(Z^2_{tot}) + S^{HEMT}_{V,in}] \quad \text{(A.4)}$$

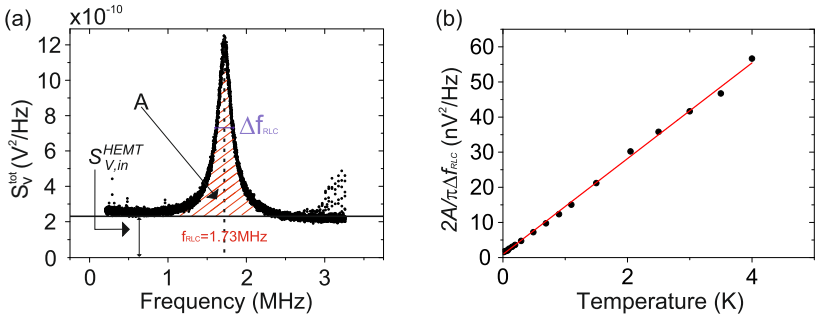

FIGURE A.3: The noise of the read-out line. (a) The total voltage noise of the setup meausured after the amplification through the HEMT with the RLC at 4K. The response has a typical Lorentzian shape and the offset is due to the input voltage noise of the HEMT. A is the area under the Lorentzian curve without the contribution of the input voltage noise of the HEMT. (b) The normalized area under the Lorentzian $2A/\pi\Delta f_{RLC}$ as a function of the temperature. The red trace is a fit of the point obtained with the Lorentzian fit of the measured voltage noise.

[1]We want to note that the gain of the HEMT is not affected by the change of the temperature of the mixing chamber, since it is thermally anchored at the 3K stage

Appendix B

Additional information on Chapter 5

Here, we present the model (fully developed by our collaborator Fabio Pistolesi) used to describe the system in the strong coupling regime.

B.1 The model

B.1.1 Assumptions and model describing the electromechanical device

We discuss in this Appendix the model to describe the electronic transport and the mechanical dynamics in the regime $\hbar\omega_m \ll \hbar\Gamma_e \ll k_BT \ll \Delta E, E_C$, where $\omega_m/2\pi$ is the (bare) mechanical frequency, Γ_e the typical electronic tunnelling rate, E_C the Coulomb charging energy of the quantum dot, ΔE the electronic energy spacing, and T the temperature. In the limit $\hbar\omega_m \ll \hbar\Gamma_e \ll k_BT$ the oscillator is slower than the hopping electrons and is classical. The oscillator displacement, z, will then enter the electronic Hamiltonian as a classical parameter. One obtains the standard description of incoherent sequential transport in presence of spin degeneracy [165, 166] with tunnelling rates ($\Gamma_\alpha^\pm$) to add/remove one electron to/from the dot from/to the lead α (where α takes the values S/D for source/drain lead). The rates read $\Gamma_\alpha^+ = \Gamma_\alpha f_\alpha$ and $\Gamma_\alpha^- = \Gamma_\alpha(1-f_\alpha)$, with Γ_α the maximum tunneling rate and $f_\alpha = f_F(E_\alpha - F_e z)$. Here $f_F(\epsilon) = 1/(e^{\epsilon/k_BT}+1)$ is the Fermi function, F_e is the variation of the force acting on the nanotube when one electron is added, and E_α is the electronic energy variation induced by the capacitive coupling to the electrodes. In our setup they read: $E_S = -e[C_G V_G^e + (C_D + C_G)V_{SD}^{dc}]/C_\Sigma$ and $E_D = -e[C_G V_G^e - C_S V_{SD}^{dc}]/C_\Sigma$, where C_S, C_D, C_G are the source, drain, and gate capacitances, V_{SD}^{dc} is the source-drain bias voltage, V_G^e is the voltage difference between the gate and the drain electrodes measured from the charge degeneracy point for vanishing V_{SD}^{dc} and z. In the following we use the notation $\epsilon_0 = -eC_G V_G^e/C_\Sigma$.

B.1.2 Vanishing electron-phonon coupling ($F_e = 0$)

We assume that only three electronic states participate to transport. We label these by 0, $\sigma = \uparrow, \downarrow$. They correspond to the states with N electrons (0) and $N+1$ electrons with spin projection σ ($\uparrow$,$\downarrow$). The master equation for the occupation probabilities of these states read [165]

$$\dot{P}_0 = -2\Gamma^+ P_0 + \Gamma^- \sum_\sigma P_\sigma \tag{B.1}$$

$$\dot{P}_\sigma = -\Gamma^- P_\sigma + \Gamma^+ P_0 \tag{B.2}$$

where $\Gamma^\pm = \Gamma_S^\pm + \Gamma_D^\pm$. By symmetry $P_\uparrow = P_\downarrow = P_\sigma$ and we obtain $P_\sigma = \Gamma^+/(\Gamma^- + 2\Gamma^+)$. The stationary current then reads

$$I = \frac{2e\Gamma_S\Gamma_D(f_S - f_D)}{\Gamma_S + \Gamma_D + \Gamma_S f_S + \Gamma_D f_D}, \tag{B.3}$$

with the conductance for $V_{SD}^{dc} \to 0$:

$$G = G_T h(\epsilon_0/k_B T), \tag{B.4}$$

where $G_T = (e^2/k_B T)\Gamma_S\Gamma_D/(\Gamma_S + \Gamma_D)$ and $h(y) = e^y/(e^y+1)(e^y+2)$ gives the shape of the conductance as a function of the gate voltage. The function h has a maximum value of $3 - 2\sqrt{2}$ at $y = (\ln 2)/2$, leading to a full-width half-height of the conductance peak of $3.56 k_B T$. Expression B.4 gives the standard $1/T$ dependence for the conductance maximum that is expected to hold for $\Gamma_\alpha \ll k_B T \ll E_C, \Delta E$, assuming that the energy dependence of the tunnelling rates is negligible. In normal conditions it allows thus to extract the value of $\Gamma_S\Gamma_D/(\Gamma_S+\Gamma_D)$ from the fit of the $1/T$ dependence of the conductance maximum. This is no longer the case in the strong electro-phonon interaction regime.

B.1.3 Equilibrium description of the oscillator

We begin the discussion of the interacting case by considering the equilibrium state ($V_{SD}^{dc} = 0$). In this case we can obtain an exact description of the mechanical oscillator statistical properties. The classical Hamiltonian is

$$H(z, p_z, n) = \frac{p_z^2}{2m} + \frac{k}{2}z^2 + (\epsilon_0 - F_e z)n \tag{B.5}$$

where p_z is the momentum of the oscillator and n is the electronic occupation. n takes the values 0 or 1; the latter is realized with double multiplicity. Using $n^2 = n$ we can re-write the Hamiltonian as

$$H(z, p_z, n) = \frac{p_z^2}{2m} + \frac{k}{2}(z - nF_e)^2 + (\epsilon_0 - \varepsilon_p/2)n \tag{B.6}$$

where we introduced the polaronic energy $\varepsilon_p = F_e^2/k$. The partition function $\mathcal{Z} = \sum_{n=0,1,1} \int dp_z \int dz e^{\frac{-H(z,p_z,n)}{k_B T}}$ can be readily evaluated giving

$$\mathcal{Z} = \frac{2\pi\omega_m}{k_B T}\left[1 + 2e^{-(\epsilon_0 - \varepsilon_p/2)/k_B T}\right]. \tag{B.7}$$

The probability of finding the oscillator at position z traced over the dot states and the momentum is $P_{eq}(z) = \sum_n \int dp_z e^{-H(z,p_z,n)/k_B T}/\mathcal{Z}$. It reads

$$P_{eq}(z) = \mathcal{G}(z)W_- + \mathcal{G}(z - F_e/k)W_+, \tag{B.8}$$

with $\mathcal{G}(z) = e^{-kz^2/2k_B T}(k/2\pi k_B T)^{1/2}$ and

$$W_\pm = 1/(1 + e^{\pm(\epsilon_0 - /2 - k_B T \ln 2)/k_B T}), \tag{B.9}$$

the weights for the two occupation states, 1 and 0, respectively. $P_{eq}(z)$ is thus given by the sum of two gaussians of width $\sim \sqrt{k_B T/k}$ centered at the equilibrium position of the oscillator $z = 0$ for $n = 0$ or $z = F_e/k$ for $n = 1$ (See Fig.5.1(c)). The square of the ratio of the gaussians width over the distance of the two equilibrium positions gives $\varepsilon_p/k_B T$, which thus constitutes the crucial dimensionless coupling constant of the problem. The probability $P_{eq}(z)$ describes the interplay of the thermal fluctuations with the electron-phonon interaction. For $\varepsilon_p/k_B T \ll 1$ one finds that the oscillator features the usual gaussian fluctuations around the equilibrium position. On the opposite regime for $\varepsilon_p/k_B T \gg 1$ one has instead two well separated gaussians distributions. For $\epsilon_0 - \varepsilon_p/2 - k_B T \ln 2 = 0$ the weights are equal ($W_+ = W_-$) and the oscillator spends the same time on the two equilibrium positions. In the limit of $\omega_m \ll \Gamma_e$ the force acting on the oscillator due to the electron charge fluctuations can be averaged for any given value of z: $F(z) = F_e\langle n\rangle(z)$. It makes then sense to define an effective potential $U(z) = -\int^z dz' F(z')$ from this average force, or equivalently, from $P_{eq}(z) = e^{-U(z)/k_B T}\mathcal{N}$ with $\mathcal{N}$ a normalization factor. Using the expression B.8 one obtains:

$$U(z) = -k_B T \ln\left[1 + 2e^{-(\epsilon_0 - F_e z)/k_B T}\right] + \frac{kz^2}{2}. \tag{B.10}$$

This is the potential discussed in the introduction of the Chapter 5 (Fig.5.1(c)). It evolves from a single parabolic well for $\varepsilon_p/k_B T \ll 1$ to a double well in the opposite limit. One can find the position z_e where the maximum and the minimum merge: $U'(z_e) = 0$ and $U''(z_e) = 0$. This leads to $e^{(\epsilon_0 - F_e z_e)/k_B T} = 2F_e/kz_e - 2$ and $kz_e/F_e - (kz_e/F_e)^2 - k_B T/\varepsilon_p = 0$. We thus have $kz_e/F_e = (1 \pm \sqrt{1 - 4k_B T/\varepsilon_p})/2$. This implies that in order to have a bistable behaviour one needs $\varepsilon_p > 4k_B T$. As discussed in the chapter the critical value of ε_p for the bistability

to appear is of the order of $k_B T$, here we derived the numerical coefficient.

From these results one can derive an expression for the zero-bias conductance that reads:

$$G = \int dz P_{\mathrm{eq}}(z) G(z), \tag{B.11}$$

where $G(z)$ is just the non-interacting expression B.4 for the conductance with $\epsilon_0 \to \epsilon_0 - F_e z$ and $P_{\mathrm{eq}}(z)$ is given by B.8. This expression can be evaluated numerically and the result is shown in Fig.B.1 where we plot the peak conductance $G^{\max}$ (thick line) in units of $(2e^2/\varepsilon_p)\Gamma_S\Gamma_D/(\Gamma_S+\Gamma_D)$ as a function of $k_B T/\varepsilon_p$. One observes an exponential suppression for strong coupling and a power law reduction in the weak coupling.

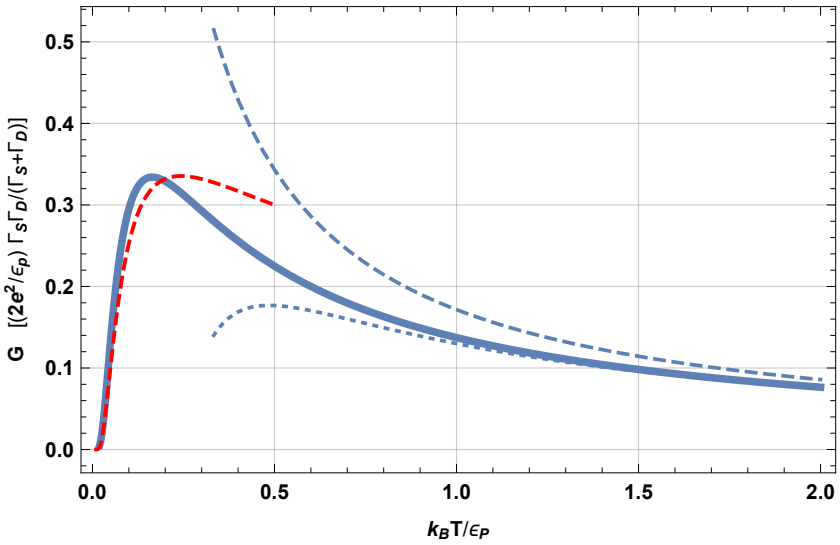

FIGURE B.1: Predicted conductance. Maximum of the conductance as a function of temperature from the numerical integration of B.11 (thick line), non-interacting prediction (dashed blue line), first order correction in the weak coupling limit (dotted blue line), and strong coupling exponential approximation (dashed red line).

B.1.4 Fokker-Planck equation description

In order to describe the system out of equilibrium we begin by deriving a Langevin equation for the oscillator displacement. In the limit $\omega_m \ll \Gamma_\alpha$ for each value of z we can obtain the average force and the correlation function of its fluctuation by calculating the average

$\langle n \rangle(z) = 2P_\sigma(z)$ and the correlation function

$$\langle \delta n(t)\delta n(0)\rangle(z) = 2\frac{\Gamma_+\Gamma_-}{\Gamma_g}e^{-\Gamma_g|t|} \tag{B.12}$$

($\delta n = n - \langle n \rangle$) making use of the master equations (B.1-B.2). Here $\Gamma_g = \Gamma^- + 2\Gamma^+$ and the z dependence comes from the $\epsilon_0 - F_e z$ dependence of the tunnelling rate. The small retardation of the electronic system with respect to variations of z induces a damping term. This term adds up to the intrinsic dissipation rate of the oscillator γ leading to an effective dissipation rate:

$$\gamma_{\rm eff} = \gamma + \frac{2(\Gamma_S + \Gamma_D)\varepsilon_p \omega_m^2}{(\Gamma_g^2+^2)\Gamma_g k_B T}[\Gamma_S f_S(1-f_S) + \Gamma_D f_D(1-f_D)]. \tag{B.13}$$

We thus obtain the Langevin equation:

$$m\ddot{z} = -m\omega_m^2 z - m\gamma_{\rm eff}\dot{z} + 2F_e P_\sigma(z) + \xi(t), \tag{B.14}$$

with $\xi(t)$ the fluctuating force acting on the oscillator. The Fourier transform at frequency ω_m of the force correlation function reads:

$$D \equiv \langle \xi(t)\xi(0)\rangle_\omega = 2k_B T\gamma m + \frac{4F_e^2\Gamma_+\Gamma_-}{\Gamma_g(\omega_m^2 + \Gamma_g^2)}, \tag{B.15}$$

where we included the fluctuation-dissipation white noise contribution due to the bare dissipative term (γ). From the Langevin equation one can derive a Fokker-Planck equation for $P(z, p_z, t)$, the probability to observe a diplacement z and a momentum p_z of the oscillator at time t. We have $\partial_t P = \mathcal{L}P$ with

$$\mathcal{L} = \left[-\frac{p_z}{m}\partial_z - F(z)\partial_{p_z} + \gamma_{\rm eff}\partial_{p_z} + \frac{D(z)}{2}\partial_{p_z}^2\right] \tag{B.16}$$

and $F(z) = 2F_e P_\sigma(z) - kz$. This equation allows to obtain the current and the behaviour of the oscillator also far from equilibrium for $eV_{SD}^{dc} \gg k_B T$. We solved it numerically, by discretization of the variables z and p_z; typically meshes of 100×100 points are sufficient. The operator $\mathcal{L}$ becomes a (sparse) matrix acting on the vector $P(z_i, p_i, t)$, with (z_i, p_i) the points on the mesch. One can then obtain the stationary distribution $P_{\rm st}$ by solving $\mathcal{L}P_{\rm st} = 0$. We also obtain the displacement correlation function: $S_{zz}(t) = \langle \delta z(t)\delta z(0)\rangle$, where $\delta z(t) = z(t) - \langle z \rangle$, and $\langle z \rangle = \int dz dp P_{\rm st}(z, p)$. We can then calculate its Fourier transform as [167]

$$S_{zz}(\omega) = -2{\rm Tr}\left[\hat{Z}\frac{\mathcal{L}}{\omega^2 + \mathcal{L}}\hat{Z}\right]P_{\rm st}, \tag{B.17}$$

where $\hat{Z}$ is the super-operator defined by $\hat{Z}P = \delta z P$. This quantity can be evaluated for each value of ω once the matrices $\hat{Z}$ and $\mathcal{L}$ are known.

Knwowledge of $S_{zz}(\omega)$ gives information on the linear response function to a driving force [132]. In the chapter we uses this quantity to obtain the form of the response function, the frequency at which the response is largest, and its width. In order to have a consistent description we use the numerical solution of the Fokker-Planck equation to obtain the zero bias conductance, the renormalized value ω_{R} for the resonance frequency ω_m, and the full-width half-maximum of the fluctuation spectrum $\Gamma_{\mathrm{m}}^{\mathrm{width}}$.

B.1.5 Fitting procedure

In order to obtain quantitative predictions with the model one only needs the following three dimensionless parameters $\lambda = \{\Gamma_{\mathrm{S}}/\omega_m, \Gamma_{\mathrm{D}}/\omega_m, \varepsilon_{\mathrm{p}}/k_B T\}$, since the bare resonating frequency ω_m is directly measured from the spectrum far from the maximum of conductance, and the temperature is known. In practice, for a given λ we numerically find the maximum of the conductance as a function of the dimensionless $eV_{\mathrm{G}}^{\mathrm{dc}}/\varepsilon_{\mathrm{p}}$. At this value of $V_{\mathrm{G}}^{\mathrm{dc}}$ we then calculate the $S_{zz}(\omega)$ spectrum, and we obtain ω_R and $\Gamma_{\mathrm{m}}^{\mathrm{width}}$. We then perform a fit by minimizing the function

$$\chi^2(\lambda) = \sum_{i=1}^{3} (A_i^{\mathrm{exp}} - A_i(\lambda))^2/(\Delta A_i)^2, \tag{B.18}$$

where A_i are the following quantities $\{G^{\mathrm{max}}, \Gamma_{\mathrm{m}}^{\mathrm{width}}, \omega_R\}$, A_i^{exp} stands for the experimental value, $A_i(\lambda)$ for the model prediction for the given λ, and ΔA_i is an estimate of the experimental incertitude for the quantity A_i. We use $\Delta A_i/A_i = 0.1$, implying the same weight for the three quantities. We perform two fit procedures, one with the three parameters free to vary and a second one with $\Gamma_{\mathrm{S}} = \Gamma_{\mathrm{D}}$. Both procedures result in similar fit quality, so that we choose to use the fit with $\Gamma_{\mathrm{S}} = \Gamma_{\mathrm{D}}$. We then use the numerical solution of the Fokker-Planck equation to obtain the theoretical curves presented in Figs.5.3, 5.5 and 5.6, without any other adjustable parameter. In Fig.B.2 we show how dissipation and the mechanical resonance linewidth evolve as a function of $\varepsilon_{\mathrm{p}}/k_B T$. Dephasing decreases to zero at high temperature.

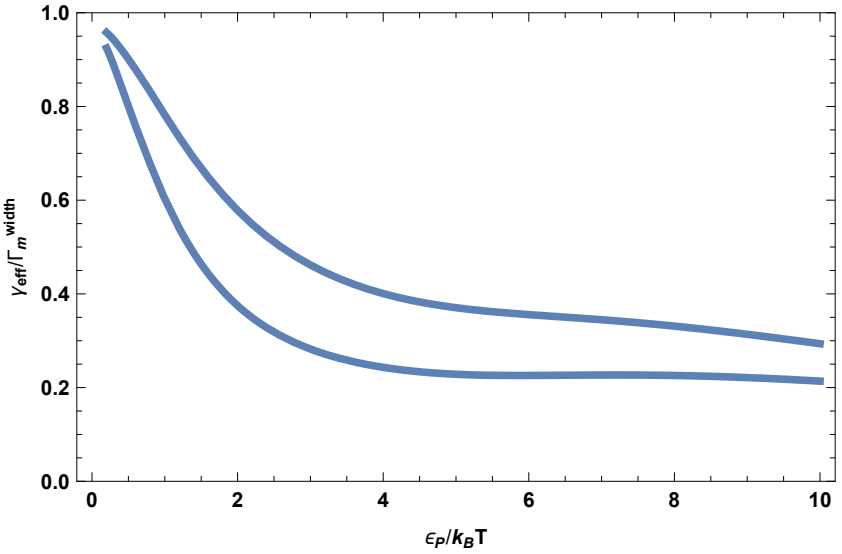

FIGURE B.2: Calculated dissipation and dephasing. The ratio of the effective damping induced by the interaction ($\gamma_{\rm eff}$) to the mechanical resonance linewidth ($\Gamma_{\rm m}^{\rm width}$) is shown as a function of $\varepsilon_{\rm p}/k_{\rm B}T$. The damping is obtained with B.13 and averaged over the stationary distribution $P_{\rm st}(z, p_z)$. The values are calculated at the maximum of the conductance peak for $V_{\rm G}^{\rm dc} \simeq 527$ mV (lower line) and $V_{\rm G}^{\rm dc} \simeq 487$ mV (upper line).

B.2 The single-electron force

In this section we derive the expression 5.1 for $F_{\rm e}$ that appears in the chapter5 (5.3). We want to devote some attention to this calculation because this force accounts for all the effects measured in this work (it is the most relevant term in the Hamiltonian B.5).
As mentioned earlier, the nanotube and the gate electrode are capacitively coupled and then, since the nanotube is vibrating, this capacitance will vary also (the ones respect to source and drain are assumed constant because are parallel to the displacement of the tube).
The electromechanial force F is then given by the variation of the total potential energy of the three capacitors with the displacement:

$$F(z) = -\frac{dU(z)}{dz} \tag{B.19}$$

where z is the direction of the motion perpendicular to the gate plane and $U(z)$ is the electrostatic energy. Let's now define $U(z)$.
We need to use the electric potential of the quantum dot $\phi(z)$ to derive $U(z)$. The electric potential is determined by the total charge Q such that the first charge dQ tunnelling into the dot experiences a potential

$\phi(z, Q = 0)$, the second one $\phi(z, Q = dQ)$, etc... In the limit of large number of electron, we obtain:

$$U(z, Q) = \int_0^Q \phi(z, Q')dQ' \tag{B.20}$$

The charge around the island is opposite to the charge into the island, because of the capacitive coupling. Then we write:

$$Q = -\sum_i Q_i = -\sum_i C_i(V_i - \phi) \tag{B.21}$$

where $i = g, s, d$ which stand for gate, source and drain, C_i is the electrode capacitance and V_i is the electrode potential. We can finally write an expression for the potential as a function of the charge:

$$\phi = \frac{\sum_i C_i V_i + Q}{\sum_i C_i} = \frac{q + Q}{C_{tot}} \tag{B.22}$$

where $q = \sum C_i V_i$ and $C_{tot} = \sum C_i$. Inserting equation B.22 in equation B.20 we get:

$$U(z, Q) = \frac{qQ}{C_{tot}} + \frac{Q^2}{2C_{tot}} \tag{B.23}$$

Minimizing the potential energy in equation B.23, we obtain that the charge at minimum is $Q = -q$. We must now note that so far we considered the limit of continuous charge, but $Q = -N|e|$ is quantized and q (also called in literature control charge) can take fractional values. Therefore, $Q = q$ is not a general case condition.
We have to find an integer number for the charge that minimizes the potential energy as close as possible to q. Typically, $q \approx (N + 1/2)|e|$, where $N \gg 1$, and the only relevant levels for the problem are $Q = -N|e|$ and $Q = -(N + 1)|e|$.
We can compute now the force from equation B.23, using $\partial C_{tot}/\partial z = C'_g$ and $\partial q/\partial z = C'_g V_g$:

$$F(z, Q) = -\frac{\partial U(z, Q)}{\partial z} = -\frac{C'_g}{C_{tot}} Q V_g + \frac{C'_g}{2C_{tot}} \frac{Q + 2q}{C_{tot}} Q \tag{B.24}$$

Considering that only two levels enter the dynamics ($Q_0 = -N|e|$ and $Q_1 = -(N + 1)|e|$), the force can be rewritten as:

$$F(z, Q) = F(z, Q_0) + F_e(z)n \tag{B.25}$$

where $F_e(z)$ is the difference between the force in levels Q_1 and Q_0, with $n = 0$ when the system is in the state Q_0 and $n = 1$ otherwise. Finally, we obtain for $F_e(z)$:

$$F_e(z) = \frac{C'_g}{C_{tot}} e \left[V_g - \frac{2q - (2N+1)e}{C_{tot}} \right] \approx \frac{C'_g}{C_{tot}} e V_g \tag{B.26}$$

where, in the last relation, the strictly equality holds if the dot is at the equilibrium point $q = (n + 1/2)|e|$. We recovered the equation 5.1).
For small displacement of the nanotube, we take for $F_e(z)$ its equilibrium value F_e. Finally, the equation of the potential energy recast (as in B.5):

$$U(z) \approx -F_e z n. \tag{B.27}$$

Appendix C

Device fabrication and experimental setup

In this section, we first go through the fabrication steps necessary to produce carbon nanotube electro-mechanical resonators. After this, we give some details about the experimental setup used to perform all the measurements presented in this manuscript.

C.1 Device fabrication

The type of fabrication we choose consists in the definition of the three terminals (source, drain and gate) as a first step. At the end of the fabrication process carbon nanotubes are grown by chemical vapour deposition (CVD). In this way, the CNT does not see any contaminants due to fabrication and this ensures very high level of cleanliness for the resonator.

C.1.1 Fabrication of prepatterned chips

As a substrate, a highly resistive silicon (Si) wafer, capped with thermally grown silicon dioxide (SiO_2), is used to avoid that any RF signal could leak out from the device into the substrate. A gate electrode is defined by UV-photolithography and followed by a metal deposition of 5nm of tungsten (W) adhesion layer and 100nm of Platinum (Pt). After that, 150nm of plasma-enhanched chemical vapour deposited (PECVD) SiO_2 is grown all over the wafer, covering also the gate. The thickness of this oxide layer will define the separation between the gate electrode and the suspended CNT. Source and drain electrodes are patterned in the same way as the gate. The metal thickness is also in this case 5nm of W plus 100nm of Pt. The distance between source and drain varies between 1.3μm and 2μm. Finally, the SiO_2 on top of the gate is removed via reactive ion etching (RIE) with a mixture of argon (Ar) and CHF_3 gases. The final result is illustrated in Fig.C.1(a)

where a schematic cross section is shown. In Fig C.1(b) a scanning electron microscope (SEM) image shows the top view.

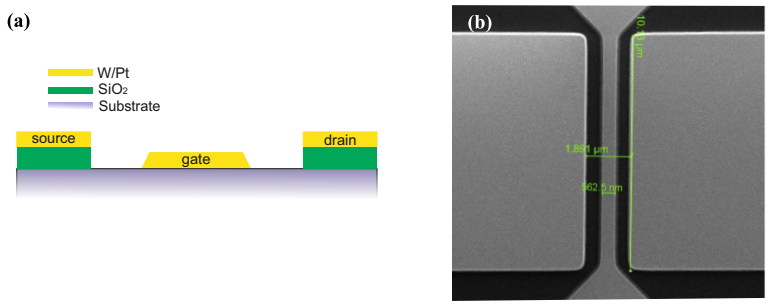

FIGURE C.1: Pre-patterned chip. (a) Schematic cross section of the different layers. (b) Scanning electronic microscope (SEM) image of one of the chips.

C.1.2 Fabrication of ultraclean suspended carbon nanotube devices

Here, we proceed with the CVD growth of CNTs. Squared openings of 600nm x 600nm are patterned in PMMA by electron beam lithography (EBL), just on top of the source electrode at a distance of 2μm from the trench. A methanol solution containing iron/molybdenum (Fe/Mo) based catalyst nanoparticles (with an alumina Al_2O_3 support) is drop-casted on the entire chip. The nanoparticles spread everywhere, and precipitate in the opening previously defined in the PMMA. After the evaporation of the methanol and the lift-off of the PMMA in acetone, catalyst nanoparticles remain attached on the electrode and define a square (see Fig.C.2(a), whity spot highlighted in the blue square). In the next step, the chip is exposed to oxygen plasma for few minutes to burn away any residues of organic layer previously deposited. Finally, the chip is transferred in a CVD oven for the growth. CNTs are grown by a decomposition process of methane gas (CH_4) into carbon and hydrogen where the Fe catalysts are located. Nanotubes are grown by the "fast heating" method. Instead of placing the chip in the center of the oven during the whole growth process, the method consists in rapidly sliding the quartz tube, so that the sample moves from a position outside the oven to the center, whose temperature is $T = 830°C$. This process is performed while flushing hydrogen (400 ml_n/min), argon (500 ml_n/min) and methane (550 ml_n/min) gases for 12 minutes. In Fig.C.2(b) is shown a $\sim 1.8\mu m$ long CNT contacted electrically to source and drain electrodes suspended over shallow trench (150nm above the local gate). The "fast heating" method has an important asset compared to the usual growth. We observe that electrodes are much

less deformed than with the usual growth method. To conclude this fabrication section we want to notice that the growth direction is still random and many tubes are not bridging source and drain. For this reason, to increase the statistic on every chip there are 40 of this kind of devices. Moreover, the production of this chip is made in a wafer-scale. For this we benefit of the collaboration with Nanofabrication Facility at University of California, Santa Barbara (UCSB).

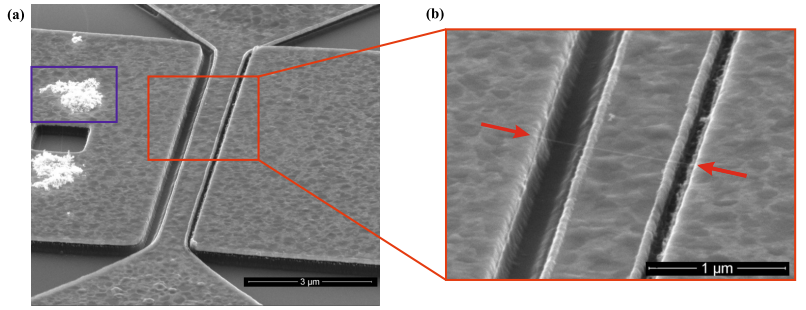

FIGURE C.2: SEM images of a suspended carbon nanotude device. (a) The highlighted blue area is where catalyst nanoparticles are deposited. (b) Zoom-in of the part of the device where the nanotube is contacted and suspended (pointed by red arrows).

C.2 Measurement setup

After the growth, we measure at room temperature with a probe station the source-drain resistance R_{SD}. We also check if there is any leakage between the leads electrodes and the gate. We select samples when R_{SD} falls between $\sim$ 30 kOhm and $\sim$ 150 kOhm. This is a good indication that the device could exhibit nice electrical properties at low temperatures. Figure C.3 shows a schematic of the low temperature measurement setup. We perform the measurement in a Triton 200, a cryogen-free dilution refrigerator from Oxford Instrument with a base temperature of 15 mK. This system is equipped with both RF-lines (8) and DC-lines (12). For the high frequency lines we use UT85-SS-SS stainless steel coaxial cables from room temperature to the 700 mK still stage. To minimize the heat conduction, superconducting UT85-Nb-Nb coaxial cables are used from the 700 mK plate to the mixing chamber stage. These lines (except the one used for the read-out of signals) are attenuated by cryogenic attenuators to decrease the thermal electromagnetic noise from room temperature and also to thermally anchor at every stage the inner conductors. The attenuation is 10 dB at T=45K, 20 dB at T=3K, 6 dB at 700 mK and 20 db on the source line

at the mixing chamber. For the gate at the mixing chamber we use a directional coupler, with an attenuation of 10 dB, to physically interrupt the central part of the coaxial line. For the DC lines, we choose thermocoax (at room temperature around 100 Ohm) Cu/NbTi cables filtered at room temperature with π-filters. At the mixing chamber stage powder filters further filter out high frequency noise. The thermalisation of the lines is realized by pressing them between two gold-plated oxygen-free copper clamps thermally anchored at every stage. Bias tees connect RF and DC lines to apply low and high frequency signals at the same time. DC- blocks are placed between cryostat RF ports at room temperature and RF sources to prevent that low frequency noise is injected into the system. To apply DC voltages we use SIM928 SRS isolated voltage sources. MHz signals are generated with Agilent E8257D PSG sources. The output signal from the device is filtered with an RLC resonator (at the mixing chamber) and amplified at 3K with a HEMT amplifier (calibration is described in the AppendixA). At room temperature we amplify again the signal with a low noise amplifier SA-220F5 NF (G=200).
We measure output signals using a UHFLI (Zurich Instruments) in lock-in or spectrum mode, depending on the type of measurement we want to perform.

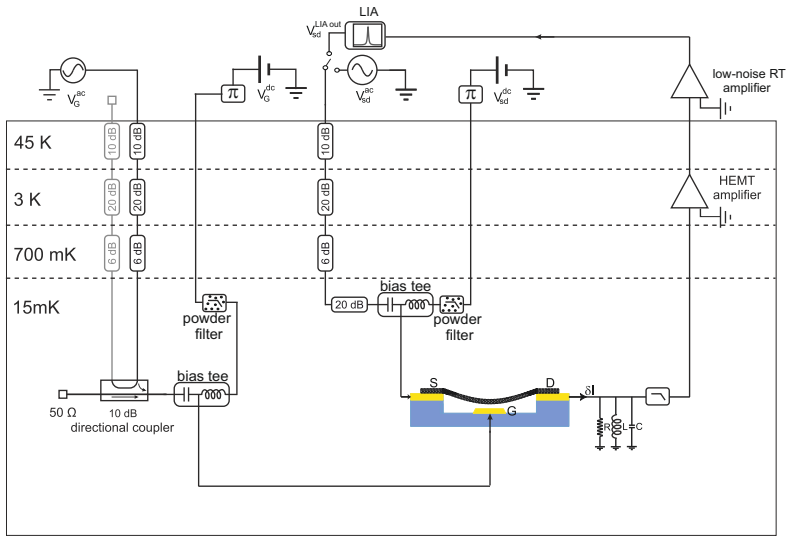

FIGURE C.3: Schematic of the measurement setup with the cryogenic wiring.

.

Bibliography

[1] Andrew N Cleland. *Foundations of nanomechanics: from solid-state theory to device applications*. Springer Science & Business Media, 2013 (cit. on p. 11).

[2] Gerd Binnig, Calvin F Quate, and Ch Gerber. "Atomic force microscope". In: *Physical review letters* 56.9 (1986), p. 930 (cit. on p. 11).

[3] Franz J Giessibl, Stefan Hembacher, Hartmut Bielefeldt, and Jochen Mannhart. "Subatomic features on the silicon (111)-(7× 7) surface observed by atomic force microscopy". In: *Science* 289.5478 (2000), pp. 422–425 (cit. on p. 11).

[4] Andrew N Cleland and Michael L Roukes. "A nanometre-scale mechanical electrometer". In: *Nature* 392.6672 (1998), p. 160 (cit. on pp. 11, 12).

[5] Robert G. Knobel and Andrew N. Cleland. "Nanometre-scale displacement sensing using a single electron transistor". In: *Nature* 424.6946 (2003), pp. 291–293 (cit. on pp. 11, 12, 53, 61).

[6] Michael T Woodside and Paul L McEuen. "Scanned probe imaging of single-electron charge states in nanotube quantum dots". In: *Science* 296.5570 (2002), pp. 1098–1101 (cit. on pp. 11, 13, 61).

[7] Benjamin Lassagne, Yury Tarakanov, Jari Kinaret, Daniel Garcia-Sanchez, and Adrian Bachtold. "Coupling mechanics to charge transport in carbon nanotube mechanical resonators". In: *Science* 325.5944 (2009), pp. 1107–1110 (cit. on pp. 11, 13, 40, 44, 53, 57, 61).

[8] Gary A Steele, Andreas K Hüttel, Benoit Witkamp, Menno Poot, Harold B Meerwaldt, Leo P Kouwenhoven, and Herre SJ van der Zant. "Strong coupling between single-electron tunneling and nanomechanical motion". In: *Science* 325.5944 (2009), pp. 1103–1107 (cit. on pp. 11, 13, 40, 53, 57, 61).

[9] Natalia Ares, Tian Pei, Aquila Mavalankar, Matthias Mergenthaler, Jamie H Warner, G Andrew D Briggs, and Edward A Laird. "Resonant optomechanics with a vibrating carbon nanotube and a radio-frequency cavity". In: *Physical review letters* 117.17 (2016), p. 170801 (cit. on pp. 11, 40, 53, 57, 61).

[10] Yutian Wen, Natalia Ares, FJ Schupp, T Pei, GAD Briggs, and EA Laird. "A coherent nanomechanical oscillator driven by single-electron tunnelling". In: *Nature Physics* (2019) (cit. on pp. 11, 13).

[11] MD LaHaye, Olivier Buu, Benedetta Camarota, and KC Schwab. "Approaching the quantum limit of a nanomechanical resonator". In: *Science* 304.5667 (2004), pp. 74–77 (cit. on p. 11).

[12] A Naik, O Buu, MD LaHaye, AD Armour, AA Clerk, MP Blencowe, and KC Schwab. "Cooling a nanomechanical resonator with quantum back-action". In: *Nature* 443.7108 (2006), p. 193 (cit. on pp. 11, 49, 53, 57, 61).

[13] CA Regal, JD Teufel, and KW Lehnert. "Measuring nanomechanical motion with a microwave cavity interferometer". In: *Nature Physics* 4.7 (2008), p. 555 (cit. on p. 12).

[14] John D Teufel, Tobias Donner, Dale Li, Jennifer W Harlow, MS Allman, Katarina Cicak, Adam J Sirois, Jed D Whittaker, Konrad W Lehnert, and Raymond W Simmonds. "Sideband cooling of micromechanical motion to the quantum ground state". In: *Nature* 475.7356 (2011), p. 359 (cit. on p. 12).

[15] MD LaHaye, J Suh, PM Echternach, Keith C Schwab, and Michael L Roukes. "Nanomechanical measurements of a superconducting qubit". In: *Nature* 459.7249 (2009), p. 960 (cit. on pp. 12, 53, 57, 61).

[16] KJ Lulla, Martial Defoort, Christophe Blanc, Olivier Bourgeois, and Eddy Collin. "Evidence for the role of normal-state electrons in nanoelectromechanical damping mechanisms at very low temperatures". In: *Physical review letters* 110.17 (2013), p. 177206 (cit. on p. 12).

[17] Adrien Noury, Jorge Vergara-Cruz, Pascal Morfin, Bernard Plaçais, Maria C Gordillo, Jordi Boronat, Sébastien Balibar, and Adrian Bachtold. "Layering transition in superfluid helium adsorbed on a carbon nanotube mechanical resonator". In: *Physical review letters* 122.16 (2019), p. 165301 (cit. on p. 12).

[18] AM Guenault, A Guthrie, RP Haley, S Kafanov, Yu A Pashkin, GR Pickett, V Tsepelin, DE Zmeev, E Collin, R Gazizulin, et al. "Detecting the" phonon wind" in superfluid ^{4}He by a nanomechanical resonator". In: *arXiv preprint arXiv:1907.01947* (2019) (cit. on p. 12).

[19] AM Guénault, A Guthrie, RP Haley, S Kafanov, Yu A Pashkin, GR Pickett, M Poole, R Schanen, V Tsepelin, DE Zmeev, et al. "Probing superfluid He 4 with high-frequency nanomechanical resonators down to millikelvin temperatures". In: *Physical Review B* 100.2 (2019), p. 020506 (cit. on p. 12).

[20] Aaron D O'Connell, Max Hofheinz, Markus Ansmann, Radoslaw C Bialczak, Mike Lenander, Erik Lucero, Matthew Neeley, Daniel Sank, H Wang, Ms Weides, et al. "Quantum ground state and single-phonon control of a mechanical resonator". In: *Nature* 464.7289 (2010), p. 697 (cit. on p. 12).

[21] Akshay K Naik, MS Hanay, WK Hiebert, XL Feng, and Michael L Roukes. "Towards single-molecule nanomechanical mass spectrometry". In: *Nature nanotechnology* 4.7 (2009), p. 445 (cit. on p. 12).

[22] Julien Chaste, A Eichler, J Moser, G Ceballos, R Rurali, and A Bachtold. "A nanomechanical mass sensor with yoctogram resolution". In: *Nature nanotechnology* 7.5 (2012), p. 301 (cit. on pp. 12, 13, 40).

[23] A Mehlin, F Xue, D Liang, HF Du, MJ Stolt, S Jin, ML Tian, and M Poggio. "Stabilized skyrmion phase detected in MnSi nanowires by dynamic cantilever magnetometry". In: *Nano letters* 15.7 (2015), pp. 4839–4844 (cit. on p. 12).

[24] B Gross, DP Weber, D Rüffer, A Buchter, F Heimbach, A Fontcuberta i Morral, D Grundler, and M Poggio. "Dynamic cantilever magnetometry of individual CoFeB nanotubes". In: *Physical Review B* 93.6 (2016), p. 064409 (cit. on p. 12).

[25] Daniel Rugar, CS Yannoni, and JA Sidles. "Mechanical detection of magnetic resonance". In: *Nature* 360.6404 (1992), p. 563 (cit. on p. 12).

[26] Daniel Rugar, Raffi Budakian, HJ Mamin, and BW Chui. "Single spin detection by magnetic resonance force microscopy". In: *Nature* 430.6997 (2004), pp. 329–332 (cit. on p. 12).

[27] HJ Mamin and D Rugar. "Sub-attonewton force detection at millikelvin temperatures". In: *Applied Physics Letters* 79.20 (2001), pp. 3358–3360 (cit. on p. 12).

[28] HJ Mamin, M Poggio, CL Degen, and D Rugar. "Nuclear magnetic resonance imaging with 90-nm resolution". In: *Nature nanotechnology* 2.5 (2007), p. 301 (cit. on pp. 12, 49, 64).

[29] CL Degen, M Poggio, HJ Mamin, CT Rettner, and D Rugar. "Nanoscale magnetic resonance imaging". In: *Proceedings of the National Academy of Sciences* 106.5 (2009), pp. 1313–1317 (cit. on pp. 12, 49, 64).

[30] Jan Gieseler, Bradley Deutsch, Romain Quidant, and Lukas Novotny. "Subkelvin parametric feedback cooling of a laser-trapped nanoparticle". In: *Physical review letters* 109.10 (2012), p. 103603 (cit. on pp. 13, 40).

[31] Francesco Ricci, Marc T Cuairan, Gerard P Conangla, Andreas W Schell, and Romain Quidant. "Accurate mass measurement of a levitated nanomechanical resonator for precision force-sensing". In: *Nano letters* (2019) (cit. on p. 13).

[32] Joel Moser, Alexander Eichler, Johannes Güttinger, Mark I Dykman, and Adrian Bachtold. "Nanotube mechanical resonators with quality factors of up to 5 million". In: *Nature nanotechnology* 9.12 (2014), p. 1007 (cit. on pp. 13, 40–42, 44, 46, 47, 56).

[33] SL De Bonis, C Urgell, W Yang, C Samanta, Adrien Noury, J Vergara-Cruz, Q Dong, Y Jin, and A Bachtold. "Ultrasensitive displacement noise measurement of carbon nanotube mechanical resonators". In: *Nano letters* 18.8 (2018), pp. 5324–5328 (cit. on pp. 13, 54, 56).

[34] Martino Poggio and Benedikt E Herzog. "Force-detected nuclear magnetic resonance". In: *Micro and Nano Scale NMR: Technologies and Systems (Wiley, 2018) p* 381 (2018) (cit. on p. 13).

[35] Julien Chaste, M Sledzinska, M Zdrojek, Joel Moser, and Adrian Bachtold. "High-frequency nanotube mechanical resonators". In: *Applied Physics Letters* 99.21 (2011), p. 213502 (cit. on p. 13).

[36] Edward A Laird, Fei Pei, Wei Tang, Gary A Steele, and Leo P Kouwenhoven. "A high quality factor carbon nanotube mechanical resonator at 39 GHz". In: *Nano letters* 12.1 (2011), pp. 193–197 (cit. on p. 13).

[37] Andreas K Huttel, Gary A Steele, Benoit Witkamp, Menno Poot, Leo P Kouwenhoven, and Herre SJ van der Zant. "Carbon nanotubes as ultrahigh quality factor mechanical resonators". In: *Nano letters* 9.7 (2009), pp. 2547–2552 (cit. on pp. 13, 40).

[38] Vera Sazonova, Yuval Yaish, Hande Üstünel, David Roundy, Tomás A Arias, and Paul L McEuen. "A tunable carbon nanotube electromechanical oscillator". In: *Nature* 431.7006 (2004), p. 284 (cit. on pp. 13, 40, 42, 43, 57, 58).

[39] Gernot Gruber, Carles Urgell, Alexandros Tavernarakis, Alexandros Stavrinadis, Slaven Tepsic, Cesar Magen, Soraya Sangiao, Jose Maria De Teresa, Pierre Verlot, and Adrian Bachtold. "Mass sensing for the advanced fabrication of nanomechanical resonators". In: *Nano letters* (2019) (cit. on p. 13).

[40] Joel Moser, J Güttinger, Alexander Eichler, María J Esplandiu, DE Liu, MI Dykman, and Adrian Bachtold. "Ultrasensitive force detection with a nanotube mechanical resonator". In: *Nature nanotechnology* 8.7 (2013), p. 493 (cit. on pp. 13, 40, 42, 44, 46, 47).

[41] Sander J Tans, Michel H Devoret, Hongjie Dai, Andreas Thess, Richard E Smalley, LJ Geerligs, and Cees Dekker. "Individual single-wall carbon nanotubes as quantum wires". In: *Nature* 386.6624 (1997), p. 474 (cit. on pp. 13, 30).

[42] Avishai Benyamini, Assaf Hamo, S Viola Kusminskiy, Felix von Oppen, and Shahal Ilani. "Real-space tailoring of the electron–phonon coupling in ultraclean nanotube mechanical resonators". In: *Nature Physics* 10.2 (2014), p. 151 (cit. on pp. 13, 40, 53, 57, 61, 62).

[43] Ilya Khivrich, Aashish A Clerk, and Shahal Ilani. "Nanomechanical pump–probe measurements of insulating electronic states in a carbon nanotube". In: *Nature nanotechnology* 14.2 (2019), p. 161 (cit. on pp. 13, 53, 56, 57, 61, 62).

[44] KJG Götz, DR Schmid, FJ Schupp, PL Stiller, Ch Strunk, and AK Hüttel. "Nanomechanical characterization of the Kondo charge dynamics in a carbon nanotube". In: *Physical review letters* 120.24 (2018), p. 246802 (cit. on pp. 13, 53, 57, 61).

[45] Yutian Wen, N Ares, T Pei, GAD Briggs, and Edward Alexander Laird. "Measuring carbon nanotube vibrations using a single-electron transistor as a fast linear amplifier". In: *Applied Physics Letters* 113.15 (2018), p. 153101 (cit. on p. 13).

[46] Wenjie Liang, Marc Bockrath, Dolores Bozovic, Jason H Hafner, M Tinkham, and Hongkun Park. "Fabry-Perot interference in a nanotube electron waveguide". In: *Nature* 411.6838 (2001), p. 665 (cit. on pp. 13, 37).

[47] Ioannis Tsioutsios. "Mechanical Resonators Based on Graphene and Carbon Nanotubes, PhD Thesis". PhD thesis. 2016 (cit. on pp. 16, 19).

[48] Herbert B Callen and Theodore A Welton. "Irreversibility and generalized noise". In: *Physical Review* 83.1 (1951), p. 34 (cit. on p. 17).

[49] L.D. Landau and E.M. Lifschitz. *Statistical Physics, Part 1*. Vol. 34. 1981 (cit. on p. 18).

[50] Ron Lifschitz and Cross M.C. *Nonlinear dynamics of nanomechanical and micromechanical resonators. Reviews of nonlinear dynamics and complexity*. Vol. 1. 2008 (cit. on p. 20).

[51] HW Ch Postma, I Kozinsky, A Husain, and ML Roukes. "Dynamic range of nanotube-and nanowire-based electromechanical systems". In: *Applied Physics Letters* 86.22 (2005), p. 223105 (cit. on p. 20).

[52] LG Villanueva, RB Karabalin, MH Matheny, D Chi, JE Sader, and ML Roukes. "Nonlinearity in nanomechanical cantilevers". In: *Physical Review B* 87.2 (2013), p. 024304 (cit. on p. 20).

[53] Jan Gieseler, Lukas Novotny, and Romain Quidant. "Thermal nonlinearities in a nanomechanical oscillator". In: *Nature physics* 9.12 (2013), p. 806 (cit. on pp. 20, 40, 46, 47).

[54] Olivier Maillet, Xin Zhou, Rasul Gazizulin, Ana Maldonado Cid, Martial Defoort, Olivier Bourgeois, and Eddy Collin. "Nonlinear frequency transduction of nanomechanical Brownian motion". In: *Physical Review B* 96.16 (2017), p. 165434 (cit. on pp. 20, 40).

[55] Alexander Eichler, Joel Moser, Julien Chaste, M Zdrojek, I Wilson-Rae, and Adrian Bachtold. "Nonlinear damping in mechanical resonators made from carbon nanotubes and graphene". In: *Nature nanotechnology* 6.6 (2011), p. 339 (cit. on pp. 20, 40).

[56] Matthias Imboden, Oliver A Williams, and Pritiraj Mohanty. "Observation of nonlinear dissipation in piezoresistive diamond nanomechanical resonators by heterodyne down-mixing". In: *Nano letters* 13.9 (2013), pp. 4014–4019 (cit. on p. 20).

[57] Vera Sazonova. "A tunable carbon nanotube resonator, PhD Thesis". PhD thesis. 2004 (cit. on pp. 21, 22).

[58] S Sapmaz, Ya M Blanter, L Gurevich, and HSJ Van der Zant. "Carbon nanotubes as nanoelectromechanical systems". In: *Physical Review B* 67.23 (2003), p. 235414 (cit. on p. 21).

[59] BD Hauer, C Doolin, KSD Beach, and JP Davis. "A general procedure for thermomechanical calibration of nano/micro-mechanical resonators". In: *Annals of Physics* 339 (2013), pp. 181–207 (cit. on p. 21).

[60] V. Gavryushin. *Graphene Brillouin Zone and Electronic Energy Dispersion (Wolfram Demonstrations Project, 2011)* (cit. on p. 26).

[61] Jean-Christophe Charlier, Xavier Blase, and Stephan Roche. "Electronic and transport properties of nanotubes". In: *Reviews of modern physics* 79.2 (2007), p. 677 (cit. on p. 26).

[62] Stephanie Reich, Janina Maultzsch, Christian Thomsen, and Pablo Ordejon. "Tight-binding description of graphene". In: *Physical Review B* 66.3 (2002), p. 035412 (cit. on p. 26).

[63] C. Schoenenberger. *Band structure of graphene and carbon nanotubes*. 2000 (cit. on p. 28).

[64] J. Alfonsi. *Zone of a single-walled carbon nanotube (Wolfram Demonstrations Project, 2008)* (cit. on p. 28).

[65] Liu Yang and Jie Han. "Electronic structure of deformed carbon nanotubes". In: *Physical Review Letters* 85.1 (2000), p. 154 (cit. on p. 28).

[66] Charles L Kane and EJ Mele. "Size, shape, and low energy electronic structure of carbon nanotubes". In: *Physical Review Letters* 78.10 (1997), p. 1932 (cit. on p. 28).

[67] CJ Gorter. "A possible explanation of the increase of the electrical resistance of thin metal films at low temperatures and small field strengths". In: *Physica* 17.8 (1951), pp. 777–780 (cit. on p. 30).

[68] IO Kulik and RI Shekhter. "Kinetic phenomena and charge-discreteness effects in granulated media". In: *Zhur. Eksper. Teoret. Fiziki* 68.2 (1975), pp. 623–640 (cit. on p. 30).

[69] I Giaever and HR Zeller. "Superconductivity of small tin particles measured by tunneling". In: *Physical Review Letters* 20.26 (1968), p. 1504 (cit. on p. 30).

[70] Theodore A Fulton and Gerald J Dolan. "Observation of single-electron charging effects in small tunnel junctions". In: *Physical review letters* 59.1 (1987), p. 109 (cit. on p. 30).

[71] CWJ Beenakker. "Theory of Coulomb-blockade oscillations in the conductance of a quantum dot". In: *Physical Review B* 44.4 (1991), p. 1646 (cit. on pp. 30, 36).

[72] Andreas Fuhrer. "Phase coherence, orbital and spin states in quantum rings". PhD thesis. ETH Zurich, 2003 (cit. on p. 30).

[73] Leo P Kouwenhoven, Charles M Marcus, Paul L McEuen, Seigo Tarucha, Robert M Westervelt, and Ned S Wingreen. "Electron transport in quantum dots". In: *Mesoscopic electron transport*. Springer, 1997, pp. 105–214 (cit. on p. 36).

[74] M Büttiker. "Quantized transmission of a saddle-point constriction". In: *Physical Review B* 41.11 (1990), p. 7906 (cit. on p. 36).

[75] Gregory Breit and Eugene Wigner. "Capture of slow neutrons". In: *Physical review* 49.7 (1936), p. 519 (cit. on p. 36).

[76] Jun Kondo. "Resistance minimum in dilute magnetic alloys". In: *Progress of theoretical physics* 32.1 (1964), pp. 37–49 (cit. on p. 37).

[77] Kenneth G Wilson. "The renormalization group: Critical phenomena and the Kondo problem". In: *Reviews of modern physics* 47.4 (1975), p. 773 (cit. on p. 37).

[78] WJ De Haas and GJ Van den Berg. "The electrical resistance of gold and silver at low temperatures". In: *Physica* 3.6 (1936), pp. 440–449 (cit. on p. 37).

[79] Jesper Nygård, David Henry Cobden, and Poul Erik Lindelof. "Kondo physics in carbon nanotubes". In: *Nature* 408.6810 (2000), p. 342 (cit. on p. 37).

[80] Pablo Jarillo-Herrero, Jing Kong, Herre SJ Van Der Zant, Cees Dekker, Leo P Kouwenhoven, and Silvano De Franceschi. "Orbital Kondo effect in carbon nanotubes". In: *Nature* 434.7032 (2005), p. 484 (cit. on p. 37).

[81] MM Desjardins, JJ Viennot, MC Dartiailh, LE Bruhat, MR Delbecq, M Lee, M-S Choi, A Cottet, and T Kontos. "Observation of the frozen charge of a Kondo resonance". In: *Nature* 545.7652 (2017), p. 71 (cit. on p. 37).

[82] J Scott Bunch, Arend M Van Der Zande, Scott S Verbridge, Ian W Frank, David M Tanenbaum, Jeevak M Parpia, Harold G Craighead, and Paul L McEuen. "Electromechanical resonators from graphene sheets". In: *Science* 315.5811 (2007), pp. 490–493 (cit. on p. 40).

[83] Vibhor Singh, Shamashis Sengupta, Hari S Solanki, Rohan Dhall, Adrien Allain, Sajal Dhara, Prita Pant, and Mandar M Deshmukh. "Probing thermal expansion of graphene and modal dispersion at low-temperature using graphene nanoelectromechanical systems resonators". In: *Nanotechnology* 21.16 (2010), p. 165204 (cit. on p. 40).

[84] M Will, M Hamer, M Muller, Adrien Noury, P Weber, A Bachtold, RV Gorbachev, C Stampfer, and J Guttinger. "High quality factor graphene-based two-dimensional heterostructure mechanical resonator". In: *Nano letters* 17.10 (2017), pp. 5950–5955 (cit. on p. 40).

[85] XL Feng, Rongrui He, Peidong Yang, and ML Roukes. "Very high frequency silicon nanowire electromechanical resonators". In: *Nano Letters* 7.7 (2007), pp. 1953–1959 (cit. on p. 40).

[86] Eduardo Gil-Santos, Daniel Ramos, Javier Martínez, Marta Fernández-Regúlez, Ricardo García, Álvaro San Paulo, Montserrat Calleja, and Javier Tamayo. "Nanomechanical mass sensing and stiffness spectrometry based on two-dimensional vibrations of resonant nanowires". In: *Nature nanotechnology* 5.9 (2010), p. 641 (cit. on p. 40).

[87] Marc Sansa, Marta Fernández-Regúlez, Álvaro San Paulo, and Francesc Pérez-Murano. "Electrical transduction in nanomechanical resonators based on doubly clamped bottom-up silicon nanowires". In: *Applied Physics Letters* 101.24 (2012), p. 243115 (cit. on p. 40).

[88] Michele Montinaro, Gunter Wust, Mathieu Munsch, Yannik Fontana, Eleonora Russo-Averchi, Martin Heiss, Anna Fontcuberta i Morral, Richard J Warburton, and Martino Poggio. "Quantum dot opto-mechanics in a fully self-assembled nanowire". In: *Nano letters* 14.8 (2014), pp. 4454–4460 (cit. on p. 40).

[89] Nikolai Kiesel, Florian Blaser, Uroš Delić, David Grass, Rainer Kaltenbaek, and Markus Aspelmeyer. "Cavity cooling of an optically levitated submicron particle". In: *Proceedings of the National Academy of Sciences* 110.35 (2013), pp. 14180–14185 (cit. on p. 40).

[90] John M Nichol, Eric R Hemesath, Lincoln J Lauhon, and Raffi Budakian. "Displacement detection of silicon nanowires by polarization-enhanced fiber-optic interferometry". In: *Applied Physics Letters* 93.19 (2008), p. 193110 (cit. on p. 40).

[91] Laure Mercier de Lépinay, Benjamin Pigeau, Benjamin Besga, Pascal Vincent, Philippe Poncharal, and Olivier Arcizet. "A universal and ultrasensitive vectorial nanomechanical sensor for imaging 2D force fields". In: *Nature nanotechnology* 12.2 (2017), p. 156 (cit. on pp. 40, 46).

[92] Nicola Rossi, Floris R Braakman, Davide Cadeddu, Denis Vasyukov, Gözde Tütüncüoglu, Anna Fontcuberta i Morral, and Martino Poggio. "Vectorial scanning force microscopy using a nanowire sensor". In: *Nature nanotechnology* 12.2 (2017), p. 150 (cit. on pp. 40, 46, 47).

[93] Hsin-Ying Chiu, Peter Hung, Henk W Ch Postma, and Marc Bockrath. "Atomic-scale mass sensing using carbon nanotube resonators". In: *Nano letters* 8.12 (2008), pp. 4342–4346 (cit. on p. 40).

[94] Zenghui Wang, Jiang Wei, Peter Morse, J Gregory Dash, Oscar E Vilches, and David H Cobden. "Phase transitions of adsorbed atoms on the surface of a carbon nanotube". In: *Science* 327.5965 (2010), pp. 552–555 (cit. on p. 40).

[95] Yaxing Zhang, J Moser, J Güttinger, A Bachtold, and MI Dykman. "Interplay of driving and frequency noise in the spectra of vibrational systems". In: *Physical review letters* 113.25 (2014), p. 255502 (cit. on p. 40).

[96] Tengfei Miao, Sinchul Yeom, Peng Wang, Brian Standley, and Marc Bockrath. "Graphene nanoelectromechanical systems as stochastic-frequency oscillators". In: *Nano letters* 14.6 (2014), pp. 2982–2987 (cit. on p. 40).

[97] Guang-Wei Deng, Dong Zhu, Xin-He Wang, Chang-Ling Zou, Jiang-Tao Wang, Hai-Ou Li, Gang Cao, Di Liu, Yan Li, Ming Xiao, et al. "Strongly coupled nanotube electromechanical resonators". In: *Nano letters* 16.9 (2016), pp. 5456–5462 (cit. on pp. 40, 61).

[98] Robert De Alba, Francesco Massel, Isaac R Storch, TS Abhilash, Aaron Hui, Paul L McEuen, Harold G Craighead, and Jeevak M Parpia. "Tunable phonon-cavity coupling in graphene membranes". In: *Nature nanotechnology* 11.9 (2016), p. 741 (cit. on p. 40).

[99] John P Mathew, Raj N Patel, Abhinandan Borah, R Vijay, and Mandar M Deshmukh. "Dynamical strong coupling and parametric amplification of mechanical modes of graphene drums". In: *Nature nanotechnology* 11.9 (2016), p. 747 (cit. on p. 40).

[100] Marc Ganzhorn and Wolfgang Wernsdorfer. "Dynamics and dissipation induced by single-electron tunneling in carbon nanotube nanoelectromechanical systems". In: *Physical review letters* 108.17 (2012), p. 175502 (cit. on p. 40).

[101] Arnaud Gloppe, Pierre Verlot, Eva Dupont-Ferrier, Alessandro Siria, Philippe Poncharal, Guillaume Bachelier, Pascal Vincent, and Olivier Arcizet. "Bidimensional nano-optomechanics and topological backaction in a non-conservative radiation force field". In: *Nature nanotechnology* 9.11 (2014), p. 920 (cit. on p. 40).

[102] Antoine Reserbat-Plantey, Kevin G Schädler, Louis Gaudreau, Gabriele Navickaite, Johannes Güttinger, Darrick Chang, Costanza Toninelli, Adrian Bachtold, and Frank HL Koppens. "Electromechanical control of nitrogen-vacancy defect emission using graphene NEMS". In: *Nature communications* 7 (2016), p. 10218 (cit. on p. 40).

[103] ST Purcell, P Vincent, Catherine Journet, and Vu Thien Binh. "Tuning of nanotube mechanical resonances by electric field pulling". In: *Physical Review Letters* 89.27 (2002), p. 276103 (cit. on p. 40).

[104] Changyao Chen, Sami Rosenblatt, Kirill I Bolotin, William Kalb, Philip Kim, Ioannis Kymissis, Horst L Stormer, Tony F Heinz, and James Hone. "Performance of monolayer graphene nanomechanical resonators with electrical readout". In: *Nature nanotechnology* 4.12 (2009), p. 861 (cit. on p. 40).

[105] Vincent Gouttenoire, Thomas Barois, Sorin Perisanu, Jean-Louis Leclercq, Stephen T Purcell, Pascal Vincent, and Anthony Ayari. "Digital and FM demodulation of a doubly clamped single-walled carbon-nanotube oscillator: towards a nanotube cell phone". In: *Small* 6.9 (2010), pp. 1060–1065 (cit. on p. 40).

[106] Olivier Arcizet, Vincent Jacques, Alessandro Siria, Philippe Poncharal, Pascal Vincent, and Signe Seidelin. "A single nitrogen-vacancy defect coupled to a nanomechanical oscillator". In: *Nature Physics* 7.11 (2011), p. 879 (cit. on p. 40).

[107] Sebastian Stapfner, Lukas Ost, David Hunger, Jakob Reichel, Ivan Favero, and Eva Maria Weig. "Cavity-enhanced optical detection of carbon nanotube Brownian motion". In: *Applied Physics Letters* 102.15 (2013), p. 151910 (cit. on p. 40).

[108] V Singh, SJ Bosman, BH Schneider, Ya M Blanter, A Castellanos-Gomez, and GA Steele. "Optomechanical coupling between a multilayer graphene mechanical resonator and a superconducting microwave cavity". In: *Nature nanotechnology* 9.10 (2014), p. 820 (cit. on p. 40).

[109] X Song, M Oksanen, J Li, PJ Hakonen, and Mika A Sillanpää. "Graphene optomechanics realized at microwave frequencies". In: *Physical review letters* 113.2 (2014), p. 027404 (cit. on p. 40).

[110] Peter Weber, J Guttinger, Ioannis Tsioutsios, Darrick E Chang, and Adrian Bachtold. "Coupling graphene mechanical resonators to superconducting microwave cavities". In: *Nano letters* 14.5 (2014), pp. 2854–2860 (cit. on p. 40).

[111] Ben H Schneider, Vibhor Singh, Warner J Venstra, Harold B Meerwaldt, and Gary A Steele. "Observation of decoherence in a carbon nanotube mechanical resonator". In: *Nature communications* 5 (2014), p. 5819 (cit. on p. 40).

[112] A Nigues, A Siria, and Pierre Verlot. "Dynamical backaction cooling with free electrons". In: *Nature communications* 6.1 (2015), pp. 1–7 (cit. on p. 40).

[113] Robin M Cole, George A Brawley, Vivekananda P Adiga, Roberto De Alba, Jeevak M Parpia, Bojan Ilic, Harold G Craighead, and Warwick P Bowen. "Evanescent-field optical readout of graphene mechanical motion at room temperature". In: *Physical Review Applied* 3.2 (2015), p. 024004 (cit. on p. 40).

[114] I Tsioutsios, A Tavernarakis, J Osmond, P Verlot, and A Bachtold. "Real-time measurement of nanotube resonator fluctuations in an electron microscope". In: *Nano letters* 17.3 (2017), pp. 1748–1755 (cit. on p. 40).

[115] Johannes Güttinger, Adrien Noury, Peter Weber, Axel Martin Eriksson, Camille Lagoin, Joel Moser, Christopher Eichler, Andreas Wallraff, Andreas Isacsson, and Adrian Bachtold. "Energy-dependent path of dissipation in nanomechanical resonators". In: *Nature nanotechnology* 12.7 (2017), p. 631 (cit. on p. 40).

[116] A Tavernarakis, A Stavrinadis, A Nowak, I Tsioutsios, A Bachtold, and Pierre Verlot. "Optomechanics with a hybrid carbon nanotube resonator". In: *Nature communications* 9.1 (2018), p. 662 (cit. on p. 40).

[117] Shaoming Huang, Mike Woodson, Richard Smalley, and Jie Liu. "Growth mechanism of oriented long single walled carbon nanotubes using "fast-heating" chemical vapor deposition process". In: *Nano Letters* 4.6 (2004), pp. 1025–1028 (cit. on p. 41).

[118] Sébastien Jezouin, FD Parmentier, A Anthore, U Gennser, A Cavanna, Y Jin, and F Pierre. "Quantum limit of heat flow across a single electronic channel". In: *Science* 342.6158 (2013), pp. 601–604 (cit. on pp. 42, 57).

[119] Erwann Bocquillon, Vincent Freulon, J-M Berroir, Pascal Degiovanni, Bernard Plaçais, A Cavanna, Yong Jin, and Gwendal Fève. "Coherence and indistinguishability of single electrons emitted by independent sources". In: *Science* 339.6123 (2013), pp. 1054–1057 (cit. on pp. 42, 57).

[120] T Jullien, P Roulleau, B Roche, A Cavanna, Y Jin, and DC Glattli. "Quantum tomography of an electron". In: *Nature* 514.7524 (2014), p. 603 (cit. on p. 42).

[121] Q Dong, YX Liang, D Ferry, A Cavanna, U Gennser, L Couraud, and Y Jin. "Ultra-low noise high electron mobility transistors for high-impedance and low-frequency deep cryogenic readout electronics". In: *Applied Physics Letters* 105.1 (2014), p. 013504 (cit. on pp. 42, 67).

[122] Xuefeng Song, Mika Oksanen, Mika A Sillanpaa, HG Craighead, JM Parpia, and Pertti J Hakonen. "Stamp transferred suspended graphene mechanical resonators for radio frequency electrical readout". In: *Nano letters* 12.1 (2011), pp. 198–202 (cit. on p. 44).

[123] Peter Weber, Johannes Güttinger, Adrien Noury, Jorge Vergara-Cruz, and Adrian Bachtold. "Force sensitivity of multilayer graphene optomechanical devices". In: *Nature communications* 7 (2016), p. 12496 (cit. on pp. 44, 46, 47).

[124] John D Teufel, Tobias Donner, MA Castellanos-Beltran, Jennifer W Harlow, and Konrad W Lehnert. "Nanomechanical motion measured with an imprecision below that at the standard quantum limit". In: *Nature nanotechnology* 4.12 (2009), p. 820 (cit. on pp. 46, 47).

[125] Christoph Reinhardt, Tina Müller, Alexandre Bourassa, and Jack C Sankey. "Ultralow-noise SiN trampoline resonators for sensing and optomechanics". In: *Physical Review X* 6.2 (2016), p. 021001 (cit. on pp. 46, 47).

[126] Martin Heritier, Alexander Eichler, Y Pan, Urs Grob, Ivan Shorubalko, Marc D Krass, Ye Tao, and Christian L Degen. "Nanoladder cantilevers made from diamond and silicon". In: *Nano letters* 18.3 (2018), pp. 1814–1818 (cit. on pp. 46, 47).

[127] John M Nichol, Eric R Hemesath, Lincoln J Lauhon, and Raffi Budakian. "Nanomechanical detection of nuclear magnetic resonance using a silicon nanowire oscillator". In: *Physical Review B* 85.5 (2012), p. 054414 (cit. on pp. 46, 47, 49, 64).

[128] Yue Wang and Fabio Pistolesi. "Sensitivity of mixing-current technique to detect nanomechanical motion". In: *Physical Review B* 95.3 (2017), p. 035410 (cit. on p. 46).

[129] John M Nichol, Tyler R Naibert, Eric R Hemesath, Lincoln J Lauhon, and Raffi Budakian. "Nanoscale Fourier-transform magnetic resonance imaging". In: *Physical Review X* 3.3 (2013), p. 031016 (cit. on pp. 49, 64).

[130] AD Armour, MP Blencowe, and Yong Zhang. "Classical dynamics of a nanomechanical resonator coupled to a single-electron transistor". In: *Physical Review B* 69.12 (2004), p. 125313 (cit. on p. 49).

[131] Aashish A Clerk and Steven Bennett. "Quantum nanoelectromechanics with electrons, quasi-particles and Cooper pairs: effective bath descriptions and strong feedback effects". In: *New Journal of Physics* 7.1 (2005), p. 238 (cit. on p. 49).

[132] Gianluca Micchi, Rémi Avriller, and Fabio Pistolesi. "Mechanical signatures of the current blockade instability in suspended carbon nanotubes". In: *Physical review letters* 115.20 (2015), p. 206802 (cit. on pp. 49, 52, 59, 60, 62, 64, 76).

[133] Fabio Pistolesi and Sebastien Labarthe. "Current blockade in classical single-electron nanomechanical resonator". In: *Physical Review B* 76.16 (2007), p. 165317 (cit. on pp. 49, 52, 62, 64).

[134] Guillaume Weick, Felix Von Oppen, and Fabio Pistolesi. "Euler buckling instability and enhanced current blockade in suspended single-electron transistors". In: *Physical Review B* 83.3 (2011), p. 035420 (cit. on pp. 49, 52, 62, 64).

[135] Gianluca Micchi, Rémi Avriller, and Fabio Pistolesi. "Electromechanical transition in quantum dots". In: *Physical Review B* 94.12 (2016), p. 125417 (cit. on pp. 49, 64).

[136] Stefano Zippilli, Giovanna Morigi, and Adrian Bachtold. "Cooling carbon nanotubes to the phononic ground state with a constant electron current". In: *Physical review letters* 102.9 (2009), p. 096804 (cit. on p. 49).

[137] Fabio Santandrea, Leonid Y Gorelik, Robert I Shekhter, and Mats Jonson. "Cooling of nanomechanical resonators by thermally activated single-electron transport". In: *Physical review letters* 106.18 (2011), p. 186803 (cit. on p. 49).

[138] Pascal Stadler, Wolfgang Belzig, and Gianluca Rastelli. "Ground-state cooling of a carbon nanomechanical resonator by spin-polarized current". In: *Physical review letters* 113.4 (2014), p. 047201 (cit. on p. 49).

[139] Liliana Arrachea, Niels Bode, and Felix Von Oppen. "Vibrational cooling and thermoelectric response of nanoelectromechanical systems". In: *Physical Review B* 90.12 (2014), p. 125450 (cit. on p. 49).

[140] Pascal Stadler, Wolfgang Belzig, and Gianluca Rastelli. "Ground-state cooling of a mechanical oscillator by interference in Andreev reflection". In: *Physical review letters* 117.19 (2016), p. 197202 (cit. on p. 49).

[141] Jozef T Devreese and Alexandre S Alexandrov. "Fröhlich polaron and bipolaron: recent developments". In: *Reports on Progress in Physics* 72.6 (2009), p. 066501 (cit. on p. 52).

[142] Michael Galperin, Mark A Ratner, and Abraham Nitzan. "Hysteresis, switching, and negative differential resistance in molecular junctions: a polaron model". In: *Nano letters* 5.1 (2005), pp. 125–130 (cit. on p. 52).

[143] D Mozyrsky, MB Hastings, and I Martin. "Intermittent polaron dynamics: Born-Oppenheimer approximation out of equilibrium". In: *Physical Review B* 73.3 (2006), p. 035104 (cit. on p. 52).

[144] Markus Aspelmeyer, Tobias J Kippenberg, and Florian Marquardt. "Cavity optomechanics". In: *Reviews of Modern Physics* 86.4 (2014), p. 1391 (cit. on p. 52).

[145] J-M Pirkkalainen, SU Cho, Francesco Massel, J Tuorila, TT Heikkilä, PJ Hakonen, and MA Sillanpää. "Cavity optomechanics mediated by a quantum two-level system". In: *Nature communications* 6 (2015), p. 6981 (cit. on pp. 53, 57, 61).

[146] Yuma Okazaki, Imran Mahboob, Koji Onomitsu, Satoshi Sasaki, and Hiroshi Yamaguchi. "Gate-controlled electromechanical back-action induced by a quantum dot". In: *Nature communications* 7 (2016), p. 11132 (cit. on pp. 53, 57, 61).

[147] Edward A Laird, Ferdinand Kuemmeth, Gary A Steele, Kasper Grove-Rasmussen, Jesper Nygård, Karsten Flensberg, and Leo P Kouwenhoven. "Quantum transport in carbon nanotubes". In: *Reviews of Modern Physics* 87.3 (2015), p. 703 (cit. on p. 56).

[148] Mitali Banerjee, Moty Heiblum, Vladimir Umansky, Dima E Feldman, Yuval Oreg, and Ady Stern. "Observation of half-integer thermal Hall conductance". In: *Nature* 559.7713 (2018), p. 205 (cit. on p. 57).

[149] Maelle Kapfer, Preden Roulleau, M Santin, Ian Farrer, DA Ritchie, and DC Glattli. "A Josephson relation for fractionally charged anyons". In: *Science* 363.6429 (2019), pp. 846–849 (cit. on p. 57).

[150] Jun Zhu, M Brink, and PL McEuen. "Frequency shift imaging of quantum dots with single-electron resolution". In: *Applied Physics Letters* 87.24 (2005), p. 242102 (cit. on p. 61).

[151] Romain Stomp, Yoichi Miyahara, Sacha Schaer, Qingfeng Sun, Hong Guo, Peter Grutter, Sergei Studenikin, Philip Poole, and Andy Sachrajda. "Detection of single-electron charging in an individual InAs quantum dot by noncontact atomic-force microscopy". In: *Physical review letters* 94.5 (2005), p. 056802 (cit. on p. 61).

[152] Steven D Bennett, Lynda Cockins, Yoichi Miyahara, Peter Grütter, and Aashish A Clerk. "Strong electromechanical coupling of an atomic force microscope cantilever to a quantum dot". In: *Physical review letters* 104.1 (2010), p. 017203 (cit. on p. 61).

[153] Harold B Meerwaldt, Giorgi Labadze, Ben H Schneider, Ahmet Taspinar, Ya M Blanter, Herre SJ van der Zant, and Gary A Steele. "Probing the charge of a quantum dot with a nanomechanical resonator". In: *Physical Review B* 86.11 (2012), p. 115454 (cit. on p. 61).

[154] Inah Yeo, Pierre-Louis De Assis, Arnaud Gloppe, Eva Dupont-Ferrier, Pierre Verlot, Nitin S Malik, Emmanuel Dupuy, Julien Claudon, Jean-Michel Gérard, Alexia Auffèves, et al. "Strain-mediated coupling in a quantum dot–mechanical oscillator hybrid system". In: *Nature nanotechnology* 9.2 (2014), p. 106 (cit. on p. 62).

[155] Jeremie J Viennot, Xizheng Ma, and Konrad W Lehnert. "Phonon-number-sensitive electromechanics". In: *Physical review letters* 121.18 (2018), p. 183601 (cit. on p. 62).

[156] Francesco Fogliano, Benjamin Besga, Antoine Reigue, Philip Heringlake, Laure Mercier de Lépinay, Cyril Vaneph, Jakob Reichel, Benjamin Pigeau, and Olivier Arcizet. "Cavity nanooptomechanics in the ultrastrong coupling regime with ultrasensitive force sensors". In: *arXiv preprint arXiv:1904.01140* (2019) (cit. on p. 62).

[157] Jens Koch and Felix Von Oppen. "Franck-Condon blockade and giant Fano factors in transport through single molecules". In: *Physical review letters* 94.20 (2005), p. 206804 (cit. on p. 62).

[158] Renaud Leturcq, Christoph Stampfer, Kevin Inderbitzin, Lukas Durrer, Christofer Hierold, Eros Mariani, Maximilian G Schultz, Felix Von Oppen, and Klaus Ensslin. "Franck–Condon blockade in suspended carbon nanotube quantum dots". In: *Nature Physics* 5.5 (2009), p. 327 (cit. on p. 62).

[159] Hongkun Park, Jiwoong Park, Andrew KL Lim, Erik H Anderson, A Paul Alivisatos, and Paul L McEuen. "Nanomechanical oscillations in a single-C 60 transistor". In: *Nature* 407.6800 (2000), p. 57 (cit. on p. 62).

[160] S Sapmaz, P Jarillo-Herrero, Ya M Blanter, C Dekker, and HSJ Van Der Zant. "Tunneling in suspended carbon nanotubes assisted by longitudinal phonons". In: *Physical review letters* 96.2 (2006), p. 026801 (cit. on p. 62).

[161] Simon Rips and Michael J Hartmann. "Quantum information processing with nanomechanical qubits". In: *Physical review letters* 110.12 (2013), p. 120503 (cit. on pp. 62, 64).

[162] Jamie Gardner, Steven D Bennett, and Aashish A Clerk. "Mechanically probing coherent tunneling in a double quantum dot". In: *Physical Review B* 84.20 (2011), p. 205316 (cit. on p. 62).

[163] John A Sidles, Joseph L Garbini, and Gary P Drobny. "The theory of oscillator-coupled magnetic resonance with potential applications to molecular imaging". In: *Review of Scientific Instruments* 63.8 (1992), pp. 3881–3899 (cit. on p. 64).

[164] Vincent Freulon. "Étude de la décohérence de paquets d'onde monoélectroniques dans les canaux de bord de l'effet Hall quantique entier". PhD thesis. 2014 (cit. on pp. 67, 69).

[165] Igor L Aleiner, Piet Wibertus Brouwer, and Leonid I Glazman. "Quantum effects in Coulomb blockade". In: *Physics Reports* 358.5-6 (2002), pp. 309–440 (cit. on pp. 71, 72).

[166] O Usmani, Ya M Blanter, and Yu V Nazarov. "Strong feedback and current noise in nanoelectromechanical systems". In: *Physical Review B* 75.19 (2007), p. 195312 (cit. on p. 71).

[167] Fabio Pistolesi, Ya M Blanter, and Ivar Martin. "Self-consistent theory of molecular switching". In: *Physical Review B* 78.8 (2008), p. 085127 (cit. on p. 75).